Galaxy Cluster Gas Fractions from Interferometric Measurements of the Sunyaev-Zel'dovich Effect

Thesis by

Laura Grego

In partial fulfillment of the requirements

for the degree of

Doctor of Philosophy

California Institute of Technology

Pasadena, California

1999

(Submitted November 6, 1998)

Acknowledgements

I count myself extremely fortunate to have had the opportunity to work on such an interesting project at its inception and to be guided through my thesis research by two wonderful mentors.

To my thesis advisor, John Carlstrom, such written thanks are hardly sufficient for five years of personal and professional support and inspiration. It has been my luck to have worked with someone with such an inventive approach to physics and a seemingly bottomless well of knowledge and energy, as well as with such a great generosity and humanity.

And *muchas gracias* to Marshall Joy, who truly deserves the appellation of mentor, for his advice and guidance and his examples of truly inspired solutions to all problems technical, scientific and social.

The SZ project has thrived through an immense amount of hard work from a talented group. Many thanks to William Holzapfel, Erik Reese, Gil Holder, Sandy Patel, Asantha Cooray, and Cheryl Bankston, for all of your contributions and (at times) heroic efforts. Special thanks to Swlh from whom I've learned much, not the least how to sneak Brussels sprouts into the pea soup.

The success of this project has also been ensured by the hard work of those involved in developing the observing system. Many thanks to Marian Pospieszalski and all at NRAO who contributed to the HEMT amplifier design and construction, and John Kovac at the University of Chicago for constructing additional HEMT amplifiers for the experiment. Thanks to Steve Padin, Steve Scott, Dave Woody and the fabulous

crew at OVRO, who built such a fine observatory, and graciously overlooked the dents we incurred driving the site cars offroad. Thanks to Nick Scoville, Anneila Sargent, and the millimeter group for the opportunity to spend our summers at OVRO and for developing the reduction software. Thanks to Dick Plambeck, John Lugten, Rick Forster, Jack Welch, and the BIMA staff for all the work put in to ensure the success of the centimeter wave observations at their fine observatory. Thanks also to the staff at NASA MSFC, who lent their considerable skill to the construction of the receiver system.

Thanks also to Jack Hughes, -ray guru, for his generous contributions to the data fitting routine and for many helpful discussions.

My gratitute to the NASA Graduate Student Researchers Program, for four years of generous financial support.

Thanks to my fellow graduate students, the resident postdocs and my friends, for sharing their knowledge and for always being amenable to a coffee break or to work out an idea, scientific or philosophical. To the Caltech-ers, especially my officemates Rachel Akeson, who patiently helped me navigate the mysteries of MMA; Chris Fassnacht, for steadfast friendship and hours of cosmo homework; and Andrew Baker, heir to the OVRO throne and chef honors. And to Alexa Harter, Tom Murphy, Bill Weber and honorary Techer Reinaldo, for years of friendship and late nights in search of sigma 2. And to those at UChicago, Nils Halverson, John Kovac, Chris Mallouris, and Aparna Venkatesan, whose support and friendship ensured the completion of this thesis. Thanks also to the of postdocs, Joe, Carlo, Cole and Jean, who patiently answered so many questions from me.

And most importantly, thanks especially to my Mom, Dad and my sisters, for their love and support, and for frequent reminders me that work is only part of life.

Abstract

Interferometric measurements of the Sunyaev-Zel'dovich effect toward 18 highly x-ray luminous galaxy clusters are presented. The observations were made using centimeter-wave receivers specifically constructed for these observations. The data were taken with the receivers mounted on the Owens Valley Radio Observatory and Berkeley-Illinois-Maryland Association millimeter arrays between 1994 and 1998.

The interferometric data are used to determine the gas mass fraction in these clusters in a uniform method. The inteferometric data contain sufficient spatial information to derive models for the pressure distribution of the cluster gas. From these models, under the assumption that the gas is isothermal, the cluster gas masses are estimated and the total gravitating masses are inferred. The total gravitating mass measurement requires the additional assumption that the gas is in hydrostatic equilibrium with the cluster potential. The cluster gas temperatures are obtained from x-ray spectral observations or, in the few cases in which spectra were unavailable, estimated from x-ray luminosity-temperature relations in the literature. Since the experiment best measures the gas fraction within a fixed angular radius, the measured gas fractions are extrapolated to a fiducial radius, using a relation derived from published numerical simulations, to facilitate comparisons. The best estimate of the cluster gas fraction at r_{500}, the radius at which the enclosed mean density is 500 times the critical density, is $(0.071^{+0.010}_{-0.012})h_{100}^{-1}$, at 68% confidence.

Under the assumption that clusters are fair samples of the universe, the mass composition in clusters at the virial radius should reflect the universal mass composition.

The intracluster gas is the dominant component of a cluster's baryonic mass, and so the gas mass fraction is a good approximation of the baryon mass fraction. The baryon fraction in clusters, f_B, together with the universal baryon mass density, Ω_B, sets a limit on the universal mass density, in the standard cosmological paradigm: $\Omega_M = \Omega_B / f_B$. The cluster gas fraction measurements presented here set an upper limit to the universal mass density: $\Omega_M h_{100} \leq 0.27^{+0.07}_{-0.06}$, at 68% confidence. We make our best estimate of the universal matter density, including with the gas fraction estimates of the baryonic mass contained in galaxies and the baryonic mass which failed to become bound during the cluster formation process: $\Omega_M = 0.29^{+0.08}_{-0.06}$ at 68% confidence for h = 0.7.

Contents

List of Tables

List of Figures

Chapter 1

Introduction

1.1 The Sunyaev-Zel'dovich Effect in Galaxy Clusters

The development of the theory of the Sunyaev-Zel'dovich (SZ) effect in galaxy clusters in 1972 was inspired by the then-mysterious nature of the x-ray emission observed in galaxy clusters (Sunyaev & Zel'dovich 1972; Birkinshaw 1998). It had been known that the Sun is a strong x-ray source, and it was expected that other stars would be the primary celestial objects studied with planned balloon and rocket-borne x-ray experiments. That clusters of galaxies, which until the early 1970s were considered to be self-gravitationally bound assemblies of galaxies, were some of the strongest sources of x-ray emission in the sky was quite unexpected. The discovery of strong x-ray emission in the directions of the Virgo, Coma, and Perseus clusters in 1971 and the subsequent all-sky x-ray survey with the *Uhuru* satellite established that clusters of galaxies are generally sources of x-rays (see Sarazin 1988, and the references therein.) And so the nature of the galaxy cluster x-ray emission became a topic of intense investigation.

Leading theories suggested that the x-rays could have originated in thermal emission from hot, ionized gas trapped in the deep potential wells of the clusters, in synchrotron radiation from non-thermally distributed electrons interacting with magnetic fields, in cosmic microwave background (CMB) radiation Compton up-scattered by a hot plasma, or in stellar-type x-ray emission from discrete sources. Observational tests were suggested as discriminators between the competing theories, the detection of the Sunyaev-Zeldovich effect one such test.

Sunyaev and Zel'dovich had previously presented work on CMB anisotropies originating in hot plasmas (Sunyaev & Zel'dovich 1970), and the cluster question was a natural application of this work. The SZ effect is a spectral distortion of the CMB radiation should it inverse-Compton scatter from a thermal population of electrons. The distortion was predicted to be small in magnitude, but would be marginally measurable with the technology of the time. Its observation towards a cluster would have confirmed the nature of the x-ray emission as thermal Bremsstrahlung. Measuring the SZ effect proved to be difficult, indeed, and the origin of the x-rays was eventually established through x-ray observations with improved imaging capabilities and spectral resolution and correlations of these with radio observations (see Sarazin 1988, and the references therein). Galaxy cluster x-ray emission does come primarily from thermal Bremsstrahlung and line emission from massive quantities of hot gas. This gas is hot, with electron temperatures, T_e, from $\sim$5 to 15 keV and rarefied, with peak electron number densities of $n_e \simeq 10^{-3}\mathrm{cm}^{-3}$. It cools slowly, mainly by this x-ray band emission, with cooling times on the order of

$$t_{cool} = 8.5 \times 10^{10}\mathrm{yr}\left(\frac{n_p}{10^{-3}\mathrm{cm}^{-3}}\right)^{-1}\left(\frac{T_e}{10^8\mathrm{K}}\right)^{1/2}, \qquad (1.1)$$

(Sarazin 1987). For most clusters, this is much longer than a Hubble time.

Although the SZ effect did not play a part in discovering the nature of the hot gas, the SZ effect's potential as a tool for investigating the physics of large scale structure

formation and cosmology was recognized.

A description of the physical mechanism which produces the SZ effect is helpful in illustrating its uses. The SZ effect is a spectral distortion of CMB radiation due to inverse-Compton scattering of the CMB photons off of hot plasma (Sunyaev & Zel'dovich 1972). In galaxy clusters, the ionized intracluster gas serves as scattering medium. A small fraction, $< 1\%$, of the incident photons are scattered and, on average, these photons gain energy. At frequencies less than about 217 GHz, the intensity of the CMB radiation is diminished as compared to the unscattered CMB, and the SZ effect is manifested as a temperature decrement towards the cluster. This decrement, $\frac{\Delta T_{SZ}}{T_{CMB}}$, or $\frac{\Delta T_{SZ}}{T}$ for simplicity, has a magnitude proportional to the Compton y-parameter, *i.e.*, total number of scatterers, weighted by their associated temperature,

$$y = \frac{k\sigma_T}{m_e c^2} \int n_e(l) T_e(l) dl, \tag{1.2}$$

where k is Boltzmann's constant, σ_T is the Thomson scattering cross section, m_e is the electron mass, n_e is the electron density, T_e is the electron gas temperature, and the integral extends along the line of sight (dl). Note that $\frac{\Delta T_{SZ}}{T}$ is then simply proportional to the integrated gas pressure.

The proportionality depends on the observing frequency, ν, and also weakly on the electron temperature through relativistic corrections. The change in spectral intensity due to the Sunyaev-Zel'dovich effect is calculated for the Rayleigh-Jeans approximation (*c.f.* Rephaeli 1995, Challinor & Lasenby 1997):

$$\left.\frac{\Delta T_{SZ}}{T}\right|_{RJ} = \frac{y x^2 e^x}{(e^x - 1)^2} [x \coth(x/2) - 4 + \theta_e f(x)], \tag{1.3}$$

where $x = \frac{h\nu}{kT}$ and $\theta_e = \frac{kT_e}{m_e c^2}$. The last term corrects for relativistic effects.

The peculiar velocity, its velocity with respect to the Hubble flow, of a cluster will also produce a "kinetic" SZ effect, analgous to scattering photons off a moving mirror. The kinetic SZ effect is a potentially powerful probe of the structure of the

universe on scales even larger than clusters. The magnitude of the decrement due to peculiar velocity is frequency-independent and is, over much of the spectrum, an order of magnitude or more smaller than the thermal effect but can be measured near the thermal effect's zero-crossing. Figure 1.1 shows the spectrum of the SZ effect measured in antenna temperature, for an extremely massive cluster. The kinetic effect is shown for a peculiar velocity of 1000 km/s. Measurements of the kinetic SZ effect have set an upper limit to the peculiar velocity of two clusters; the peculiar velocities must be less than 2-3% of the Hubble flow (Holzapfel *et al.* 1996). With current observational techniques, using the Caltech Submillimeter Observatory on Mauna Kea, Hawaii, the atmosphere limits the observational precision to about 700 km/s. New observing systems are planned for deployment, and the future of the field shows great promise.

The SZ effect has an unusual characteristic for an astronomical observable; the observed magnitude of the decrement is independent of redshift. A cluster's SZ effect depends only on its y-parameter, an intrinsic property, not its distance; clusters should be observable, then, at any distance at which they exist as collapsed objects, and at which they are resolved. One megaparsec, the size scale of clusters, will not subtend less than an arcminute, even at $z >> 1$. The SZ effect is therefore an ideal tool for exploring the distant history of structure formation. Incidentally, detection of the SZ effect in clusters confirms the cosmic nature of the CMB; the CMB must originate at least as far away as the furthest detected SZ cluster.

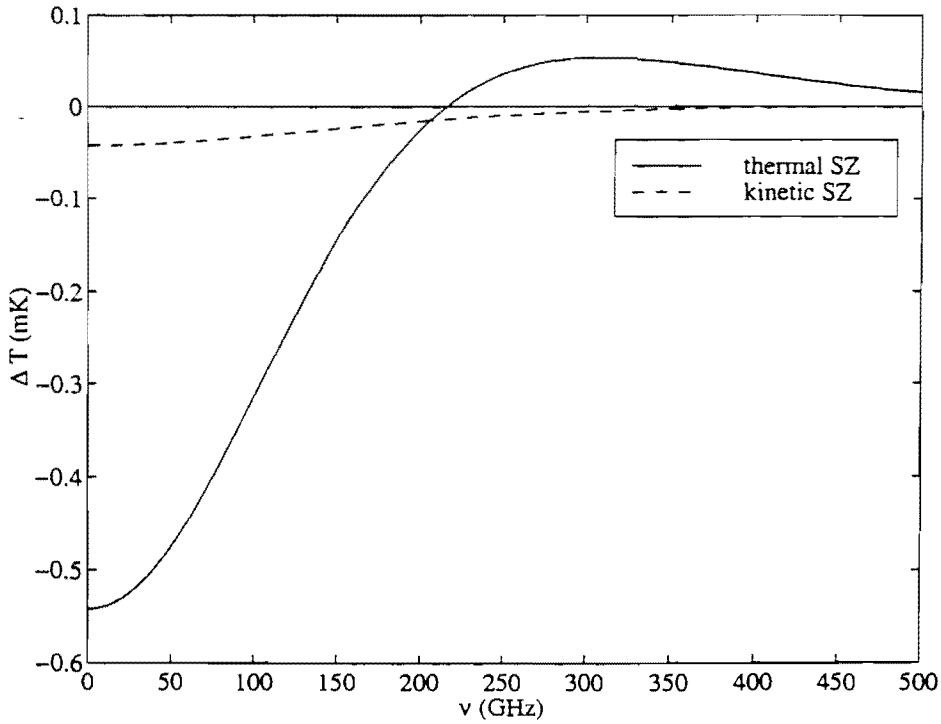

Figure 1.1 Spectrum of the thermal and kinetic SZ effects, plotted as ΔT_{SZ} in the Rayleigh-Jeans approximation for a cluster with $y = 10^4$, $v_p = 1000$ km/s.

1.2 Galaxy Cluster Gas Fractions from the SZ Effect

The physics of galaxy clusters and of large scale structure formation can be investigated with the SZ effect. The intra-cluster medium (ICM) is the dominant visible baryonic mass component. The mass in this phase is nearly an order of magnitude larger than the mass in optically observed galaxies (White *et al.* 1993; Forman & Jones 1982). The spatial distribution of the ICM, especially in relation to the total mass, provides information on the dynamical history of these massive objects. Since the sound crossing time typical of cluster gas is much less than the dynamical time,

one may reasonably assume that the cluster gas is relaxed in the cluster's potential. Hydrodynamic simulations have supported this notion (*e.g.*, Evrard, Metzler & Navarro 1996). In the simplest analyses, the gas is in hydrostatic equilibrium (HSE) with the cluster potential, supported only by thermal pressure. Evidence of non-equilibrium suggests either recent dynamical activity, *e.g.*, a recent merger, or evidence that additional physics, *e.g.*, magnetic fields, should be included in the cluster models.

Under the assumption of HSE under thermal pressure support, the total cluster mass can be extracted from the density and temperature spatial distribution of the ICM. The relative spatial distribution of the dark matter and of the ICM is reflective of the energetics of the cluster. If gravitational instability is the only force governing structure formation, the gas distribution should closely follow the dark matter distribution. Evidence suggests that the ICM is distributed more uniformly than the dark matter. David *et al.* (1995) find, from x-ray observations of a nearby sample of clusters with a wide range of masses, that the dark matter has a steeper radial density profile, $\rho_{dark} \propto r^{-2}$, than the gas, and that the distribution of the gas tends to become shallower with decreasing mass. They find a range of profiles, from $\rho_{gas} \propto r^{-2.0}$ in the most massive systems, to $\rho_{gas} \propto r^{-1.0}$ in groups. This behavior is to be expected if energy transfer from galaxies and the dark matter to the gas is important. Spatially resolved SZ effect measurements and ICM temperature measurements can be used together to measure both the gas and dark matter mass distributions, and therefore also the cluster gas mass fraction.

The SZ effect can also be used as a cosmological probe. SZ measurements combined with x-ray and optical observations can yield measurements of the distances to clusters. One method is the deduction of the characteristic scale, R, of a cluster by comparing SZ and x-ray observations. With this, one can infer the angular diameter distance, D_A, to the cluster, since D_A relates this length to the apparent

size, θ: $D_A = R/\theta$. This deduction is possible because the x-ray observable, the surface brightness, is proportional to the emission measure, $S_x \propto \int n_e^2 f(T_e) dl$, where $f(T_e)$ is a weak function of temperature for hot clusters, and the integration is along the line of sight; in contrast, the SZ effect is proportional to the first power of the density, $\frac{\Delta T_{SZ}}{T} \propto \int n_e T_e dl$. With knowledge of the gas temperature, one can solve for the length scale of the cluster. These measurements, especially when taken over a large sample, can provide an independent assessment of $H_\circ$, the expansion rate of the universe, which is free from possible distance-ladder systematics. The geometry of the universe can be constrained by Measurements of $H_\circ$ to a sample of clusters with a range of redshifts, since the evolution of $H_\circ$ with redshift is geometry-dependent.

The gas mass fraction is also a useful cosmological probe. Mechanisms for segregating baryonic matter from dark matter on cluster mass scales ($> 10^{14} M_\odot$) are difficult to reconcile with observations and standard cosmological and large scale structure models (White *et al.* 1993, Evrard *et al.* 1997). Under the fair sample hypothesis, then, at the virial radius the mass composition of clusters is expected to reflect the universal mass composition. A cluster's gas mass fraction, which constitutes a lower limit to its baryonic mass fraction, is then a lower limit to the universal baryon fraction, i.e., $f_{gas} \leq f_B = \Omega_B/\Omega_M$, where Ω_B is the ratio of the density of baryons to the critical density, $\Omega_\circ = \frac{3H_\circ^2}{8\pi G}$, and G is the gravitational constant. The value of Ω_B can be inferred from measurements of light element abundances and standard Big Bang Nucleosynthesis (BBN) theory (Wagoner, Fowler, & Hoyle 1967; Copi, Schramm, & Turner 1995). Thus, an upper limit on Ω_M can be derived from the gas fraction measurement.

Extending this argument, since the baryon fraction of clusters should reach the universal value at the virial radius, the baryon fraction of clusters should be constant at this radius. Under this assumption, any systematic variation with redshift of the gas fraction at its virial radius should be due to having assumed incorrect values for the

cosmological parameters. The correct values for (Ω_M, Ω_Λ) can then be determined from the gas fraction measurements; they will be the values which make the gas fraction constant with redshift.

In this thesis are presented measurements of the cluster gas fraction, based on SZ measurements conducted from 1994-1998, and a discussion of the implications of these measurements for cluster physics and for cosmology. Chapter 2 describes the instrument we have constructed expressly to make such measurements, as well as the observational strategy. In Chapter 3 a discussion is presented of the reduction and calibration methods for the SZ measurements. Chapter 4 contains a description of the procedure for fitting the SZ data to models for the cluster gas. Chapter 5 contains a detailed description of the methods used to extract cluster gas masses and gas fractions from the SZ observations, including a discussion of the possible systematic uncertainties. In Chapter 6, these prescriptions are applied to a test case, the cluster Abell 370, an extreme example. Chapter 7 contains a description of the observed cluster sample and the criteria for selecting clusters. In Chapter 8, the gas fractions for the entire cluster sample are presented, and the implications for cluster physics and cosmology are discussed in depth. A summary of the results and a discussion of future work is contained in Chapter 9.

Chapter 2

Instrument and Observations

2.1 An Overview of the OVRO-BIMA 30 GHz SZ Observations

Measurements of the SZ effect have been historically difficult to make because the magnitude of the signal is small, on the order of 1 mK or less. To make reliable measurements of the SZ decrement in a reasonable amount of time, the instrumental sensitivity must be high and the systematic effects well-understood. The instrument must also be well matched to the large angular size of clusters. The core radius of a cluster, its characteristic size, can be estimated from optical and x-ray observations. Cluster galaxies are usually smoothly distributed, and the core radius is usually defined to be the projected radius at which the galaxy density is one-half that at the center of the cluster. Bahcall (1975) suggests that the core radii of regular, non-merging, clusters are similar in size, about $r_c = (0.50 \pm 0.008) h_{100}^{-1}$ Mpc. The core radii of the gas density distribution determined from x-ray observations are more widely distributed, and are found to be $(0.14 - 1.8) h_{100}^{-1}$ Mpc in the EMSS sample (Jones & Forman 1984), although this measurement is likely to be contaminated by cooling flows in the sample clusters. In Figure 2.1, the angular size subtended by 1 Mpc, about the characteristicsize of a cluster, is shown as a function of redshift.. It

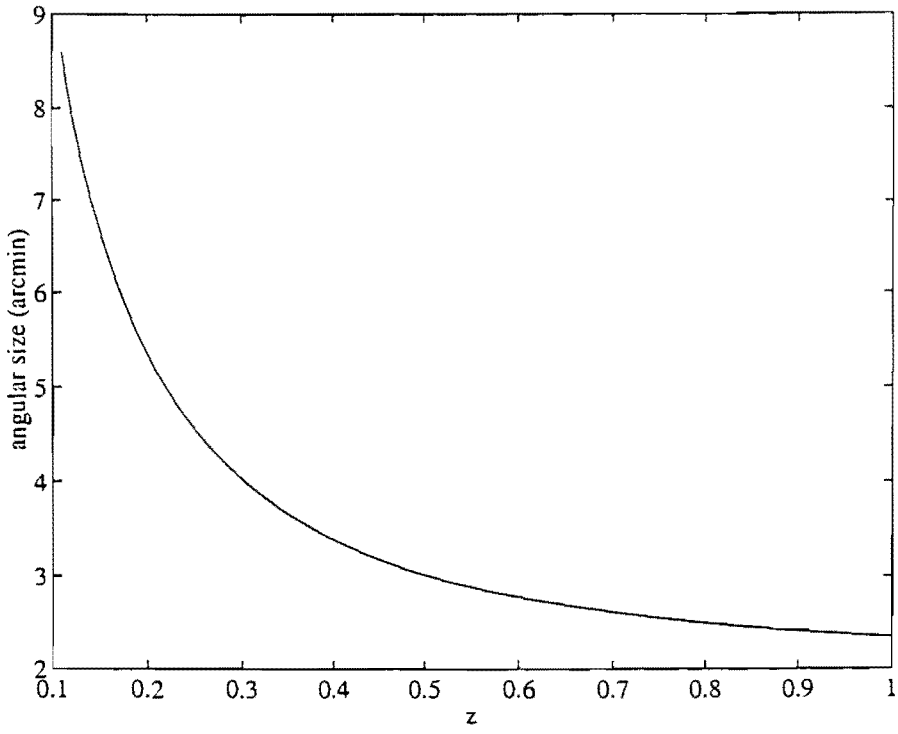

Figure 2.1 Angular size of a 1 Mpc cluster vs. redshift, with h=0.7, $\Omega_M = 0.3$, $\Omega_\Lambda = 0$.

is clear from this figure that an instrument used to observe the SZ effect should have sensitivity at arcminute or larger scales.

The first detections of the SZ effect were made with single dish radiometric techniques. The radiometric observations take advantage of the fact that at microwave frequencies, the existing large telescopes have an angular beam size of a few arcminutes. To measure the flux and time-variation of radio-bright point sources in the cluster fields, the fields generally are observed also with an interferometer. Sophisticated beamswitching techniques are essential for separating the atmosphere's emission and differential ground pickup from the SZ decrement, although ground pickup can be minimized by observing preferentially at high elevations, severely tapering the antenna illumination pattern, and minimizing scatter from the telescope structure.

Clusters can, in principle, be observed at arbitrary redshift with single dish experiments, although observing efficiency is decreased by beam dilution when the cluster is unresolved. This is a constraint for experiments in which significant amounts of observing time are needed in order to securely ascertain systematic uncertainty levels, and so many single dish experiments with large beams preferentially observe nearby clusters. These methods have met with regular success and are currently used by a number of research groups. An excellent review of the history of the field and summary of current research can be found in Birkinshaw (1998).

One can also use interferometric techniques to measure the SZ effect. Well-designed interferometry experiments provide two-dimensional spatial information about the gas distribution and can separate the effects of potentially confusing radio point sources from concurrent measurements of the decrement. The interferometric method rejects noise uncorrelated between array elements, so systematic measurement uncertainties commonly associated with single dish measurements, such as differential ground and atmospheric emission, are controlled straightforwardly.

Contamination from point sources may pose a serious problem. The average spectral index of radio bright point sources associated with clusters is $\alpha = 0.77 \pm 0.06$, where $S_\nu \propto \nu^\alpha$, S_ν is flux, and ν is frequency (Cooray *et al.* 1998), so it is preferable to keep the observing frequency high; at frequencies greater than 100 GHz, however, thermal emission from dust in galaxies may become important sources of contamination.

Interferometers are generally designed for high resolution imaging and take advantage of the relative technical simplicity of long wavelength observations. For example, at the NRAO Very Large Array (VLA), a 27 element array of 25 meter dishes, SZ observations would need to be made at long wavelengths, 3 centimeters or longer, in order to access cluster scales. Contamination from point sources will be significant at these wavelengths, however, and so VLA observations are not suited to SZ work.

To make interferometric observations of the SZ effect in clusters, one requires a specially-built instrument or modification of an existing instrument. The Ryle telescope in Cambridge, England, was the first such modified instrument. The existing system, an east-west array with 15 meter dishes at fixed positions, was modified to work at 15 GHz (Jones 1990). The first interferometric SZ detections were reported by this group in Jones *et al.* (1993) and Grainge *et al.* (1993).

We have constructed a system with which to operate millimeter-wave interferometers at centimeter wavelengths, allowing us to both benefit from the suppressed systematic error level typical of interferometers as well as access the large angular scales of clusters. Receivers built to operate at centimeter wavelengths were integrated into the millimeter-wavelength interferometer systems at the Owens Valley Radio Observatory (OVRO) Millimeter Array and at the Berkeley-Illinois-Maryland Association (BIMA) Millimeter Array. The arrays are fully two-dimensional and the configuration of the many elements can be easily changed. Observing with the compact telescope configurations of the arrays at these longer wavelengths allows access to the angular scales of clusters. At these frequencies (26–36 GHz), contaminating point sources are a manageable problem; the high resolution elements permit identifying and quantifying any point sources present. Operating these systems at ~ 10 times lower frequency than the design frequency allows for very good optical performance. The recent development of low-noise High Electron Mobility Transistor (HEMT) based amplifiers working at these frequencies (see Pospieszalski 1995) has enabled construction of receivers sensitive enough so that an effect so small can be detected significantly in a reasonable amount of time. The first detections from this system are reported in Carlstrom, Joy, & Grego (1996) and Carlstrom *et al.* (1997).

2.2 26-36 GHz Receivers

We constructed centimeter-wave receivers designed to integrate with a millimeter interferometer system. A schematic of the receiver is presented in Figure 2.2. Each labeled component will be discussed in turn. Photographs of the receiver are reproduced in the top and bottom panels of Figure 2.3.

The receivers are based on cryogenically-cooled HEMT amplifiers, built at NRAO and at the University of Chicago. These are four-stage HEMT amplifiers. The first stage is always an InP device, and the latter stages are either GaAs or InP. Four-stage InP HEMT amplifiers have higher gain and lower noise than the GaAs/InP devices. The amplifiers have a gain of 28-35 dB, depending on the device, over a passband of about 26 to 36 GHz, with flatness $\sim$ 4dB over this band. Receiver temperatures range from 11-19 K at 28-30 GHz, the frequency at which the SZ observations are currently made. A highpass filter (Spacek Labs, Santa Barbara, CA, model no. A28-6-F-32-7), which allows the system to operate in single-sideband mode for local oscillator (LO) frequencies below 28 GHz, follows the HEMT amplifier. We found the inclusion of a broadband isolator between the HEMT amplifier and the filter improved the spectral passband response of the receiver. During the 1997 season, only a few of the receivers contained isolators (Channel Microwave Corporation, Camarillo, CA, Model IR627); in the others, the highpass filter contained a 3 dB attenuating vane in order to minimize reflections back into the HEMT amplifier.

The highpass-filtered signal is input to a Schottky diode-based mixer (Spacek Labs, Santa Barbara, CA, model MKaKa-9.) The local oscillator system driving the mixer will be discussed below. From the mixer, the intermediate frequency (IF) signal is amplified by a cooled 30 dB IF amplifier (Miteq, Hauppauge, NY, Model AMF-3D-010080-13-CRYO). The IF signal is output from the dewar through 0.085" diameter low thermal conductivity semi-rigid coaxial cable, which has a silver-plated

steel center conductor and either a stainless steel or beryllium-copper outer conductor.

The scalar feedhorn is coupled to the HEMT amplifier through a circular polarizer, added before the 1996 observing season, and a circular-to-linear waveguide transition. Before 1996, the system responded to linearly polarized light. Figure 2.3, top panel, shows the receiver system as it is mounted in the dewar. The dewar window is made of expanded polystyrene, and has a styrofoam support.

The receiver is cooled by a cryogenic two-stage closed-cycle helium refrigerator (CTI Model 350). The first stage (70K) is used to cool the radiation shield, an aluminum case. This shield is in place in the bottom panel in Figure 2.3. To reduce the heat load on this stage, the radiation shield was plated with a gold layer before the 1997 observing season. For the observing seasons prior to 1997, the dewar case was lined with $\sim$10 sheets of superinsulation (aluminized mylar). To reduce its emissivity, the outer dewar case (at 300K) was also gold plated.

This entire system, from the feedhorn to the IF amplifier, is in good thermal contact with the second stage of the cryocooler ($\sim$10 K) through indium-coated copper braid and copper sheeting. The amplifier and downconverter assembly is supported on fiberglas-epoxy (G10) composite cylindrical standoffs, in order to maintain rigid support while keeping the heat load low.

The LO signal is generated by a room-temperature YIG oscillator. Six receivers have YIGs tunable between 26 and 40 GHz (Avantek ADD26240-M), and the four receivers constructed post-1997 use YIG oscillators tunable from 13-20 GHz (Micro Lambda Inc., Fremont, CA, Model MLOB-1385PD), which were modified from original design frequency range of 13-18 GHz. Frequency doublers (DBS Microwave, El Dorado Hills, CA, Model DBS-2640x218) are used with these oscillators, and so they, too, can drive the mixer with a 26-40 GHz LO signal. The LO signal is sent through flexible coaxial cable and hermetically sealed connectors to the mixer. A sample of the LO signal is coupled via a 10dB coupler to a harmonic mixer (Spacek Labs,

Santa Barbara, CA, Model GKa-305), which then interfaces with standard OVRO and BIMA phaselock systems.

2.3 Interferometers

The centimeter-wave receivers were designed to be integrated with the Owens Valley Radio Observatory (OVRO) millimeter array. It was possible to make observations for long (~30 day) sessions in the summer, when high atmospheric water content made millimeter-wave observations impractical. Additional receivers were constructed as the millimeter array gained additional telescopes; from 1994-1995, the array grew from four telescopes to six. Observations have continued at OVRO in the summers of 1996 and 1998.

In the summer of 1996, we also made observations at the Berkeley-Illinois-Maryland Association (BIMA) millimeter interferometer with these six receivers. Three additional receivers were constructed after this season, and a total of nine of the BIMA telescopes were operated at centimeter wavelengths in the summers of 1997 and 1998. A spare (tenth) receiver was constructed prior to the 1998 observing season.

Contained in the following section is a description of the observatories' characteristics and the details of integrating the centimeter wave receivers into the millimeter systems.

2.3.1 OVRO

The Owens Valley Radio Observatory (OVRO) Millimeter Array is located to the east side of the Sierra Nevada mountains at an altitude of 1,222 meters. In the summer, when these observations took place, the weather was adequate for observing about 80% of the time. The array consists of six 10.4 meter diameter radio dishes, each with

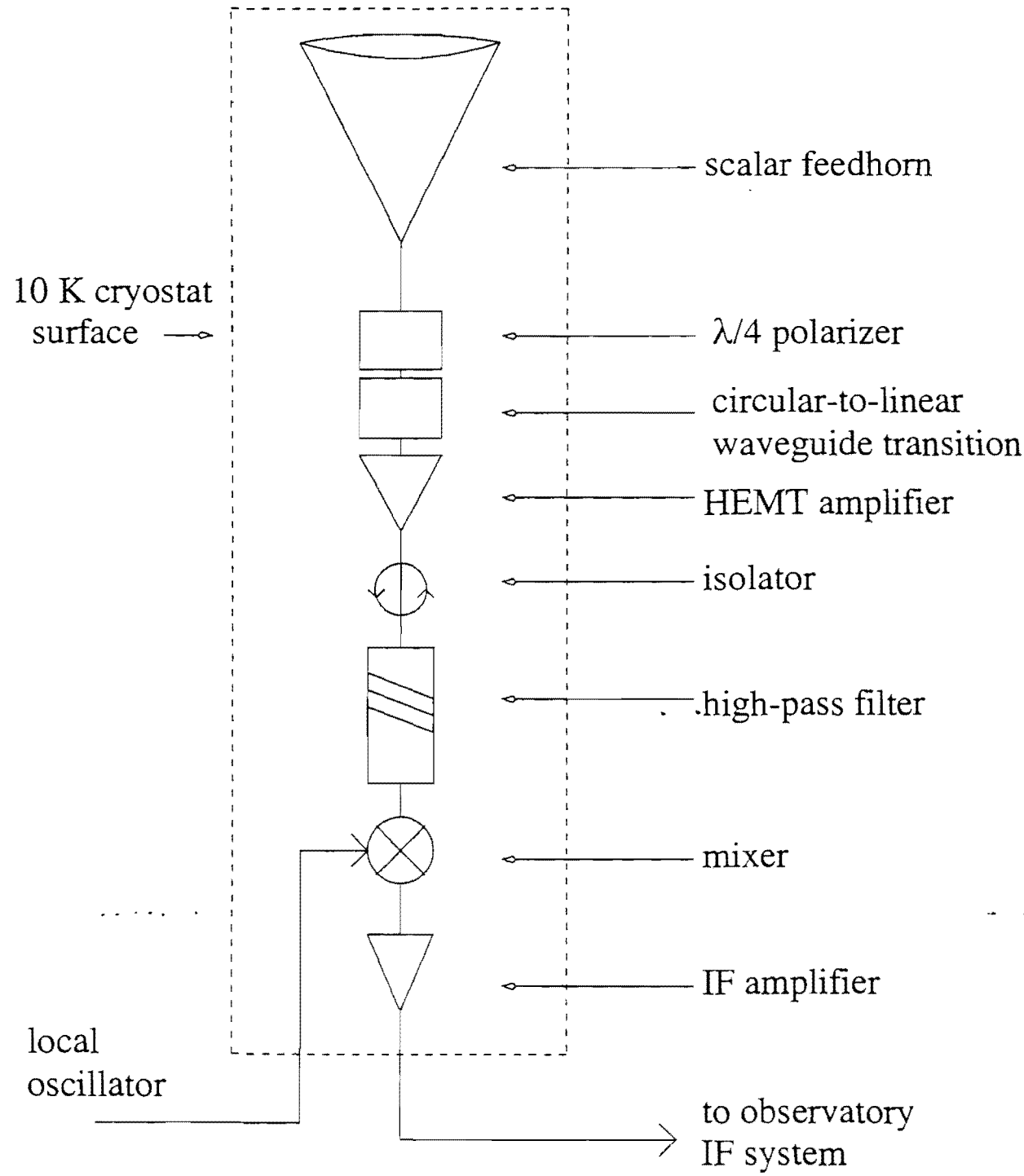

Figure 2.2 26-36 GHz receiver schematic.

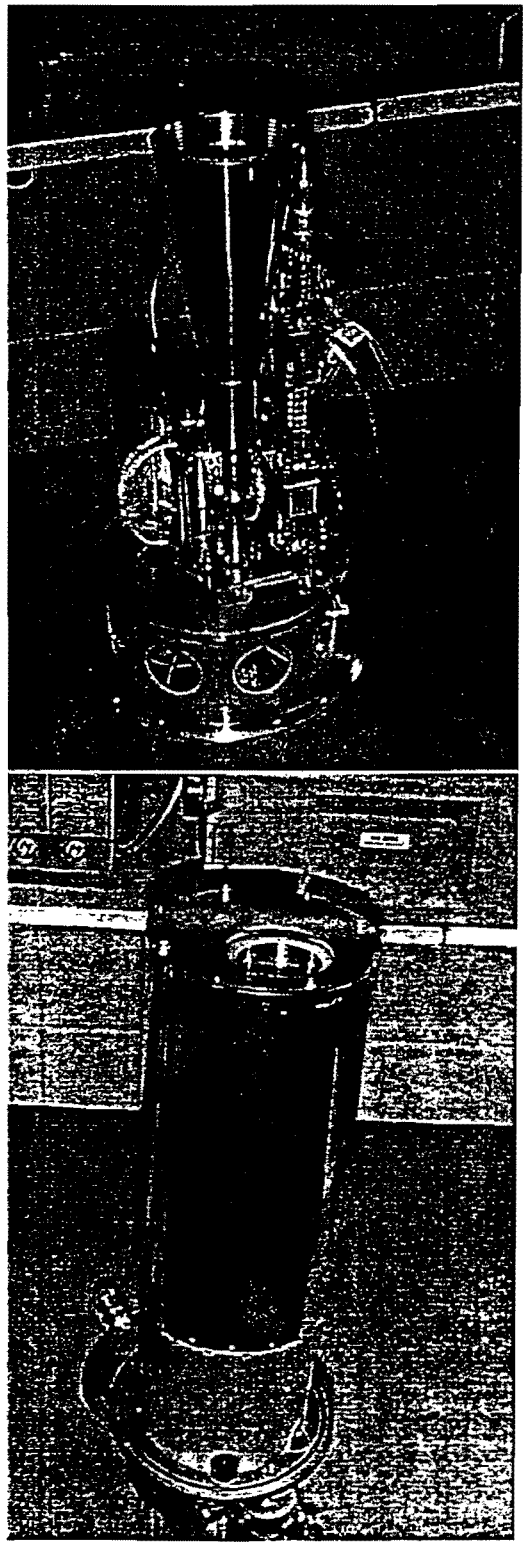

Figure 2.3 The 26-36 GHz receiver. Top: the 10K surface. Bottom: with radiation shield in place.

r.m.s. surface precision of 35 μm. The aperture efficiency at 28.5 GHz was measured by holographic techniques to be ~0.75. The contribution of the antenna, including spillover, to the system temperature is ~12-15 K, as measured from sky dips. The array is fully two-dimensional, with baselines ranging from 14 to 240 meters. A general description of the OVRO millimeter array is provided in Padin *et al.* (1991).

At OVRO, the receiver dewar case and refrigerator are mounted to the telescope by bolting the window end of the dewar to a space frame which fixes the dewar near the focus of a tertiary reimaging mirror which is also fixed by the space frame. (See Figure 2.5.) The OVRO millimeter system contains a tertiary flat mirror which directs the beam to the millimeter receiver system at the Nasmyth focus. To use the centimeter system, the tertiary flat mirror is removed, and the beam from the 10.4 meter Leighton telescope is coupled to the feedhorn through the tertiary reimaging mirror. The reimaging mirror is an off-axis ellipsoidal reflector. This mirror has three points around its perimeter at which the optical surface can be adjusted with push-and-pull screws. The optical surface is adjusted so that the secondary is refocused at the front surface of the feedhorn. The secondary mirror is focused by adjusting its distance from the primary surface.

The alignment of the tertiary mirror is performed using a half-circle mask of material absorbent at centimeter wavelengths, mounted on the secondary mirror. The mask, which covers half of the secondary mirror at a time, is rotated through four positions (quadrants) and the power of the system is checked to ensure it is the same whichever part of the secondary is covered.

The compressors are mounted on the alidade platforms, and the helium lines are secured against twisting. These bend minimally with change in telescope elevation. The LO system is shielded from the weather by an insulated aluminum box, mounted to the dewar case. Since the ambient temperature can change from 100°F in mid-afternoon to 50°F before sunrise, the LO system temperature regulation system is

crucial; the YIG oscillator is extremely temperature sensitive and may drift ~100 MHz in frequency due to a temperature change of just a few degrees. The temperature regulation system evolved over the five observing seasons, from fans mounted near the oscillator to keep the air circulated (the YIG itself is a significant producer of heat) to the present incarnation, a Peltier cooler mounted to the YIG body with a regulating circuit which keeps the temperature constant to within 0.1° C.

The system temperature is checked before and after each integration and extrapolated between the measurements, using what is commonly called the "chopper wheel" method (Ulich & Haas 1976, Kutner & Ulich 1981). The millimeter system temperatures are checked by the insertion and retraction of an absorbing wheel which is mounted near the sidecab window and therefore inaccessible to the centimeter system. We constructed an ambient temperature absorber to mount to the bolt circle by which the dewar is secured to the space frame. This ambient load, a cone of absorbing material, is inserted and retracted from the system according to the same feedback loop used for the millimeter absorbers. The outsides of the cones are constructed of lightweight aluminum sheeting so that the receiver does not "see through" the foam, and so the cones don't get radiatively heated by direct sunlight and consequently differ in temperature from the ambient temperature measured by the thermometer mounted at the control building a few hundred meters away. The servo motor is stopped by a magnetic switch, with one piece mounted in the cone arm, and one in the motor's box.

The intermediate frequency (IF) signal is sent via flexible coaxial cable to the sidecab, and then is sent over optical fiber to the correlator room in the basement of the control building. There the signal is passed through the delay lines. Care is paid to set correctly the power level of the signals. Since the optical fiber and the correlator inputs have different dynamic range, it must be ensured that the power levels are not too low, which would allow the noise in the post-receiver system to

contribute significantly to the instrument noise, or too high, which would saturate the system and create an error in the measured signal amplitude. This problem is specific to the centimeter system, in which the power from the ambient load is a factor of $\sim$10 greater than that from the sky. The dynamic range of the millimeter observations is not so large, since the sky emits strongly at millimeter wavelengths.

The continuum measurements are made with the dual-channel analog correlator, each channel having an input bandwidth of 1 GHz (see Padin 1994 for a full description of the analog correlator.) In 1994, the SZ observations were made using a single channel centered at 28.7 GHz. After 1994, the observations were made using two 1 GHz channels, centered on 28.5 and 30 GHz. The receivers were modified after 1994 to include high-pass filters with a cutoff frequency of 27 GHz which again enabled the observations to be made in single-sideband mode. For a continuum source, operation in single-sideband mode affords an improvement of $\sqrt{2}$ in signal-to-noise ratio (S/N) with respect to double-sideband mode with balanced gains.

The OVRO observing control program (CMA) continually checks the performance of the interferometer, and will not collect data when the system is not performing optimally, *e.g.*, if the correlator environment is above a specific temperature, if the LO system is not properly locked, if the telescope has difficulty acquiring the source position, *etc.*. Such a system minimizes both the amount of data editing necessary and the possibility of including corrupt data in the analysis. A full description of CMA and its attributes can be found in Finch & Scott (1996), and Scott & Finch (1998).

The observatory's coordinates are latitude: 37° 14′ 02″ and longitude: 118° 16′ 56″. Adequate u-v coverage can be obtained for sources with declinations greater than about -10°. Typically, two or three different telescope configurations were used each observing season, to expand the u-v coverage, to optimize the u-v coverage at different declinations, or to enhance the recovery of the positions and fluxes of radio-bright

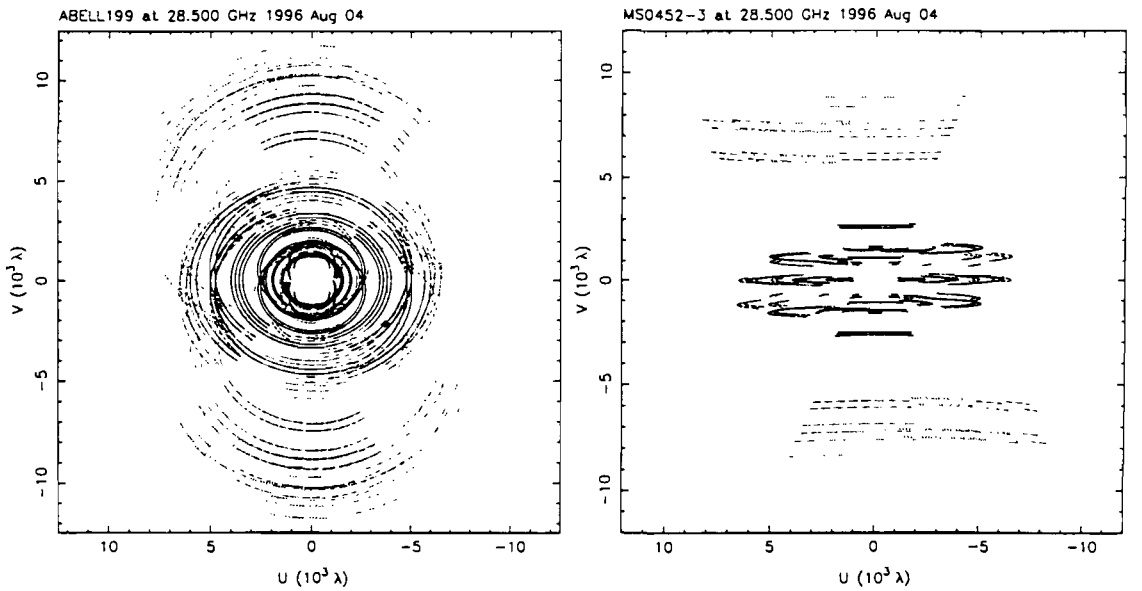

Figure 2.4 The u-v coverage at OVRO is shown for representative high and low declination sources. Abell 1995, left, is at α_{J2000} : $14^h52^m57.5^s$, δ_{J2000} : 58°02′55.2″. MS0451-03, right, is at α_{J2000} : $04^h51^s40.5^s$, δ_{J2000} : −03°05′46.0″.

point sources in the field. Typical u-v coverage for a high-declination source and for a low-declination source are shown in Figure 2.4.

Holographic measurements were used to determine the primary beam of each telescope. The beams for each dish are quite similar, the full width at half maximum (FWHM) varying maximally five percent, and are nearly Gaussian with a FWHM of 3.8 arcminutes.

2.3.2 BIMA

The Berkeley-Illinois-Maryland Association (BIMA) millimeter array is located at Hat Creek, CA, in the southern Cascade mountain range, at an altitude of 1021 meters. The array consists of ten 6.1 meter diameter radio dishes, with typical *r.m.s.* surface accuracy of 30 μm. The aperture efficiency at 30 GHz is ~0.70. The secondary mirror support structure is designed to have minimal blockage of the dish surface and

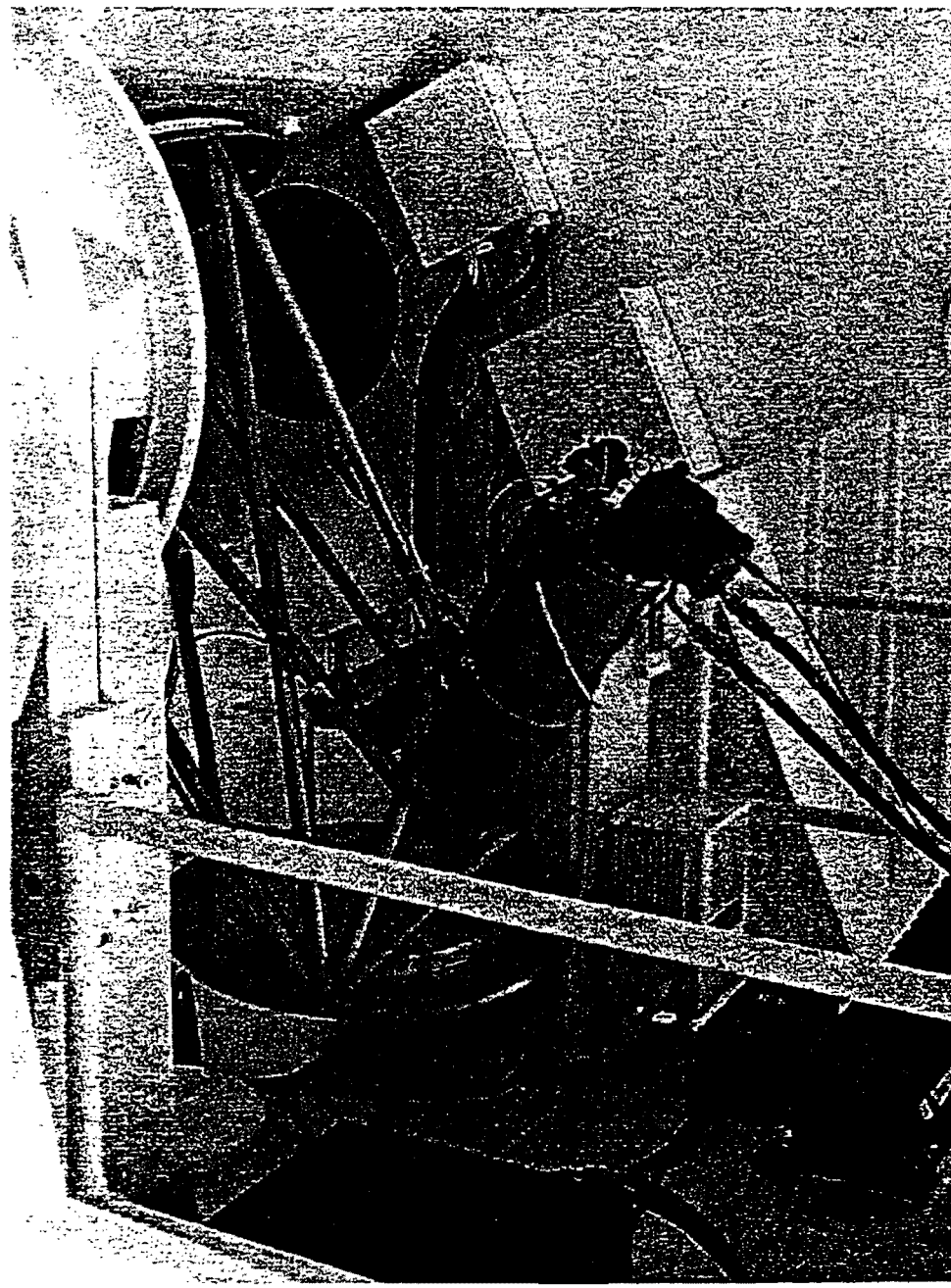

Figure 2.5 The receiver and tertiary mirror mounted, using a space frame, to the OVRO telescope.

so the contribution to the system temperature from the antenna is minimal, ~6 K. The BIMA array is fully two-dimensional, with baselines ranging from as short as 7.5 m and as long as 1 km. The telescopes are outfitted with collision protection, both mechanical and in the software. A general description of the BIMA interferometer is given in Welch *et al.* (1996).

The centimeter-wave receivers and LO system are the same as those we used at OVRO. To integrate the receiver with the BIMA system, we replace the millimeter system receiver dewar and mount the centimeter wave dewar in its place with a specially designed bracket which allows for easy alignment of the receiver. (See Figure 2.3.2.) The cm-wave receiver was designed for the OVRO system, which has a very different focal length/dish diameter ratio. In order to efficiently couple the beam to the feedhorn, a Teflon lens is introduced in the optical path in front of the dewar; there is not enough room in the receiver cabin for a reimaging system. The system temperature is measured by the introduction of an absorbing ambient load made of metal-backed ecosorb which can be moved in and out of the optical path between the lens and receiver. The receiver is carefully aligned by covering the secondary mirror with an absorbing foam half-circle and requiring that the power through the system be the same when each of the north, south, east, and west halves of the secondary mirror are covered. Care is taken to perform this measurement at sufficiently high elevation $> 45°$ to ensure the telescope does not see the ground. The receiver cabin is climate-controlled, and the YIG tuning is computer-controlled, so the additional temperature control system for our LO box is unnecessary.

The IF signal is routed through the existing downconversion system and sent via coaxial cable to the correlator in the control building. The signal passes through the delay lines and then is sent to the correlator (Welch *et al.*1996). The correlator is a hybrid, using single sideband downconverters followed by analog lowpass filters and then 2 bit digitization. The correlation is then done digitally. We operate the

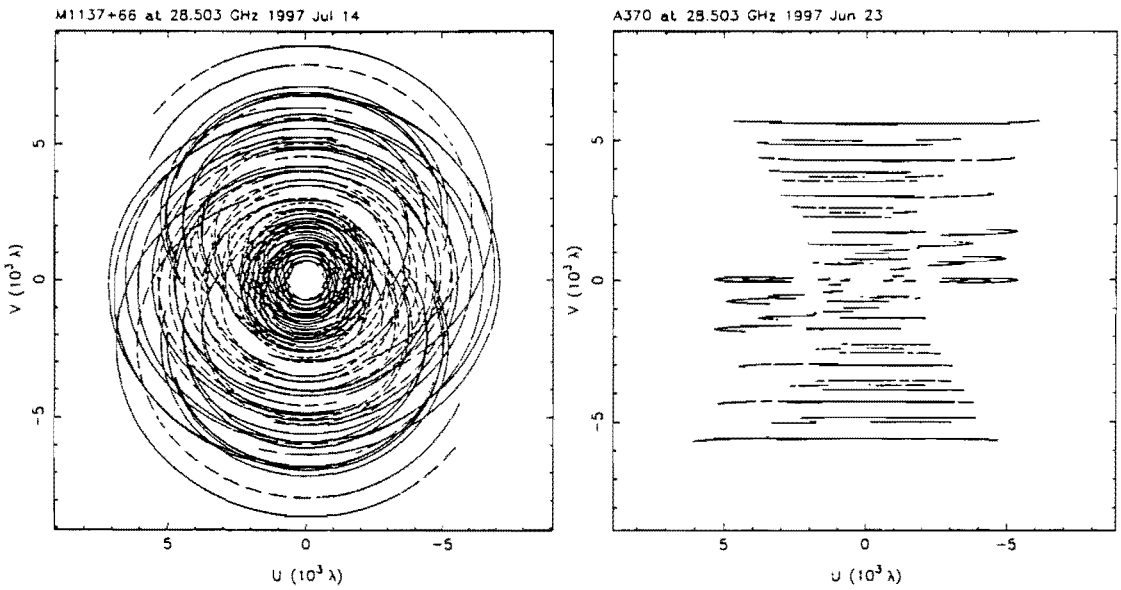

Figure 2.6 The u-v coverage at BIMA is shown for representative high and low declination sources. MS1137.5+6625, left, is at α_{J2000} : $11^h37^m36.2^s$, δ_{J2000} : 66°24′56.9″. Abell 370, right, is at α_{J2000} : $02^h37^s20.0^s$, δ_{J2000} : −01°47′11.70″.

correlator in wideband mode (mode 8 in the notation of Welch *et al.*1996) using the entire 800 MHz and 2-bit sampling. The interferometer data are written to a standard MIRIAD file (Wright and Sault 1993; Sault *et al.*1995). Data corrupted by error in the system, like mismeasurement of the system temperature or radio interference, are removed in the reduction phase.

The observatory is located at latitude: 40.8173, longitude: 121.4690, and adequate u-v coverage can be obtained for sources with declinations greater than about -10°. Typically, one or two configurations were used in each observing season, in order to expand the u-v coverage and to optimize it for sources at different declinations. The abundant telescope pads at the intersection of the north-south and east-west arms and the small telescope size allow a large number of short baselines. Typical u-v coverage for a high-declination and for a low-declination source are shown in Figure 2.6.

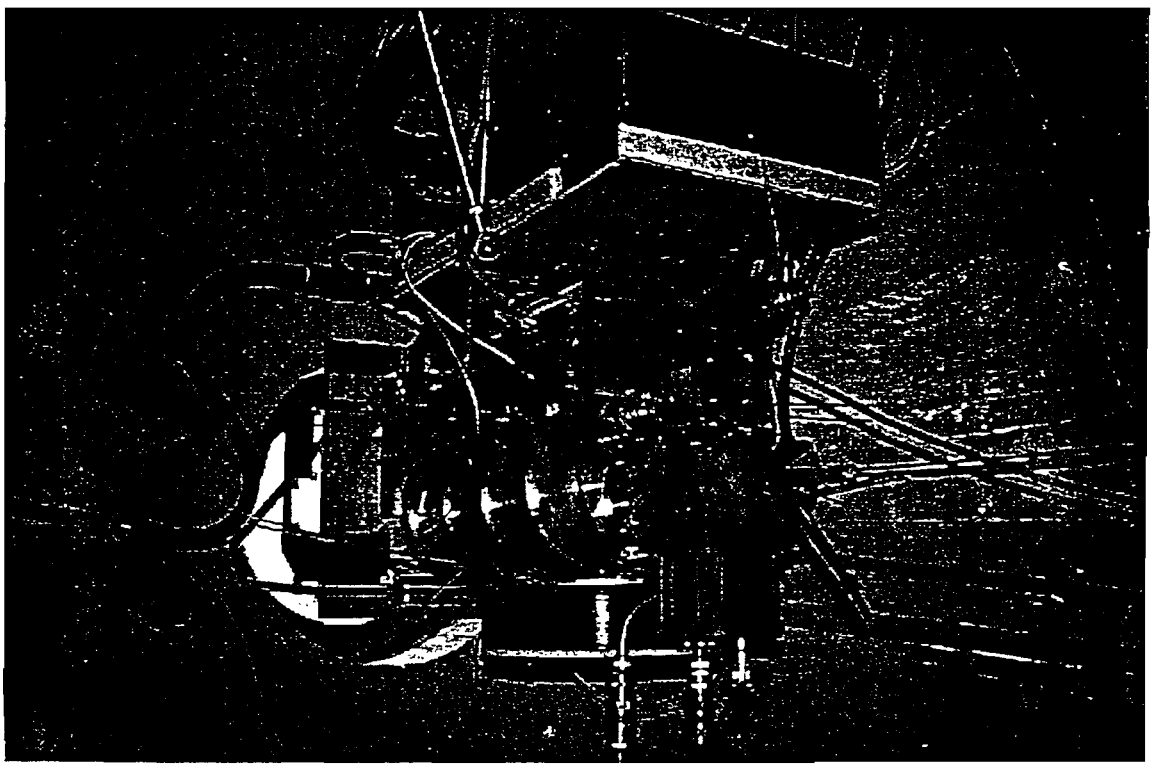

Figure 2.7 The centimeter-wave receiver is mounted in place of the millimeter receiver in the BIMA receiver cab.

Holographic measurements of each antenna's beam pattern were made. The beam patterns for each telescope are very similar, the FWHM varying maximally by ~3%. The primary beam is determined to be nearly Gaussian with a 380″ FWHM.

Chapter 3

Data Reduction and Calibration

3.1 Interferometer Data

Before discussing the details of this particular interferometry experiment, a brief introduction to interferometry concepts, especially the form of interferometry data and how they are measured, will be useful. Following this introduction, the reduction and calibration protocol for the OVRO and BIMA interferometry data will be discussed in Sections 3.2 and 3.3.

An interferometer measures the spatial coherence function, modified by the instrumental response, of a source of interest. The spatial coherence function is the correlation of the electric field measured by the two interferometer elements. A multi-element interferometer can be viewed as an assembly of N(N-1)/2 two-element interferometers, where N is the number of elements. The response of a two-element interferometer to a complicated astronomical source can be viewed as the response of the interferometer to an assembly of point sources. Therefore, a simple description of the response to a point source can be used to understand the response to extended objects. Here we follow the derivation of Perley, Schwab, & Bridle (1994).

A coordinate system in the plane of the sky can be defined as (x, y, z), where x and y are direction cosines in the north and east directions and $(0, 0, 1) = \hat{s}_o$, where

$\hat{\mathrm{s}}_\circ$ is set to be the direction from the interferometer to a fiducial point, the "phase tracking center." The phase tracking center can be kept at the center of the observed object while it transits by compensating for the geometrical delay, θ_g, the difference in electrical path length from the source to the two telescopes. A point source not at the phase center will have an associated phase since its geometrical delay will be different. Defining $\mathbf{B}$ as the vector connecting the telescopes, called the baseline vector, and s the vector to the point source, the geometrical delay to the point source in direction s is

$$\theta_g = \mathbf{B} \cdot \mathrm{s} \, \frac{2\pi\nu}{c} = \frac{2\pi \mathbf{B}}{\lambda} \cdot (\hat{\mathrm{s}}_\circ + \Delta\mathrm{s}), \tag{3.1}$$

where ν and λ are the observing frequency and wavelength. The expression $\frac{2\pi\mathbf{B}}{\lambda} \cdot \hat{\mathrm{s}}_\circ$ is simply the geometrical delay to the phase center. Since this delay can be compensated for dynamically, we set this to be zero, *i.e.*, the phase center is defined to have $\theta_g = 0$. And so $\frac{2\pi\mathbf{B}}{\lambda} \cdot \Delta\mathrm{s}$ is a residual phase, the phase of the point source.

The vector connecting the telescope pair, the "baseline," can be expressed in the same coordinate system, and measured in units of $\lambda = c/\nu$. These coordinates are denoted (u, v, w), where w is in the direction of $\hat{s}_\circ$, v is north, and u is east. And so

$$(u, v, w) = \left(\frac{\mathbf{B} \cdot \hat{\mathbf{x}}}{\lambda}, \frac{\mathbf{B} \cdot \hat{\mathbf{y}}}{\lambda}, \frac{\mathbf{B} \cdot \hat{\mathbf{z}}}{\lambda} \right), \tag{3.2}$$

and

$$\frac{\mathbf{B} \cdot \Delta\mathrm{s}}{\lambda} = ux + vy$$

and

$$\theta_g = 2\pi(ux + vy).$$

The brightness distribution, in units of intensity, of an astronomical source on the sky can be described in the sky coordinates, $I = I(x, y, z)$. We make the simplification that the region of interest comprises a small area of sky, and that the brightness distribution is adequately two dimensional, $I = I(x, y)$ and $V_\nu(u, v, w) = V_\nu(u, v)$.

The beam patterns of the antennae, $A_\nu(x,y)$, are assumed to be identical for each telescope. $A_\nu(x,y)$ is also referred to as the primary beam. We also assume that astronomical sources are incoherent spatially, and that the measurements are quasi-monochromatic (hence the subscript ν.)

The response of a two-element interferometer to a point source at position $\hat{s} = (x_\circ, y_\circ)$ is related to its flux $I_\nu(x,y) = I_{\nu\circ}(x_\circ, y_\circ)$ in this way:

$$V_\nu(u,v) = A_\nu(x_\circ, y_\circ) I_{\nu\circ}(x_\circ, y_\circ) e^{-2\pi i(ux_\circ + vy_\circ)}. \tag{3.3}$$

The spatial coherence function of an extended brightness distribution can be derived by adding the spatial coherence functions of the point sources which would comprise such a brightness distribution.

$$V_\nu(u,v) = \int_{-\infty}^{+\infty}\int_{-\infty}^{+\infty} A_\nu(x,y) I_\nu(x,y) e^{-2\pi i(ux+vy)} dxdy \tag{3.4}$$

$V_\nu(u,v)$ is called the visibility function, and is measured in units of intensity. $V_\nu(u,v)$ is a complex number, and contains information about the phase of the source with respect to the phase center.

The sky brightness, modified by the instrument response, or the primary beam, can be recovered from the visibility function,

$$A(x,y) I_\nu(x,y) = \int_{-\infty}^{+\infty}\int_{-\infty}^{+\infty} V_\nu(u,v) e^{2\pi i(ux+vy)} dudv. \tag{3.5}$$

The primary beam, $A(x,y)$, is a measurable function and so the brightness distribution can be recovered by dividing the transformed visibility function by the beam.

In practice, each telescope pair measures one visibility, $V(u,v)$, in a given amount of time. The telescopes follow the source across the sky, and the phase tracking center is kept at the same place on the source. As the baseline vector rotates with respect to $\hat{s}_\circ$, different visibilities are measured. In practice, the u-v plane will not be completely sampled, and therefore the sky brightness cannot be fully recovered. The

function $S_\nu(u,v)$, which is unity at u-v pairs where data are taken, and zero elsewhere, describes the u-v sampling. The recovered brightness distribution is referred to as the *dirty image.*

$$I_\nu^D(x,y) = \int_{-\infty}^{+\infty}\int_{-\infty}^{+\infty} S_\nu(u,v)V_\nu(u,v)e^{2\pi i(ux+vy)}dudv. \tag{3.6}$$

The relation of the dirty image to the real brightness distribution is

$$I_\nu^D = (I_\nu A_\nu) * B, \tag{3.7}$$

where $*$ denotes convolution, and

$$B(u,v) = \int_{-\infty}^{+\infty}\int_{-\infty}^{+\infty} S(u,v)e^{2\pi i(ux+vy)}dudv \tag{3.8}$$

is the *synthesized beam.*

By choosing the u-v sampling carefully, the synthesized beam can be altered in order to maximize response to a particular observed source structure. For cluster observations, care can be taken to make measurements with short ($\leq 1.5\mathrm{k}\lambda$) projected baselines, so that the synthesized beam is well suited to the angular scales of the clusters.

The true cluster brightness distribution can be recovered to some extent through a process called CLEAN. The CLEAN algorithm deconvolves the synthesized beam from the dirty image and creates a "clean image" from the CLEAN components. The CLEAN components are obtained by iteratively removing the flux from the brightest point in the clean map, multiplied by the synthesized beam and a CLEAN loop gain. The flux of the source is effectively broken up into an assembly of point sources, or CLEAN components. The clean map is created by adding in the CLEAN components convolved with a Gaussian FWHM approximation to the synthesized beam. The process is nonlinear, and it cannot recover the contribution to the brightness distribution from visibilities which have not been measured, but a clean map does contain a good deal of information about a source.

Figure 3.1 illustrates the interferometric method discussed. The top left figure is the simulated sky brightness distribution of a cluster at z=0.3. The top right figure is the synthesized beam for a typical interferometric cluster observation. The bottom left figure is the dirty map of the cluster, using the synthesized beam shown and a sampling function and observing time taken from a typical cluster observation. The bottom right figure is the CLEANed image, the result of deconvolution of the synthesized beam and the dirty image.

Visibility data are measured with interferometers in the following way. The signal of interest, as well as emission from the atmosphere and other sources of noise, is received by the telescope, amplified and then converted to a lower frequency at which analysis is technically simpler. The downconverted signals are passed through a set of delay lines, usually pieces of cable of varying electrical path length, which compensate for the geometrical delay, the difference in path length from the source to the different telescopes. The delay compensation is updated continually, and allows the phase center to remain at the same place on the source.

The signal and atmospheric noise, plus any additional noise introduced by the receiver system, are analyzed by a complex correlator, which actually performs the operation in Equation 3.4 for each baseline. Generally, the correlations are performed on the signal which has been integrated over a period of time, the period set by the required S/N. The noise in a visibility measurement is proportional to $T_{sys}/\sqrt{\Delta\nu\Delta t}$, where T_{sys} is the system temperature, including the noise from the atmosphere and the receiver system; $\Delta\nu$ is the correlator input bandwidth; and Δt is the integration time. The system temperature is a convenient representation of the system noise. T_{sys} is defined to be the physical temperature of a matched termination to the beam beyond the earth's atmosphere which would produce the same power, P_N, at the correlator input.

$$T_{sys} = P_N/k\Delta\nu G, \tag{3.9}$$

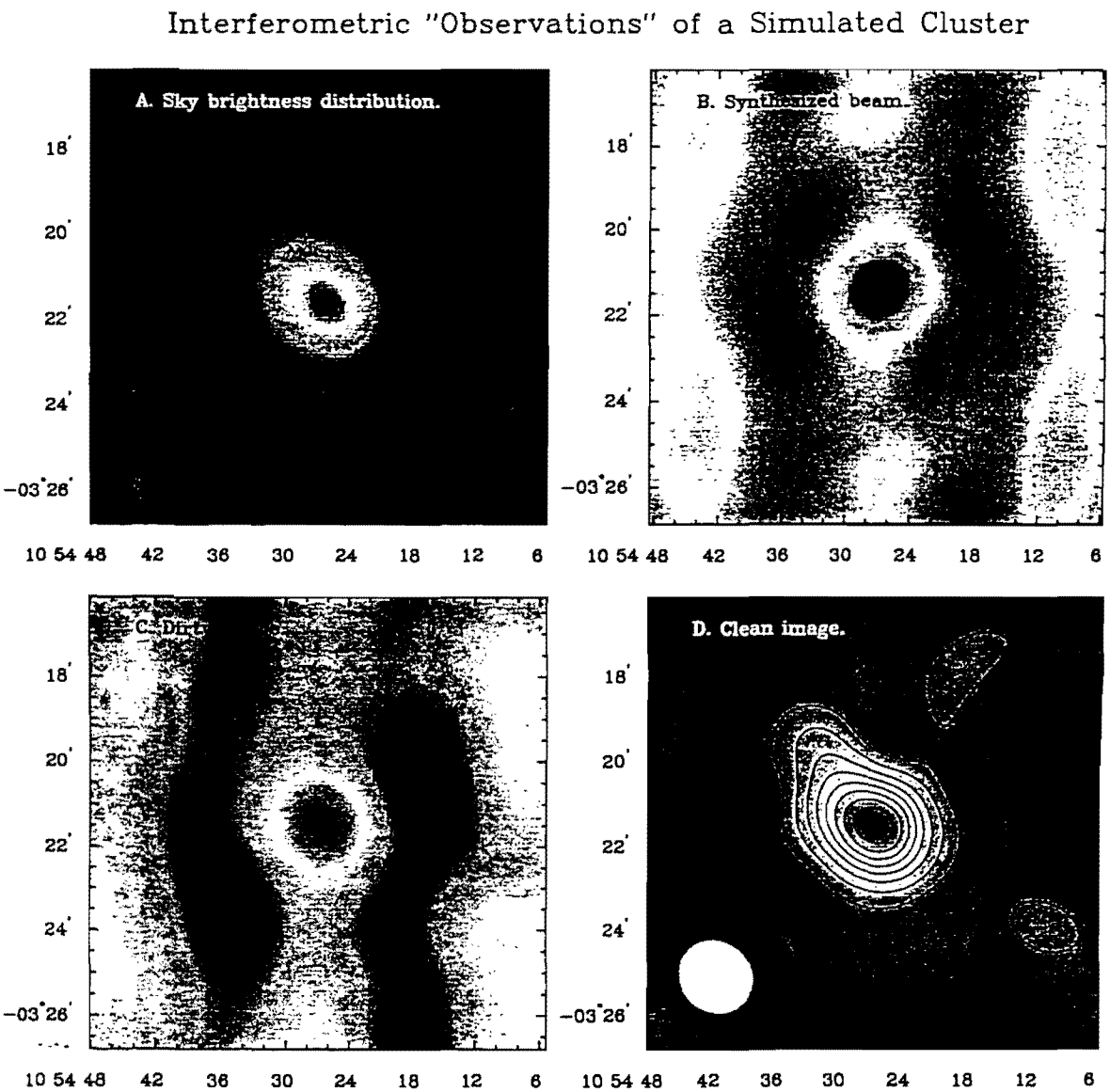

Figure 3.1 An illustration of the interferometric method: The top left figure is the simulated sky brightness distribution of a cluster at redshift 0.3. The axis units are arcseconds and the center of the image is the phase tracking center. The top right figure is the synthesized beam for a typical interferometric observation of a cluster. The bottom left figure is the dirty map of the cluster, using the synthesized beam shown and a sampling function and observing time for a typical cluster observation. The bottom right figure is the CLEANed cluster image, the result of deconvolution of the synthesized beam and the dirty image.

where G is the total instrument and atmosphere gain and k is Boltzmann's constant. The power due to an astronomical source can be denoted in a similar way, as an antenna temperature, T_a. A portion of the power will be due to the correlated flux, T_{vis}.

$$T_{vis} = P_{vis}/k\Delta\nu G \tag{3.10}$$

The power input to the correlator will be proportional to $T_{sys} + T_a$. Since the noise should be uncorrelated, T_{vis} can be recovered as $\rho_{corr} \times (T_{sys} + T_a)$, where ρ_{corr} is the correlation coefficient from the operation in Equation 3.4. For the experiment we are considering, $T_a << T_{sys}$. The visibilities are measured in units of flux, S_a, where

$$S_{vis} = 2kT_{vis}/A\eta_a, \tag{3.11}$$

and A is the geometrical area of the telescope, and η_a is the aperture efficiency.

3.2 OVRO Reduction

The observing strategy was devised to maximize the usable observing time on the galaxy cluster while providing good instrument calibration. The cluster observations, typically six sets of four minute observations, are interleaved with observations of a nearby radio-bright reference source (the gain calibrator), typically observed for one or two minutes, in order to monitor the instrumental amplitude and phase gain. The pointing model is generally updated with every calibrator observation. The pointing model predicts how the direction of the maximum telescope gain changes with respect to the azimuth and elevation encoder readouts. A primary calibration source, either a planet or other bright, stable radio source, is observed sometime during the several hour time period spanned by the observation of a given cluster, here called a "track." If Mars is at least 15° above the horizon, it is always observed.

After the telescopes are moved to the desired configuration, the exact (to within a fraction of a millimeter) positions of the telescopes are derived by observing a large set of radio-bright sources with known coordinates. These sources are located all over the sky. The relative phases of the sources as measured by the array of telescopes are used to determine very accurately the positions of the telescopes, and to derive the correction to the assumed positions. This correction, the baseline correction, can be applied to the data online or during the calibration process.

The OVRO datasets were archived, edited, and calibrated using the MMA data reduction package (Scoville *et al.* 1993). Much of the data editing and some of the calibration is performed online automatically by the array control software, CMA. The data are edited according to several criteria. Data taken with a telescope which is blocked by another telescope (shadowed) are removed from the data set. The shadowing limit used is conservative; data taken when the projected baseline is less than 1.05 times the telescope diameter are deleted. Data taken during poor weather, as evidenced by poor phase stablity, are removed, as are any data affected by anomalous jumps in the calibrator phase. Any cluster data not bracketed by calibrator observations are also removed.

The data are calibrated in two main steps, gain calibration and absolute flux calibration. For each dataset, the gain calibrator amplitude and phase are examined with MMA, gain corrections for each baseline are derived and these are then applied to the cluster data. The amplitude gain drifts of the telescope were minimal; the amplitude gain changes were less than a percent over a many hour track. MMA presents a time series of the gain observations, with a user-specified time-averaging length, generally about 20 minutes. This time series can be simply connected or fit by a polynomial, and the interpolated gains are applied to the cluster data. The amplitude gains are typically well fit by a 0- or 1-degree polynomial. The average gains for each baseline were quite stable from day to day. In observing seasons before

1996, however, the receivers responded to linearly polarized light. Since some of the gain calibrators are linearly polarized at the 5-10% level, the measured fluxes of such calibrators changes with parallactic angle. In theory, with observations at a wide range of parallactic angle, the polarization can be modeled and these flux variations can be detangled from the telescope gain variations. In practice, this is difficult. Fortuitously, only a few of the cluster observations are significantly affected, since two different gain calibrators were often used for a single cluster and in no case were both noticeably polarized. For the affected clusters, the average calibrator flux is used and the amplitude gain is assumed to be constant. It is not important to know the exact value of the gain calibrator's flux. Since the absolute calibration is done with respect to a primary calibrator, it is only important to be able to extricate the stability of the gains.

The gain calibrator phase is generally well fit by a second degree polynomial, and in stable weather the phase gain only drifts a few tens of degrees over the course of a cluster observation.

The absolute flux scale of the observations is determined relative to Mars. The brightness temperature of Mars is predicted using the Rudy model for Mars' whole disk brightness temperature (Rudy 1994) at the frequency at the center of the observed bandwidth. The Rudy model requires geometrical and electrical parameters as input. The geometrical parameters are Martian season, sub-Earth longitude and latitude, and sub-solar longitude and are interpolated from the Astronomical Almanac (1994-1998) for each day of observation. The default values of the electrical parameters (absorption length in wavelengths, surface dielectric constant and absorption length for the CO2 in the polar ice caps) are used except for the dielectric constant, which is set to 2.25, rather than 2.5, as suggested by Muhleman (private comm.). The accuracy of this model is expected to be 3-4%. For a given set of input parameters, the brightness temperature varies less than a percent over the range of

frequencies used in the SZ experiment. Since the typical Mars brightness temperatures are ~200 K, the flux of Mars can be determined using the Rayleigh-Jeans approximation, $S_\nu = 2kT_b\Omega/\lambda$, where S_ν is the flux, k is Boltzmann's constant, T_b is the brightness temperature, Ω is the solid angle subtended by Mars, and λ is the observing wavelength. Pre-1998, the Rayleigh-Jeans approximation was used. At the observed frequencies, ~30 GHz, the Rayleigh-Jeans approximation differs from the true blackbody temperature by ~0.3%. The equatorial and polar diameters of Mars are interpolated from the Astronomical Almanac in order to determine Ω.

The absolute calibration protocol evolved over the course of the experiment. The observations are flux calibrated in the data reduction stage. The primary and gain calibrators which were observable at the same time as Mars were calibrated against the predicted Mars flux. Since the amplitude gain of the instrument is stable in time and telescope elevation, the observations of these calibrators and Mars need not be contiguous. Should Mars not be observable at the same time as a given cluster and its gain calibrator, a "bootstrap" method is used, and the gain calibrator is flux calibrated against one of the other primary calibrators. A time-averaged flux for each clusters' gain calibrator is derived. The duration of each of these observation seasons was no longer than a month, and so no time variation of the gain calibrator fluxes were evident.

The datasets for each cluster are combined into one dataset for each correlator band and are written into a standard NRAO protocol u-v fits file for further analysis.

3.3 BIMA Reduction

The observing scheme employed at BIMA is similar to that as described in Section 3.2, with observations of the gain calibrator and cluster interleaved. Observations of primary calibrators are performed throughout the track until each primary calibrator

specified for that observing session has been observed. A bright source without line emission is needed to serve as a "passband calibrator," in order to establish the spectral response of the instrument. If the gain calibrator isn't sufficiently bright to serve as a passband calibrator, an additional bright source is observed. Pointing data are collected daily, and they are reviewed and the model updated periodically.

The baseline solution is determined in the same method as at OVRO.

The BIMA datasets are stored as standard MIRIAD data files. The MIRIAD data files are actually directory trees which contain directories for each source observed (cluster, gain calibrator, flux calibrator), and each source's directory contains a raw visibility data file; a calibration file; and an editing, or flagging, file. The edits and calibration are applied 'on-the-fly' as the data are viewed, concatenated, or written out to a *u-v* fits file. MIRIAD (Sault *et al.* 1995) is a UNIX-based system, and calibration and editing can be completed very quickly with shell scripts. Little editing is done on-line, and so great care is taken to examine the data in the reduction stage.

The reduction proceeds in several steps. The observation of passband calibrator is used to examine the instrumental response versus frequency, *i.e.*, the passband. The channels at the edges of the passband are flagged, since the signal-to-noise ratio is very low at the filter edges. Any 'birdies', or channels with spurious interference, are also flagged. Also edited out are shadowed data, data taken with obviously incorrect or irregular system temperatures, data taken when the telescope tracked incorrectly, and data contaminated by interference from the correlator. The bandpass gains are derived and applied to the cluster and gain calibrator data. Then the spectral channels are vector averaged into one wideband channel.

The coaxial cables which serve as transport for the LO reference run underground, but still have some sensitivity to ambient temperature, and so their electrical path lengths change throughout the day. The cable lengths are constantly monitored and a *time*-dependent phase correction for the interferometer is derived and applied to the

dataset. The gain calibrator data are then used to determine the antenna based gains in a manner that does not alter the overall gain of the instrument. The gains are inspected, and typically a 0-degree polynomial is fit to the amplitude gain time series, and a second degree polynomial is fit to the phase gain time series. The interpolated gains are applied to the cluster data, and any cluster data not bracketed by gain calibrator observations are flagged.

After the complete reduction, the gain calibrator u-v data are mapped and inspected. If the point source flux is not recovered completely, it may suggest that some of the data have low coherence, and the dataset is inspected again.

Absolute flux calibration at BIMA evolved between the 1997 and 1998 seasons. For the 1997 data, each of the Mars observations were reduced in the method described above, and the resultant amplitude and phase are SELFCALed, deriving the antenna gains for each of the 10 telescopes. The absolute flux of Mars was derived using the Rudy model as described in Section 3.2. The gains were very stable over the two months of observing time, with an $r.m.s.$ antenna gain variation of of 1.2% for all telescopes all summer. Since the antenna gains were constant for the entire observing season, the average antenna gains were used for each dataset for the 1997 season. With the knowledge that the gains are steady, the 1998 antenna gains were derived against Mars in the first week of the 1998 BIMA observations, and these gains are applied online. The subsequent observations of Mars are monitored in order to detect any subsequent gain variation.

The datasets for each cluster are combined and written to a MIRIAD-supported data file, and this is converted to a standard NRAO protocol u-v fits file for further analysis.

Chapter 4

Data Modeling

As was discussed in Section 3.1, SZ data obtained from interferometric observations will necessarily be spatially filtered; the visibility function will not be measured at every spatial frequency. Therefore, in order to get a full description of the SZ effect in clusters, the data must be fit to a model. A description of this model and its attributes are presented in Section 4.1, the fitting procedure is discussed in Section 4.2, and the constraints derived on the fit parameters are shown and discussed in Section 4.3.

4.1 Galaxy Cluster β-Model

Since the SZ effect profile is determined by the density and temperature profiles of the ICM, the model used should be closely tied to the models generally used to fit the x-ray profiles of the ICM. The β-model (Cavaliere & Fusco-Femiano 1976, 1978) has been widely used to fit the density and temperature profiles of cluster galaxies and the ICM. This model is derived to be static and self-consistent. Assuming spherical symmetry, the gas density profile, $\rho_{gas}(r)$, and the galaxy density profile, $\rho_{gal}(r)$, are related to the temperature profile, $T(r)$, and the polytropic index, γ (which relates the gas pressure to the gas density, $p_{gas} \propto \rho_{gas}^{\gamma}$) in the following way:

$$\left(\frac{\rho_{gas}}{\rho_{ogas}}\right)^{\gamma-1} = \frac{T}{T_o} = 1 + \frac{\gamma-1}{\gamma}\beta\ \ell n\frac{\rho_{gal}}{\rho_{ogal}}, \tag{4.1}$$

where ρ_{ogas}, ρ_{ogal}, and T_o are the values of the gas density, galaxy density, and temperature at the cluster center, and β is the ratio of the specific kinetic energy in the galaxies to the gas.

$$\beta = \frac{\sigma_{vo}^2 \mu m_p}{kT_o}, \tag{4.2}$$

where σ_{vo}^2 is the cluster velocity dispersion at the cluster center parallel to the line of sight, μ is the mean molecular mass, m_p is the proton mass, and k is Boltzmann's constant.

The assumption that clusters are isothermal, and so $\gamma = 1$, simplifies the analysis and in light of limited evidence is a reasonable assumption. Spatially resolved ICM temperature measurements are not technically feasible for any but the nearest clusters; these are generally found to be isothermal in the central regions.

One of the most successful empirical approximations to the galaxy distribution in the central and intermediate regions is the functional form

$$\frac{\rho_{gal}}{\rho_{ogal}} = (1 + (r/r_c)^2)^{-3/2}, \tag{4.3}$$

called the modified King model, where r_c is a scale length, the core radius.

Under the isothermal assumption, and using Equation 4.3 for the galaxy distribution, the gas distribution takes the form

$$\left(\frac{\rho_{gas}}{\rho_{ogas}}\right) = (1 + (r/r_c)^2)^{-3\beta/2}. \tag{4.4}$$

We generalize the β- model to be spheroidally symmetric, rather than spherically symmetric, *i.e.*, the cluster is shaped like an ellipse revolved around one of its axes and is either a sphere or an ellipsoid. It is assumed that the mean molecular mass is constant througout the gas, and so the electron number density, n_e, should trace the gas density. In this model, the electron number density in a prolate ellipsoid is a function of $\eta^2 = r^2 + a^2 z^2 : a < 1$, where r and z are the radial and height coordinates in the cylindrical coordinate system, and a is the axis ratio of the two

unique ellipsoidal axes. If the ellipsoid is oblate, then the density is a function of $\eta^2 = a^2r^2 + z^2 : a < 1$. The electron density then follows a distribution:

$$n_e(r) = n_{eo}\left(1 + \frac{\eta^2}{r_c^2}\right)^{-3\beta/2}, \tag{4.5}$$

where r_c, the core radius, and β are fit parameters, and n_{eo} is the central electron number density. If the cluster gas is isothermal and its symmetry axis is in the plane of the sky, this density distribution leads to the following two-dimensional SZ temperature decrement:

$$\Delta T\,(\theta) = \Delta T(0)\left(1 + \frac{\theta_\eta^2}{\theta_c^2}\right)^{\frac{1}{2}-\frac{3\beta}{2}}, \tag{4.6}$$

where $\theta_\eta = \eta/D_A$, D_A is the angular diameter distance, $\theta_c = r_c/D_A$, and $\Delta T(0)$ is the temperature decrement at zero projected radius,

$$\Delta T(0) \propto T_e n_{eo} \int \left(1 + \left(\frac{l}{r_c}\right)^2\right)^{-\frac{3}{2}\beta} dl, \tag{4.7}$$

where the integral, dl, is along the line of sight. The spheroidal β-model distribution of the electron density projects to an elliptical β-model distribution of the SZ decrement.

4.2 Fitting Procedure

Again, the SZ temperature decrement is proportional to the Compton y-parameter (Equation 1.2),

$$y = \frac{k\sigma_T}{m_e c^2}\int n_e(l)T_e(l)dl,$$

where k is Boltzmann's constant, σ_T is the Thomson scattering cross section, m_e is the electron mass, n_e is the electron density, T_e is the electron gas temperature, and the integral extends along the line of sight (dl). The proportionality depends on the observing frequency and temperature, as noted in Equation 1.3.

$$\left.\frac{\Delta T_{SZ}}{T}\right|_{RJ} = \frac{yx^2e^x}{(e^x-1)^2}[x\coth(x/2) - 4 + \theta_e f(x)],$$

where $x = \frac{h\nu}{kT_e}$ and $\theta_e = \frac{kT_e}{m_e c^2}$, and the last term corrects for relativistic effects.

At 28.5 GHz, $\frac{\Delta T_{SZ}}{T} = -1.91y$ in the non-relativistic Rayleigh-Jeans (R-J) approximation, where T is the temperature of the cosmic microwave background radiation. We adopt the COBE FIRAS value of $T = 2.726 \pm 0.010$K (Mather *et al.* 1994). At 28.5 GHz, $f(x) = 7.08\text{x}10^{-3}$. Including the relativistic corrections for a temperature typical of massive clusters, $kT_e = 7$ keV, $\frac{\Delta T_{SZ}}{T} = -1.86\ y$.

Recalling from Section 3.1, the interferometer data are in the form of visibilities, *i.e.*, a measured amplitude and phase for each u-v pair, and are components of the Fourier transform of the sky brightness distribution; see Equation 3.4. The amplitude is measured in units of flux density.

The data and model are compared in the u-v plane. This avoids introducing into the modeling procedure the nonlinear process of deconvolving the data from the sampling. To evaluate a model, the two-dimensional SZ decrement which corresponds to the model is multiplied by the primary beam, and the Fourier transform of the product is taken at each for each u-v pair sampled by the interferometer, according to the sampling function $S(u,v)$ of Section 3.1. The model visibilities are compared to the measured visibilities, and a χ^2 analysis of the model space is performed. The model parameter space includes the following parameters: centroid position, β, θ_c, axis ratio (defined to be < 1), position angle (defined counter clockwise from north), and $\Delta T(0)$. The position and flux density of any radio-bright point sources are also fitted. The point source fluxes for each dataset are allowed to vary individually, since the primary beam attenuation is different for OVRO and BIMA, and the intrinsic point source flux can vary with time.

The fits are performed jointly on all datasets for a given cluster; some clusters have been observed at both OVRO and BIMA and over a number of seasons. The data at all u-v points available are used. The inner u-v radius cutoff is determined by the shadowing limit, *i.e.*, when the projected baseline is less than the diameter of a

telescope dish. For the BIMA data this limit is 0.58 $k\lambda$ and for the OVRO data it is 1 $k\lambda$. We use the holographically determined primary beam models when modeling the data, and the entire datasets are used to do the analysis.

4.3 Constraints on Fit Parameters

This approach to fitting the SZ data constrains the position of the cluster's center, its axis ratio and the positions and fluxes of the point sources very well. The fitting program consistently obtains the same values if the input values for these parameters are reasonably near (*i.e.*, within a beamwidth, 30″, of) the correct values. The initial guesses for the point source parameters are taken from inspection of the data imaged in DIFMAP (Shepherd *et al.* 1994), an interactive mapping program. The point source positions and fluxes are fit in DIFMAP, using the long baseline data in which the sensitivity to the SZ effect is expected to be low; these values are satisfactory inputs to the fitting program which fits the decrement and point sources concurrently.

When the cluster's center position, axis ratio, position angle, and the point source fluxes and positions are well-determined, these parameters are fixed to the best-fit values. To explore how well the shape parameters β and θ_c are constrained, a grid search is performed over a selected range of these parameters, and the remaining free parameter, $\Delta T(0)$, is allowed to take its best fit value. A grid of this kind for the cluster CL0016+16 is presented in Figure 4.3. In Figure 4.3A the axis ratio is fixed to 0.84, the best-fit value from the two-dimensional fitting, and in Figure 4.3B the axis ratio is fixed at 1.0. From the figure it is clear that β and θ_c are strongly correlated.

The full line contours are marked for $\Delta\chi^2 = 2.3$, 4.61, and 6.17 which indicate 68.3%, 90.0%, and 95.4% confidence, respectively, for the two-parameter fit. The dashed lines indicate $\Delta\chi^2 = 1.0$, 2.71, and 6.63. The projection onto the β or θ_c axis of the interval contained by these contours indicate the 68.3%, 90% and 99%

Figure 4.1 Confidence intervals for β and θ_c from a two-parameter fit to the OVRO and BIMA data for CL0016+16. A. Elliptical fit: The axis ratio is fixed to 0.84, the best-fit value from the two-dimensional fitting. B. Circular fit: The axis ratio is fixed at 1.0. The full line contours are marked for $\Delta\chi^2$ = 2.3, 4.61, and 6.17 which indicate 68.3%, 90.0%, and 95.4% confidence, respectively, for the two-parameter fit. The dashed lines indicate $\Delta\chi^2$ =1.0, 2.71, and 6.63. The projection onto the β or θ_c axis of the interval contained by these contours indicate the 68.3%, 90% and 99% confidence interval on the single parameter.

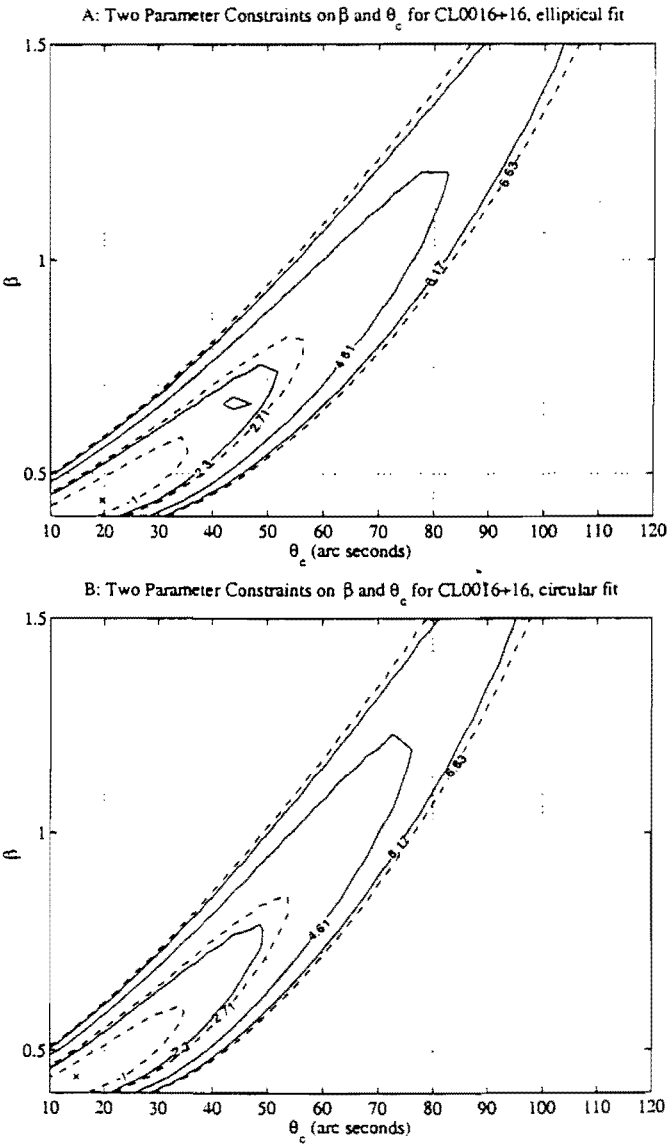

confidence interval on the single parameter. At each (β, θ_c) point, the values of $\Delta T(0)$ with $\Delta\chi^2 \leq 1$ range about 15% from the best fit $\Delta T(0)$ value. The fits are quite similar for both the circular and elliptical fits.

Chapter 5

SZ Gas Mass and Gas Mass Fraction Measurement Methods

The SZ effect measurements and the models fit to them are good indicators of a cluster's gas mass. Although the fit parameters β, θ_c and $\Delta T(0)$ are not strongly constrained individually, it will be shown in this chapter that together these parameters do constrain the gas mass quite well.

As discussed in Chapter 1, a measurement of the gas fraction in clusters can be of great use. In addition to the gas mass, a measurement of the total mass of the cluster is necessary. In this chapter are described our methods for calculating the gas masses and total masses of galaxy clusters. The simplest gas mass estimate to be made from the SZ effect is the surface gas mass, *i.e.*, the gas mass in a cylindrical volume with the long axis along the line of sight. Total masses measured with gravitational lensing methods probe this same geometry, and so it is natural to compare the two in order to measure a surface gas fraction. However, strong gravitational lensing in clusters is relatively rare and is restricted to the cores of clusters, and weak lensing analyses are published for only selected clusters, so a more general means of calculating the cluster baryon fraction is also considered. Using the fitted shape parameters, the gas mass is measured in a spheroidal geometry; the total mass in the spheroid can be

measured via the virial theorem, under the assumption that the gas is in hydrostatic equilibrium.

The gas mass calculation methods for cylindrical and spheroidal geometries are presented in Section 5.1. The total mass calculation methods, gravitational lensing and the hydrostatic method, are presented in Section 5.2. Systematic effects which may influence these measurements are discussed in Section 5.3.

5.1 Gas Masses from the SZ Effect

5.1.1 Surface Gas Mass

As is clear from Equation 1.2,

$$y = \frac{k\sigma_T}{m_e c^2} \int n_e(l) T_e(l) dl,$$

if the gas is isothermal, then the SZ brightness at any point in the two-dimensional projected cluster image is simply proportional to the integrated electron density along the line of sight. Under the isothermal assumption, we can directly measure the number of electrons in the gas contained in a cylindrical volume; the long axis of the cylinder is defined by the line of sight and the radius is chosen. Assuming a value for the number of nucleons per electron, the total mass in the ionized phase can be calculated from this. If the gas has solar metallicity, as measured by Anders & Grevesse (1989), the nucleon/electron ratio is 1.16. The nucleon/electron radio changes maximally a few percent for different metallicities, since the heavier elements compose only a small fraction of the total gas mass.

A model is fit to the u-v data in order to estimate the full, two-dimensional decrement, and so, within the validity of the model, all of the gas in the cylinder is recovered. The interferometric measurements recover a large fraction of the total SZ decrement without modeling. The flux solely recovered from a 7 keV cluster at z =

0.37 by the measured visibilites is 30-50% of the flux in the two-dimensional modeled decrement. The visibilities alone, then, provide a strong lower limit to the integrated SZ decrement.

This method of measuring the gas mass is not strongly model-dependent, is not sensitive to the details of the spatial distribution of the gas as long as the β-model provides a reasonable description of the gas distribution, and does not assume anything about the physics of the gas, apart from isothermality.

In order to determine the best-fit cylindrical gas mass at a particular radius, the gas mass is calculated at each point on a large (β, θ_c, $\Delta T(0)$) grid: a 40x40x40 grid with ($0.4 < \beta < 2.0$, $10 < \theta_c < 150$, $-600\mu K < \Delta T(0) < -3000\mu K$). This parameter range is adjusted if necessary to provide better resolution or to include a larger range of parameters, as an individual cluster warrants. Each set of parameters (β, θ_c, $\Delta T(0)$) are fit to the data, and a χ^2 statistic calculated. The best-fit gas mass is calculated at the best-fit parameters, and the $\Delta\chi^2 = 1$ range of masses determine the 68% confidence interval for the gas mass.

In order to convert the angular surface area to physical units, the angular diameter distance, D_A, to the cluster must be determined. To do this, we assume an ($\Omega_M = 0.3$, $\Omega_\Lambda = 0.0$) cosmology.

5.1.2 Gas Mass in a Spheroid

Calculation of a cluster's gas mass in a three-dimensional spheroid is more involved. This requires knowledge of the three-dimensional gas density distribution, including a fiducial value. The calculation is simplified considerably by making a few assumptions. We assume the gas is isothermal, so that the SZ effect profile traces the gas profile, and that the cluster obeys spheroidal symmetry with the symmetry axis in the plane of the sky. The surfaces of constant electron density are then concentric spheroids. The effects of relaxing these assumptions are discussed in Section 5.3.

To extract the central electron density, n_{eo}, for a given set of model parameters and measured electron temperature, we perform the integral in Equation 4.7.

$$\Delta T(0) \propto T_e n_{eo} \int \left(1 + \left(\frac{l}{r_c}\right)^2\right)^{-\frac{3}{2}\beta} dl,$$

where the integral, dl, is along the line of sight, and solve for n_{eo}.

The gas mass in any given volume can be calculated by integrating Equation 4.5,

$$n_e(r) = n_{eo}\left(1 + \frac{\eta^2}{r_c^2}\right)^{-3\beta/2},$$

using the derived central density and density profile and multiplying it by the nucleon/electron ratio of 1.16. Again, in order to derive $r_c = \theta_c D_A$, it is necessary to assume a cosmology.

This calculation also requires an assumption about the geometry of the cluster, since the core radius and extent of the cluster along the line of sight are not known. For an oblate ellipsoid, the axis of symmetry is the cluster's minor axis, and the core radius in the line-of-sight direction is equal to the cluster's observed major axis; for a prolate ellipsoid, the axis of symmetry is the major axis, The recovery of the three-dimensional structure of the gas is often denoted as "deprojection."

X-ray derived gas masses are also calculated by deprojecting the cluster density distribution; in fact, deprojection is strictly necessary for recovering the gas mass from x-ray observations, since the x-ray emission measure is proportional to $\int n_e^2 dV$. A profile is fit to the x-ray surface brightness, and the three-dimensional density profile is inferred, generally under the same assumptions made here. The x-ray and SZ derived gas masses may systematically differ. Should the density not vary smoothly, *i.e.*, if there is "clumping," described by the β-model, the x-ray shape parameters will be affected. If these clumps are pressure-supported, however, the SZ profile should not be affected. A comparison of the gas masses derived using each method would, in theory, provide an insight into the physics of the cluster gas.

5.2 Total Masses

5.2.1 Surface Total Masses from Gravitational Lensing

One of the predictions of the theory of General Relativity is that the trajectories of light rays are deflected by gravity. The magnitude of this deflection is twice that predicted by special relativity. This prediction was borne out beautifully by the observation of the gravitational influence of the Sun on the apparent angular position of background stars, observed during a solar eclipse in 1919. This bending of light, known as gravitational lensing, has become an incisive tool for observational cosmology. It is especially relevant for determining the total magnitude and spatial distribution of mass in massive objects like galaxy clusters. Gravitational lensing by a non-solar system object was first observed by Walsh, Carswell, & Weymann (1979) [as reported in Narayan & Bartelmann 1997]. This object, the quasar QSO 0957+561 A, B, was discovered to consist of two images of the same distant quasar separated by 6″. The lensing in this case is done by a galaxy. Massive galaxy clusters, $M_{cluster} \sim 10^{15} M_{\odot}$, are four or five orders of magnitude more massive than a single galaxy, and are thus expected to be strong lenses. Galaxy cluster gravitational lensing became an observational field in 1987, with the discovery of a giant lensed arc in the galaxy cluster Abell 370 (Soucail *et al.* 1987 a, b). Since this time, on the order of 20 galaxy clusters have had strong lensing reported in the literature (Le Fèvre *et al.* 1994; Wu & Fang 1997), and as deep optical imaging with high resolution has become a mature field with the the commissioning of the Hubble Space Telescope and large ground-based telescopes at excellent sites, like the Keck Telescope and the Canada-France-Hawaii Telescope, the number of lensing detections is rapidly increasing. The sophistication of the modeling of the lens potentials has kept pace with the observational advances. State-of-the-art models are able to produce high resolution mass maps; for instance, Tyson, Kochanski, & Dell'Antonio (1998) present a mass

map of the central 200 *kpc* of the cluster CL0024+1654, resolving structures on 10 *kpc* scales.

General relativistic analysis of the propagation of light in a curved spacetime in a general scenario is complicated. In practical terms, a number of simplifying assumptions are made. It is generally assumed that the universe's geometry is well-described by the Friedmann-Lemaître-Robertson-Walker metric, and that the gravitational potentials describing the observed phenomena are local perturbations. In the simplest models, we consider the light to travel in unperturbed spacetime between the source and the lens, and between the lens and the observer. The size of the lens is considered to be very small with respect to the other length scales in the geometry, the source-lens distance, D_{LS}; and the lens-observer distance, D_L. We can then assume a locally flat, Minkowskian spacetime near the lens, only weakly perturbed by the lens mass, and use the simplified Minkowskian spacetime curvature perturbed to first post-Newtonian order.

Astronomical gravitational lens systems are usually complicated structures, and require models with at least a modest level of detail. A simple example of lensing is suitable for illustrating the important components in a lens system, though. A lens with constant surface mass density equal to the critical density will focus perfectly. Surface mass density is determined by integrating an object's three-dimensional mass density along the line of sight: $\Sigma(r,\phi) = \int \rho(r,\phi,z)dz$, where cylindrical coordinates are used and z is along the line of sight. The critical mass density is (see, for example, Narayan & Bartelmann (1997))

$$\Sigma_{cr} = 0.35 \text{ g cm}^{-3} \left(\frac{D}{\text{Gpc}}\right)^{-1}, \tag{5.1}$$

where

$$D = \frac{D_{ds}}{D_d D_s}, \tag{5.2}$$

and D_d, D_s, D_{ds} the angular diameter distances between the observer and lens, lens

and source, and observer and source, respectively. To approximate the total mass within the Einstein radius, θ_{cr}, the critical mass density can be integrated within the area enclosed.

$$\mathrm{M}_{total} = \int_0^{\theta_{cr}} \Sigma_{cr} D_{ds}^2 \cdot \theta d\theta \int_0^{2\pi} d\phi \tag{5.3}$$

This integrated mass, derived under the assumption of a constant critical surface mass density, is not a perfectly accurate estimate of the mass within the arc, since lens systems are likely to be more complicated than this. Note, however, that with images and spectra (to obtain the source and lens redshifts) the total mass within a radius can be recovered in an uncomplicated way; the dynamical state of the matter does not affect the physics of this mass measurement. Note also that lensing probes the same geometry the SZ observations do. Lensing measures a surface total mass density and the SZ observations measure surface gas mass density.

The increase in quality of observations and the development of sophisticated analysis methods has also made weak gravitational lensing a powerful tool for investigating the masses of clusters. This method relies on a statistical analysis of the ellipticities and magnification of the images of background galaxies of a cluster in order to deduce the shape of its gravitational potential. Many investigations of weak lensing in clusters are reported in the literature (*e.g.*, Squires *et al.* 1996; Tyson & Fischer 1995), and this field is rapidly growing. Not all clusters will exhibit strong lensing, and so for a large sample comparison of lensing total masses to SZ gas masses, weak lensing would be the primary tool. The comparison is complicated by the fact that weak lensing shear measures the gradient of the potential, and so to normalize the mass distribution, one often has to fit a model for the gravitating mass and to integrate it.

5.2.2 Total Mass in a Spheroid from the Virial Theorem

The spatial distribution of the gas and its temperature constrain the underlying gravitational potential of the cluster, under the assumption that the cluster gas is in hydrostatic equilibrium and that it is supported only by thermal pressure. The total cluster mass, mainly dark matter, can then be calculated.

We develop here the method for calculating the total mass under the assumption that the gas is in HSE. Hydrostatic equilibrium implies

$$\frac{1}{\rho_{gas}}\nabla p_{gas} = -\nabla\Phi, \tag{5.4}$$

where ρ_{gas} and p_{gas} are the gas density and pressure, respectively. The cluster's gravitational potential, Φ, can be related to the total mass density, ρ_{grav}, by Poisson's equation,

$$\nabla^2\Phi = 4\pi G\rho_{grav}, \tag{5.5}$$

where G is the gravitational constant. We can solve for the density of the cluster's gravitational mass by combining Equations 5.4 and 5.5:

$$\rho_{grav} = -\frac{1}{4\pi G}\nabla\cdot\left(\frac{1}{\rho_{gas}}\nabla p_{gas}\right). \tag{5.6}$$

We relate the pressure, density, and temperature of the gas through the equation of state:

$$p_{gas} = \frac{\rho_{gas}kT_e}{\mu m_p}, \tag{5.7}$$

where k is Boltzmann's constant, μ is the mean molecular weight of the gas, and m_p is the proton's mass. To calculate μ, we again assume the gas has the solar metallicity of Anders and Grevesse (1989). We also assmue that μ is constant throughout the gas. The value of μ will change 3-4% depending on the solar metallicity measurements one

adopts; the metallicity in clusters is not well known, however, and although choosing μ incorrectly will incur a systematic error, it will be much smaller than the statistical errors involved. Making the assumption that the gas is isothermal, Equations 5.6 and 5.7 are combined in the form:

$$\rho_{grav} = -\frac{kT_e}{4\pi G\mu m_p}\nabla^2 \ln \rho_{gas}. \tag{5.8}$$

Note that the gravitational mass density depends only on the shape of the gas distribution, and is independent of the value of the central gas density. Using the derived shape parameters, β, θ_c, and projected axial ratio, a/b, and the measured gas temperature, we estimate the total mass density of the cluster. The density is integrated within the same spheroidal volume as the gas density. For simplicity, the mass derived with this method will be denoted the "HSE" mass.

For the same range of β, θ_c, and $\Delta T(0)$ as described in the Section 5.1.1, the cluster's ellipsoidal gas mass, virial mass, gas mass fraction, and χ^2 statistic in spherical, prolate and oblate spheroids are calculated and the 68% confidence intervals for the gas mass and gas fraction are calculated.

Since the fair sample assumption is best at large radii and the cores of clusters may be affected significantly by physical processes not included in our model (cooling flows, galaxy winds, magnetic fields), it is preferable to make gas fraction measurements at the largest radii the method permits. There are two constraints on this radius. The first limit arises from the model, the second arises from the observation scheme.

First, we consider the model. The two-dimensional SZ decrement is modeled as concentric ellipses, which imply, in an isothermal analysis, that the gas density is stratified on concentrically ellipsoidal shells. This, in turn, implies that the isopotential surfaces are concentric ellipsoids. The gravitating matter needed to produce concentrically ellipsoidal isopotential surfaces has a significantly more aspherical distribution than the resulting potential. For an observed axis ratio of 0.67, the dark

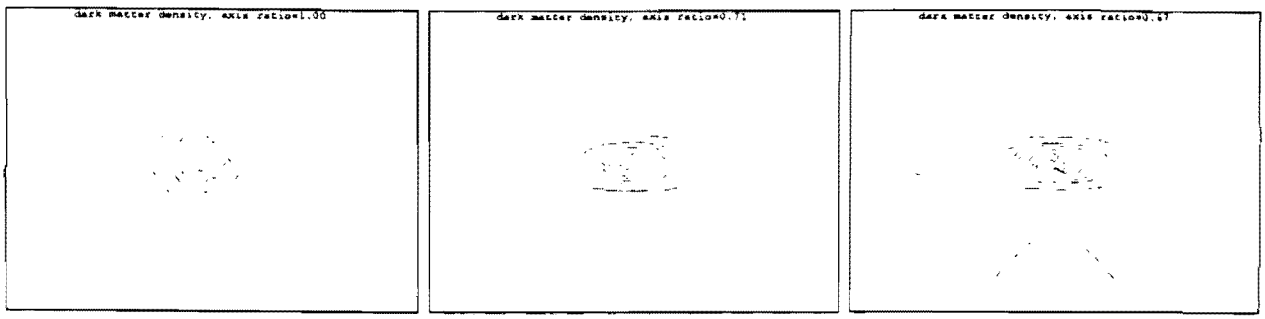

Figure 5.1 The dark matter density distribution required to support a concentrically ellipsoidal gas distribution with axis ratio A. 1.0, B. 0.71, and C. 0.67. The actual size scale depends on the core radius and β. The density distribution flattens faster than the gas distribution does. At axis ratios less than 0.7, *e.g.*, panel C., some negative density dark matter is required.

matter distribution becomes unphysical; beyond a few core radii in the direction of the minor axis/axes the gravitating matter density must be negative. If the cluster gas truly exhibits constant axis ratio with radius, this may suggest that the cluster potential is truly bimodal or perhaps even more complicated, since a simple supporting potential is impossible. However, it is more likely an indictment of the simplified models we have used. We have considered the class of potentials with isopotential surfaces following concentric ellipsoids because they adequately describe the observations and because their deprojections are straightforward. Such simplified models are seriously deficient, however, for the hydrostatic analysis; to produce a cluster with an observed axis ratio of less than $1/\sqrt{2}$ in this formalism, the cluster mass must be partially composed of dark matter with negative density. In Figure 5.1, the dark matter density needed to support concentrically ellipsoidal gas distributions is shown for increasing values of the gas distribution axis ratio. The dark matter distribution gets extremely flattened, and in the third panel, at axis ratios less than 0.7, some negative density dark matter is needed to support the gas distribution. It is improper, then, to measure the dark matter out past a few core radii for a highly elliptical cluster with this method.

In fact, a related problem in the field of elliptical galaxies has been studied at length in the literature. In Evans (1994), underlying density distributions are generated for potential surfaces which are stratified on similar concentric spheroids. The density profile functional forms are different from cluster β- models, but the general results agree. For moderately flattened galaxy potentials, the density distribution takes on a peanut-like shape, and for even more flattened potentials, some negative density matter must be introduced.

In order to fully take advantage of the two-dimensional information about the cluster gas, more physically realistic models should be used. De Zeew & Pfenniger (1988) derived a number of potential-density pairs for galaxies, some of which may be applicable to clusters. One of these models of particular interest may be a family of density distributions with surfaces of constant density stratified on concentric ellipsoids, which will produce potentials which become less flattened with increasing radius. An alternative may be to generate potentials physically motivated by numerical simulations of clusters. Suto *et al.* 1998 have derived families of cluster gas distributions generated from assuming an underlying dark matter density similar to the Navarro, Frenk, & White (NFW) universal density profile (Navarro, Frenk & White 1997), which could be extended to include elliptical clusters. The effects on the gas calculations of using this simplified model are discussed in Section 5.3.4.

A second constraint on the maximum radius for the gas fraction measurements is set by the observational scheme. It is unwise to extrapolate the fitted models beyond where they are constrained well by the data. The largest spatial scales on which information is available is limited by the shortest baselines on which the signal is detected significantly. To quantify this characteristic, the spheroidal gas masses as described in Section 5.1.2 and gas fraction determined using the HSE method of Section 5.2.2 are calculated at a number of different cluster radii. The fractional uncertainty in these measurements, $\Delta M_{gas}/M_{gas}$ and $\Delta f_g/f_g$, are measured as a function of cluster

radius. The minimum uncertainty is obtained when the radius is around 75″. This is a characteristic of the observational scheme. This cluster, A370, has high signal-to-noise (S/N) datasets from both OVRO and BIMA. It is, however, a low declination source ($\delta \sim -01°$), for which it is difficult to achieve good u-v coverage. This may also contribute to the constraint on angular radius. In Figure 5.3, the same calculations are presented for Abell 611, a cluster with SZ axis ratio of ~1.00, and which has a moderate declination, $\delta \sim 40°$, and was observed solely at OVRO. Note that there is a broad minimum in the uncertainty of the gas fraction calculations from about 50″ to 90″.

5.3 Systematic Effects

We consider the effects of the assumptions made in the gas mass and gas fraction calculations of the previous sections, including the assumption that the gas is isothermal and in hydrostatic equilibrium under thermal support only, and that the clusters are biaxial ellipsoids with their symmetry axes in the plane of the sky. Some other sources of possible systematic error are also discussed, *i.e.*, contamination of the emission-weighted temperatures, the simplified ellipsoidal β-model, and the radio point sources.

5.3.1 Emission-Weighted Temperature

The measured emission-weighted ICM temperature may be in error due to contamination from other sources in the viewing field. The Gas-Imaging Spectrometer (GIS) (Ohashi *et al.* 1996) on board *ASCA* is the preferred x-ray instrument with which to determine ICM temperatures for clusters. The spectral band over which it is sensitive (0.7-10 keV) and its modest spectral resolution ($\Delta E/E \sim 8\%$ FWHM at 6 keV) are more appropriate for this purpose than that of the *ROSAT* PSPC, which

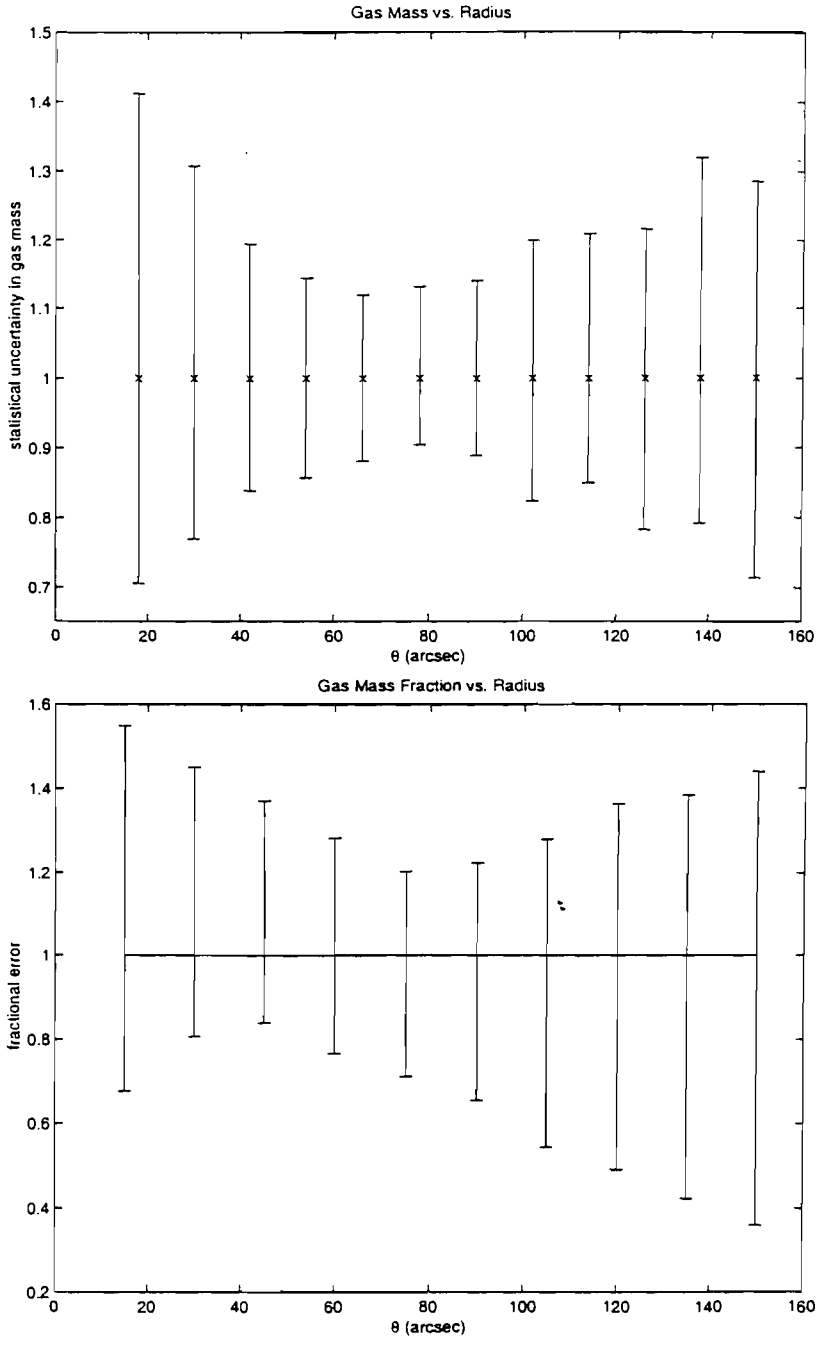

Figure 5.2 Uncertainties in the spheroidal gas mass and f_g vs. radius, for an elliptical cluster: the gas mass and gas mass fraction, calculated as a function of cluster radius. The total mass is calculated assuming hydrostatic equilibrium and isothermality. The SZ effect in A370 has an axis ratio of 0.672.

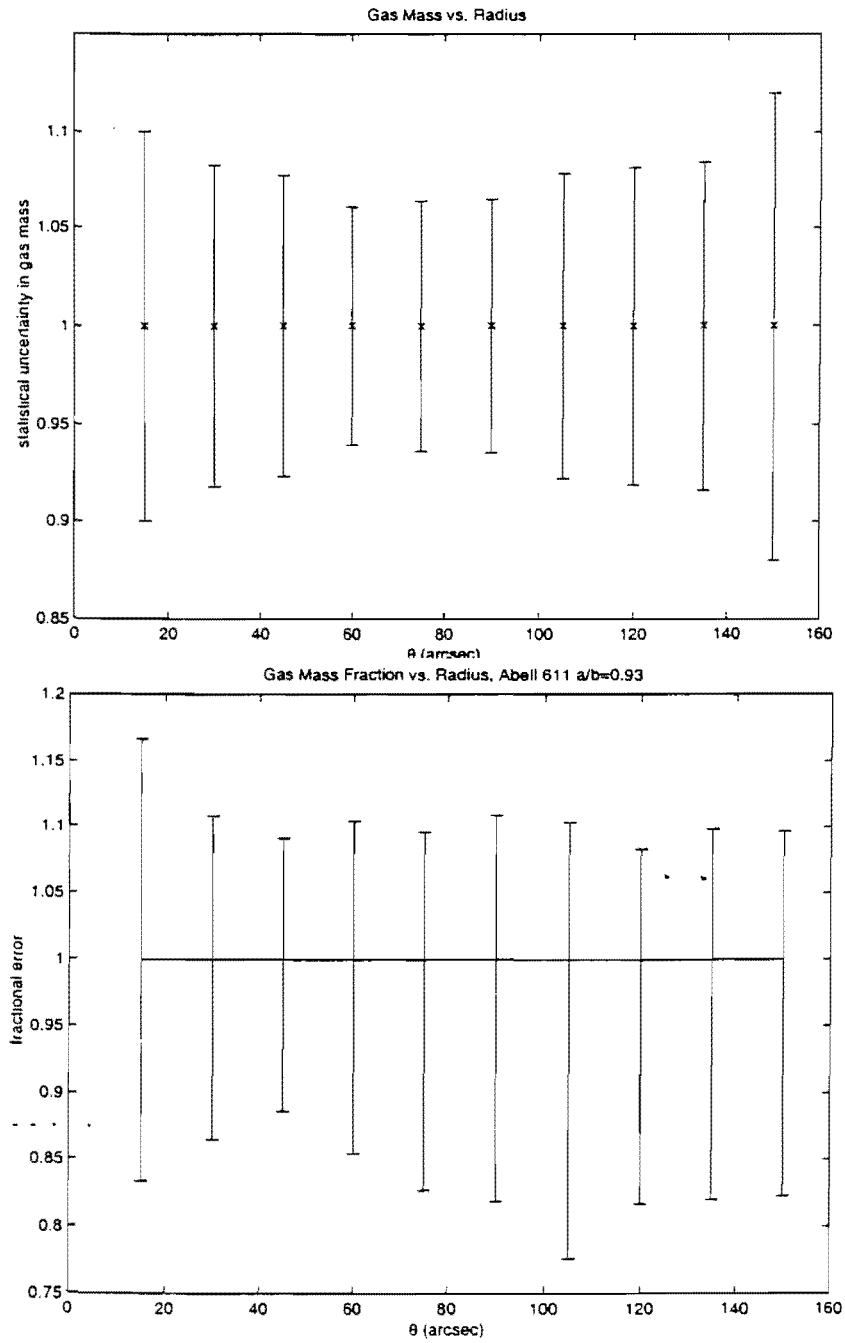

Figure 5.3 Uncertainties in spheroidal gas mass and f_g vs. radius, spherical cluster: the gas mass and gas mass fraction, calculated as a function of cluster radius. The total mass is calculated assuming hydrostatic equilibrium and isothermality. The SZ effect in A611 has an axis ratio of 0.93.

is mainly sensitive in the soft x-ray band (0.2 – 2.4 keV) and has limited spectral resolution ($\Delta E/E \sim 40\%$ at 1 keV). The GISis more efficient than the *ASCA* Solid-State-Imaging Spectrometer (SIS) at high energies (> 4 keV), the spectral region of interest for galaxy clusters. The *ASCA* telescope angular resolution, however, makes it difficult to make spatially resolved temperature measurements of clusters except in those with z<< 0.1; the half-power diameter is $\sim 3'$. Therefore, if there is a contaminating source in the field, *e.g.*, a nearby AGN or another cluster in the field, this temperature may be in error. The effects of temperature structure within the cluster will be discussed in the next section.

The SZ gas mass is inversely proportional to the assumed temperature: $M_{gas}(\mathrm{SZ}) \propto 1/T_e$ and the total mass measurement with the HSE method is directly proportional to T_e: $M_{HSE} \propto T_e$. The gas fraction then will be quite sensitive to temperature: $f_g \propto 1/T_e^2$, and $\Delta f_g/f_g \propto 2\Delta T_e/T_e$.

5.3.2 Temperature Gradients

We consider the cluster's gas to be isothermal because it significantly simplifies the analysis, and there is only limited evidence available suggests it is reasonable. Here we consider the systematic effects of both a gradual, negative temperature gradient, and of a cooling flow in the cluster core.

A negative temperature gradient in the gas which has not been resolved by observations will systematically affect the gas and virial masses. The existence of such a temperature gradient implies that the true temperature in the central region is higher than the emission-weighted temperature used in the isothermal analysis. Since the emission measure is proportional to n_e^2, the emission-weighted temperature will be most sensitive to the cores of clusters. So in the presence of an unresolved temperature gradient, the emission-weighted temperature will be in error.

An additional effect of such a gradient is that the fitted shape parameters from the

isothermal analysis will no longer describe the gas density. If a negative temperature gradient is truly present, the density profile declines with radius more slowly with radius than the SZ decrement does. A temperature gradient also affects the derived HSE mass. An underestimated central temperature effects an underestimation of the HSE mass in the central region, but the declining temperature makes the isothermal virial mass an overestimate at larger radii. Thus, the magnitude and even the sense of the error in the gas mass fraction will depend on the exact shape parameters, temperature profile, and the radius at which the masses are measured.

Temperature structure may also exist in the cores of clusters. The gas in the central regions of some clusters, presumably radiatively cooled by thermal bremsstrahlung emission, has become sufficiently dense that cooling becomes quite efficient, and the temperature drops. These cooling flows (see review of the subject in Fabian 1994) are generally identified by enhanced x-ray emission in the centers of clusters and the presence of iron lines characteristic of cool gas in the spectra. Should these central regions be pressure-supported, they should not generate an SZ excess in the central regions. The emission-weighted temperatures measured with the *ASCA* GIS will generally not be strongly affected by cooling flows, since cooling flows only account from 10-30% of the x-ray luminosity, and the cooling flow characteristic temperatures of 1-2 keV are near the low-energy cutoff of *ASCA* GIS. Fabian *et al.* (1994) suggest that cooling flows may bias the emission-weighted temperature by 0.5-1 keV for the most massive cooling flows. They also, however, suggest that clusters with cooling flows deviate from their derived luminosity-temperature relation. These deviations appear to increase in magnitude with the mass of the cooling flow, beyond what is expected from the cooling flow itself. A likely explanation is that gas may tend to be "clumped" when in this relaxed, dynamical state. If these clumps are pressure-supported, then the SZ-derived shape parameters are unlikely to be affected. If an SZ cluster is also a cooling flow cluster, the most likely systematic effect is that

the temperature will be underestimated by 10-20%.

5.3.3 Inclination Angle and Cluster Geometry

Certainly, the assumption that clusters are biaxial, and all with symmetry axes in the plane of the sky, is a simplification. The observed brightness distribution could also be produced by a cluster with its symmetry axis inclined to the plane of the sky and a different intrinsic density distribution.

Analytical relationships between the inclination angle and the shape parameters of an spheroidal object are derived for triaxial spheroids in Stark (1977) and biaxial spheroids in Fabricant, Rybicki, & Gorenstein (1984). Retaining the simplifying assumption of biaxiality, the cluster gas mass and HSE mass is derived for a cluster which gives the observed SZ map but with an inclined symmetry axis. The inclined cluster retains a β-model distribution, and the same value of β, but the central density and intrinsic axis ratio change with inclination angle, i, in order to be consistent with the observations. The angle i is measured between the symmetry axis and the line of sight, where $i = 90°$ for a cluster with symmetry axis in the plane of the sky.

The relationship between intrinsic axis ratio, a_i, and the inclination angle, i, for an oblate ellipsoid is

$$a_i = a\frac{[1 - a^{-2}\cos^2(i)]^{1/2}}{\sin(i)}, \tag{5.9}$$

where a is the observed axis ratio. For a prolate ellipsoid,

$$a_i = a\frac{\sin(i)}{[1 - a^2\cos^2(i)]^{1/2}}. \tag{5.10}$$

The gas mass and gas fraction are presented for several values of inclination angle, using the shape parameters β=0.7, θ_c=60″, and $\Delta T(0)$=-1000μK, and a rather extreme value of axis ratio, a/b=0.65. The gas mass remains the same for all inclination angles, which is to be expected since the gas mass is proportional to the total SZ flux, independent of how it is arranged spatially.

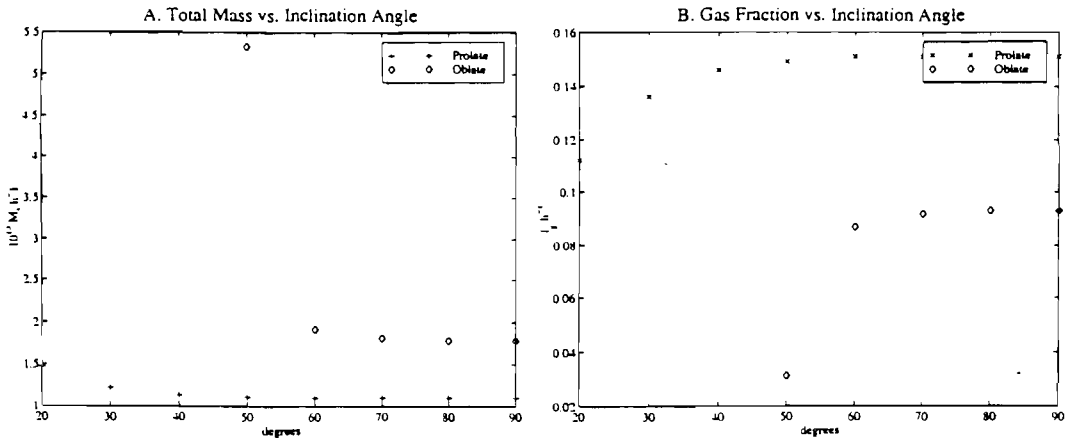

Figure 5.4 Change with inclination in derived HSE mass and gas fraction of an ellipsoidal cluster's symmetry axis. A. The total mass, calculated with the hydrostatic, isothermal method, as a function of inclination angle. B. The gas mass fraction as a function of inclination angle, where the total mass is calculated with the hydrostatic, isothermal method. The angle is measured between the symmetry axis and the line of sight; if the symmetry axis is in the plane of the sky, $i = 90°$. The gas fraction is calculated using the β=0.7, θ_c=60″, and $\Delta T(0)$=-1000μK, and a/b=0.65.

For both oblate and prolate geometries, the total mass at 65″ changes only a small amount over a broad range of inclination angle. As inclination angle increases, so does the intrinsic axial ratio; the HSE potential is affected as well as the volume included. And so, for a large range of inclination angle, the gas fraction remains relatively unchanged. (See Figure 5.4.)

We conclude that, for a broad region of parameter space, however, inclination is not an important source of uncertainty in the HSE gas fraction calculation. Since the cylindrical gas mass does not require deprojection, it will be unaffected by inclination altogether.

5.3.4 Simplified β-Model

As mentioned previously, the concentrically ellipsoidal β-model is inadequate for HSE analyses of even moderately elliptical clusters. This problem will significantly affect

the analysis of large samples of clusters. Of the 58 clusters with emission-weighted axis ratios reported in Mohr *et al.* (1995), 13 have projected axis ratios less than $1/\sqrt{2}$; the fraction of clusters with intrinsic axis ratios less than $1/\sqrt{2}$ should be larger still.

The effect on the calculated gas fractions of using this simple ellipsoidal model is assessed in the following way. We construct a model cluster, predict its observed SZ effect, and then attempt to recover the simulated cluster's mass using the same observation and analysis protocol used for the true observations. The dark matter of the simulated cluster is arranged in concentrically spheroidal shells with a β-model profile, a more physically realistic model than that necessary to support concentric isopotentials. The dark matter's axis ratio is set to 2.0:3.5. Isothermal gas at 7 keV is added in hydrostatic equilibrium with the cluster potential. A simulated two-dimensional SZ decrement map is then constructed, assuming the cluster is at redshift z = 0.37. The decrement map is sampled with the u-v coverage of a typical interferometric observation and noise typical of a long observation is added. The resulting u-v data are analyzed in the manner described in Chapter 4, *i.e.*, the data are fit to a concentrically ellipsoidal β-model. The gas and dark matter masses are determined with the HSE method of Chapter 5. Two simulated clusters are analyzed; one is an oblate spheroid and the other is a prolate spheroid, both with the symmetry axis in the plane of the sky. In both cases, the best fit projected axis ratio of the gas distribution as determined from the simulated SZ observations was 0.79. These gas masses and gas fractions are compared to the actual model input values in Table 5.3.4.

The model appears to be adequate at small radii, but deteriorates noticeably by a radius of 100″. This suggests it is reasonable to measure the gas fraction this way at the radius where we constrain the model well. For now, we have restricted our analysis to within radius of 65″, a region within which the approximation is valid. A carefully considered alternative model, one which describes a more realistic matter

Table 5.3.4: Comparison of Fitted to Actual Mass and Mass Fractions, Using Elliptical Fits

	at 65″	at 65″	at 100″	at 100″
Oblate, $i = 90°$	**true value**	**derived value**	**true value**	**derived value**
dark matter ($10^{13} M_\odot$)	6.30	$6.6^{+0.5}_{-0.5}$	12.7	$18^{+2.0}_{-5.5}$
gas ($10^{13} M_\odot$)	0.49	$0.48^{+0.4}_{-0.4}$	1.07	$1.03^{+0.15}_{-0.13}$
gas fraction	0.078	$0.075^{+0.015}_{-0.015}$	0.084	$0.055^{+0.030}_{-0.005}$
Prolate, $i = 90°$	**true value**	**derived value**	**true value**	**derived value**
dark matter ($10^{13} M_\odot$)	3.63	$3.2^{+0.6}_{-0.6}$	7.32	$8.5^{+2.0}_{-4.0}$
gas ($10^{13} M_\odot$)	0.30	$0.26^{+0.08}_{-0.02}$	0.74	$0.65^{+0.25}_{-0.10}$
gas fraction	0.081	$0.09^{+0.05}_{-0.02}$	0.101	$0.08^{+0.11}_{-0.02}$

distribution, should be an improvement on this.

5.3.5 Non-thermal Pressure Support

Recent comparisons of cluster total masses derived by gravitational lensing models to those derived by the HSE method suggest that the HSE method may systematically underpredict the cluster's total mass by a factor of 2-3 (Miralda-Escudé & Babul 1994; Loeb & Mao 1994; Wu & Fang 1997). Some of the suggested explanations for the discrepancy include extension of the cluster along the line of sight, a temperature gradient in the gas, both of which have already been discussed in this section, and non-thermal pressure support of the gas in the cluster core.

It has been suggested that clusters which exhibit strong lensing also may be dynamically active and therefore the HSE approximation may not be valid. It is also possible that projection effects affect cluster lensing. A lensing cluster may have a chance alignment with another cluster or group, which would preferentially increase

the mass measured by the lensing method. Bartelmann & Steinmetz (1996) used simulations to investigate the biases in gravitational lensing measurements in clusters, and concluded that clusters selected for gravitational lensing typically do exhibit substructure and dynamical activity. They also conclude, though, that, rather than a failure of the HSE method, projection effects are the primary cause of discrepant x-ray and lensing masses.

Non-thermal pressure sources could include bulk cluster flows or magnetic fields. Loeb & Mao (1994) argue that magnetic field pressure may be a significant source of pressure in the central region of Abell 2218, and could explain the entire mass discrepancy. Intracluster magnetic fields are typically a few μG (Kim *et al.* 1990; Taylor & Perley 1993), an order of magnitude smaller than the level at which the fields would contribute significantly to the dynamics of cluster gas, although stronger fields, $\sim 10 - 100\mu$ G, have been measured in a few clusters (Taylor & Perley). A subsequent comparison of weak lensing with the HSE mass in A2218 found the two mass estimates to be consistent within the experimental uncertainties (Squires *et al.* 1996), but it remains to be shown by further investigations whether magnetic fields play a strong role in the physics of cluster gas.

In some cases the mass discrepancies were resolved. In an examination of a large sample of clusters, Allen (1998) suggests that the x-ray-lensing mass discrepancy can often be resolved by taking account of the effects of cooling flows and carefully ensuring that the lensing and x-ray masses are probing the same line of sight. His analysis of a sample of 13 clusters show consistency between x-ray and lensing masses for the 6 cooling flow clusters and an agreement for the non-cooling flow clusters when the comparison was made outside of the core of the cluster.

5.3.6 Radio Bright Point Sources

At the frequency range of this experiment, 26-36 GHz, radio point sources appear in about half of the observed clusters. The radio source counts from the SZ measurements are presented in Cooray *et al.* (1997). Also in this paper is a discussion of the systematic error in the SZ decrement resulting from not removing radio point sources just below the detection limit. The error was estimated for the cluster A2218, where a point source evident at low frequencies was not detected significantly at 28.5 GHz. The presence of this point source could lead to an underestimate of the decrement of about 0.5-1.5%, and an upper limit to the magnitude of the underestimate of ΔT, and therefore the gas mass, is set at $\sim 2\%$.

Loeb & Refregier (1997) also investigated the effects of point source removal on the SZ decrement. They predict a systematic overestimate of the decrement due to enhanced detectability and removal of point sources within the cluster relative to the field away from the cluster. The enhanced detectability is due to the lensing magnification of background point sources by the cluster potential. Scaling their derived result at 15 GHz with the spectral index for the cluster sources derived in Cooray *et al.* (1997), the Loeb-Refregier effect would predict a $<2\%$ overestimation of the gas mass.

Chapter 6

Abell 370: A Test Case

The gas mass and gas fraction calculations described in Section 5 are applied to a test case, Abell 370. AWe choose this cluster for two reasons. The first is that A370 is well-studied at optical and x-ray wavelengths, and so allows a detailed comparison of the SZ data with other observations. The second is that it is an extreme example of a cluster, being highly elliptical, and exhibiting complicated optical and x-ray structure. As such, it serves as a test of the gas fraction analysis method, which we plan to use on a large sample of clusters. Its low declination ensures that its u-v coverage is more limited than clusters at moderate declinations (see Figure 2.6). It is highly elliptical, with a projected axis ratio of 0.67. Furthermore, its x-ray image and gravitational lensing model evidence complicated structure in the cluster core.

In this chapter we first present a summary of the x-ray and optical observations of A370 in Section 6.1, then discuss the SZ observations in Section 6.2, derive the gas mass and gas fractions both in the cylindrical and spheroidal geometries in Section 6.3, and discuss the Hubble constant measurement from A370 and the systematic uncertainties in the f_g measurements in Sections 6.4 and 6.5, respectively.

6.1 Optical and X-ray Observations

The distribution and kinematics of Abell 370's constituent galaxies have been carefully measured optically. Mellier *et al.* (1988), using their 29 best galaxy spectra, find Abell 370 has a mean redshift z = 0.374 and velocity dispersion $\sigma_v = 1340^{+230}_{-150}$ km s^{-1}. These observations also show that the cluster is dominated by two giant elliptical galaxies, with a projected separation of about 40″ in the north-south direction. The major axes of both of these two dominant galaxies are also oriented nearly north–south. The Mellier *et al.* optical isopleth map shows two density peaks, with similar north-south orientation, although these are not centered on the two elliptical galaxies. The galaxy velocities do not appear to be distributed in a Gaussian manner, although the statistics derived from a sample of 29 galaxies are not definitive. Should the velocity distribution truly be non-Gaussian, it may suggest that the cluster is bimodal or that it is not yet fully relaxed. The mean velocities in the two isopleth peaks are not found to differ significantly, however, nor are the calculated barycenters of the two peaks, and so it is difficult to make a firm conclusion on the state of the cluster based on these data alone.

Abell 370 was the first cluster found to have an associated strongly gravitationally lensed arc ($z_{arc} = 0.725$; Soucail *et al.* 1988). In addition to this giant arc, which apparently consists of multiple images of a single source, three faint pairs of images were found, each pair presumed to be lensed images of a single galaxy (Kneib *et al.* 1993). A radial arc was also found to be associated with this cluster (Smail *et al.* 1996).

Gravitational lens models have been used to map the total mass distribution in the core region of Abell 370. Kneib *et al.* (1993) find the position and elongation of the giant arc and the positions of the multiple images are best reproduced by a bimodal distribution of the dark matter, with the two centers of mass nearly coincident with

the cluster's two large elliptical galaxies. A subsequently discovered radial arc and subsequently measured redshifts of the multiple images are compatible with this model (Smail *et al.* 1996).

Abell 370 has been observed with the High Resolution Imager (HRI) of the *ROSAT* x-ray satellite. In the *ROSAT* bandpass (0.1-2.4 keV), x-ray Bremsstrahlung emission from a plasma at the high gas temperatures typical of clusters depends only weakly on the gas temperature. In Figure 1, we show an HRI image of A370, the result of $\sim$ 30 kiloseconds of observation time. The bright source to the north, at $\alpha_{J2000} = 02^h\ 39^m\ 55^s$, $\delta_{J2000} = -01°\ 32'\ 33''$, is coincident with what appears in the Digital Sky Survey to be a nearby elliptical galaxy, and does not appear to be associated with A370. The image indicates that the gas also is elongated in the north-south direction, and the emission is strongly peaked at the position of the southern dominant elliptical galaxy, numbered 35 in Mellier *et al.* (1988), and is offset from the center of the large scale emission. The cluster gas distribution does not appear to be clearly bimodal at this resolution, but it is suggestive. It is difficult, however, to characterize the x-ray emission more quantitatively with data of this sensitivity.

Abell 370 has also been observed with the ASCA x-ray satellite. Using 37.5 kiloseconds of *ASCA* GIS/SIS observations, Mushotzky & Scharf (1997) determined the emission-weighted average temperature of the cluster to be $7.13^{+1.05}_{-0.83}$ keV. Analyzing the same data, Ota *et al.* (1998) find the emission-weighted temperature to be $6.6^{+1.1}_{-0.9}$ keV. These values are systematically lower than the value obtained in the first analysis of these data by Bautz *et al.* (1994), who obtain a value of 8.8 ± 0.8 keV. The discrepancy is presumably because the Mushotzky *et al.* and Ota *et al.* analyses used the values of the response matrices of the *ASCA* telescope and x-ray detectors which have been refined since the Bautz *et al.* analysis (Bautz, private communication). For our analysis, we adopt the Ota *et al.* value of $6.6^{+1.1}_{-0.9}$ keV, because this published analysis includes detailed discussion of the spectral fitting procedure.

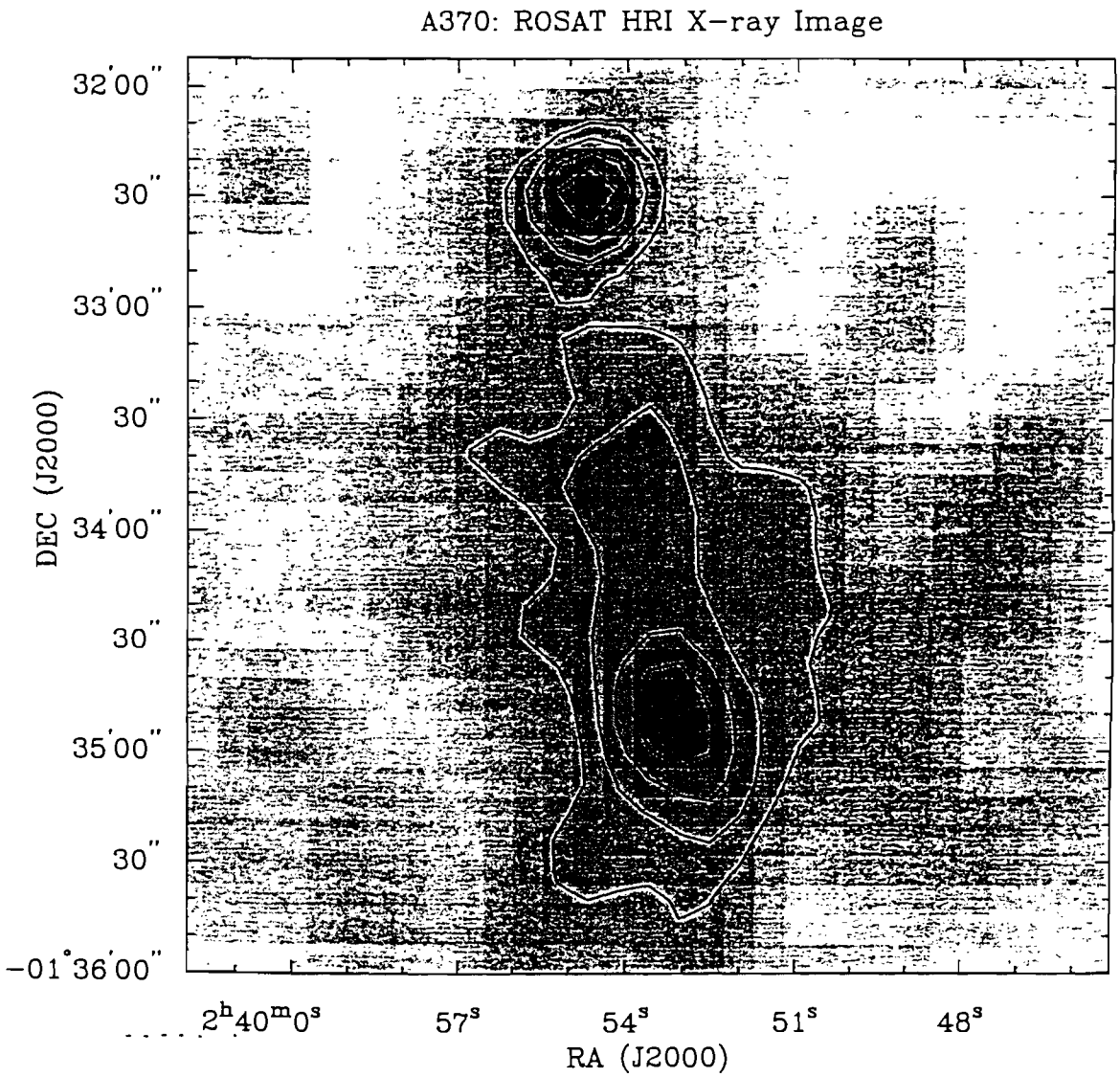

Figure 6.1 X-ray image of the galaxy cluster Abell 370 observed with the *ROSAT* HRI. The x-ray image was filtered to include only PHA channels 1-7, binned in 8″ x 8″ pixels, and smoothed with an 10″ Gaussian filter. The background level is 2.8 x 10^{-3} HRI counts sec^{-1} arcmin $^{-2}$ and the countour levels are at 5.8, 7.2, 8.7, 9.5, 10.1, and 11.6 x 10^{-3} HRI counts sec^{-1} arcmin $^{-2}$. The x-ray emission peak is associated with a pointlike source located $\sim$ 2.5′ to the north of the cluster center.

The unassociated source evident in the *ROSAT* HRI image has not been removed from the *ASCA* spectra in any of the three published analyses. If this emission originates in Bremsstrahlung emission from hot gas in the galaxy, its characteristic temperature is expected to be less than 1 or 2 keV (Sarazin & White 1988 and references therein). Since the sensitivity of *ASCA* is optimized for higher energies than this, we would not expect the measured temperature to be greatly contaminated. Should the emission originate from an AGN in the galaxy, though, the effect on the measured temperature is more difficult to predict, and will depend strongly on the index of the power law of the AGN spectrum. We assess whether the source is extended, and find that it is pointlike in the resolution of the HRI with a 2.4 σ certainty. Without further measurements, we cannot rule out that the cluster's spectrum is contaminated by emission from an AGN. It is also possible that if the cluster is in fact bimodal with two distinct subclusters, the measured emission-weighted average T_e will be somewhere between the temperatures of the two subclusters. Lacking more definitive measurements, we continue with our assumption that the gas is isothermal at $kT = 6.6^{+1.1}_{-0.9}$ keV, and describe the estimated effects of these uncertainties in Section 6.5.

We compare A370's measured line of sight velocity dispersion with our adopted gas temperature, and find $\beta_{spec} \equiv \mu m_p \sigma_v^2 / kT_e = 1.87^{+1.02}_{-0.59}$. If the energy per unit mass contained in the galaxies is equal to that in the gas and the cluster is spherical, we expect β_{spec} to be ~ 1. If the temperature measurement is biased low, *e.g.*, from an AGN, this could partially explain the β_{spec} discrepancy. Elongation of the cluster potential along the line of sight or a alignment of two (or more) subclusters will also enhance the measured β_{spec}.

The optical and x-ray observations still leave some ambiguity about the physical state of A370. The SZ measurements give additional information with which this may be clarified.

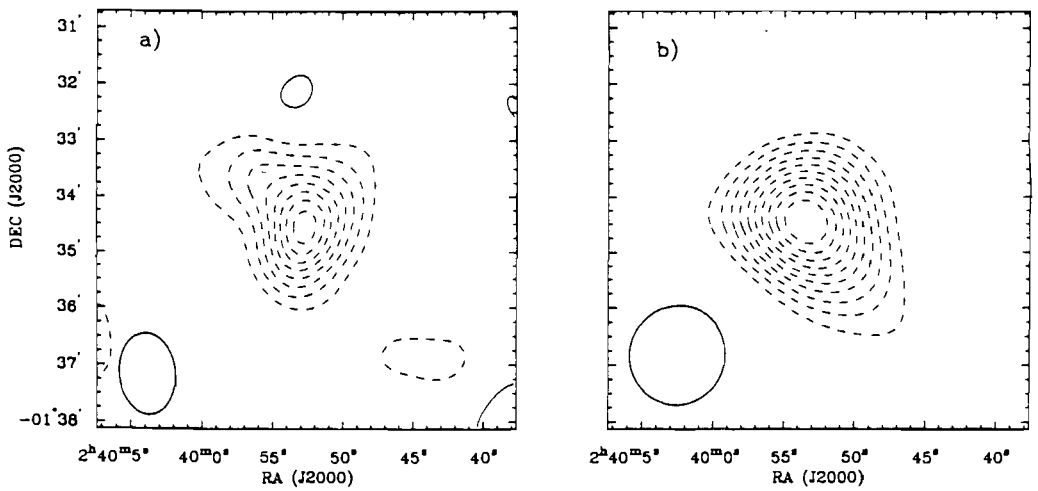

Figure 6.2 A. Image of Abell 370 from OVRO observations. The restoring beam, shown in the lower left hand corner, has a Gaussian FWHM of 59″ x 86″. The RMS noise in the map is 50 μJy/beam, or 14.9 μK, and the integrated flux density of the source is -1.54 mJy. B. Image of A370 from BIMA observations. The restoring beam has FWHM of 91″ x 95″. The RMS noise in the map is 180 μJy/beam, or 31.4 μK, and the integrated flux density of the source is -4.14 mJy.

6.2 SZ Observations

We observed Abell 370 for 50 hours over nine days with the Owens Valley Radio Observatory millimeter array in 1996 August and 43 hours over six days with the Berkeley-Illinois-Maryland Association millimeter array in 1997 June-August. We set our pointing center to $\alpha_{J2000} = 02^h\ 39^m\ 52.5^s$, δ_{J2000} =-01° 34′ 20″, the position of the northern dominant elliptical galaxy, the galaxy numbered 20 in Kneib *et al.* (1996).

We image the OVRO data using the DIFMAP package (Shepard, Pearson, & Taylor 1994). Examining the images made with projected baselines greater than 2.0 kλ, a point source at 45″ to the east of the map center (map center is the pointing center) is found in both continuum bands. Its measured flux density in the 28.5 GHz band, attenuated by the instrumental primary beam pattern, is +0.69 ± 0.10 mJy and is +0.84 ± 0.10 mJy in the 30 GHz band. This source, 0237-0147, is discussed

further in Cooray *et al.* (1998). We combine the two continuum channels, and find the best fitting model is a point source with flux density of 0.725 ± 0.07 mJy. The point source model is removed from the u-v data set in order to construct the SZ decrement map. A Gaussian taper with FWHM of 1.2 $k\lambda$ is applied to the combined dataset in the u-v plane and map was CLEANed, restricting the CLEAN components to the central 200″, about the size of the decrement in the convolved, or "dirty", map. The map presented in Figure 2A is made with a restoring beam of Gaussian FWHM 59″ x 86″, with contour intervals of 1.5 σ. The $r.m.s.$ noise in the map is 50 μJy/beam, or 14.9 μK, and the integrated flux density of the source is -1.54 mJy.

Again using DIFMAP, we image the BIMA data, and find the same point source at about 45″ to the east of the pointing center in a high resolution (projected baselines longer than 1.4 $k\lambda$) image. The point source measured at BIMA in 1997 has flux density of $+0.70 \pm 0.17$ mJy. The primary beam attenuation at the point source position in the BIMA system is $\sim$ 6% less than the attenuation at this position at OVRO, and so the flux density of the point source is consistent with being constant in time. We model and subtract the point source from the data set, apply a Gaussian taper with FWHM of 0.8 $k\lambda$ in the u-v plane and construct a map of the decrement. The map was CLEANed, restricting the CLEAN components to the central $\sim$ 220″ of the resultant image, about the size of the decrement in the dirty map. The restoring beam used to make the map in Figure 2B is a Gaussian with FWHM 91″ x 95″, and the contours presented are at intervals of 1.5 σ. The $r.m.s.$ noise in the map is 180 μJy/beam, or 31.4 μK, and the integrated flux density of the source is -4.34 mJy.

It is instructive to compare the general characteristics of SZ images to the x-ray map. At the resolution of both the OVRO and BIMA instruments, the gas is extended in the north-south direction, though less markedly than in the x-ray map. The substructure suggested by the lensing and velocity dispersion data is not evident here. We increased the image resolution of both datasets, but the gas still

does not show significant substructure or bimodality. The SZ decrement distribution is not peaked at the pointing center, but south of it, about halfway between the two dominant galaxies (this will be quantified in the next section). The detailed appearance of the SZ map, especially the shapes of the least significant contours, depends on the specific method of point source removal and the CLEANing of the data, and so it is not useful to compare the SZ and x-ray images at a high level of detail. As discussed below, the quantitative analysis of the SZ data is done using the u-v data directly.

6.3 Gas Mass Fraction

The fitting is done in the manner of Chapter 4; the model is fit to the data in the u-v plane. Figure 6.2 demonstrates the necessity of this. Although the OVRO image is deeper than the BIMA image, *i.e.*, the *r.m.s.* noise is lower, the BIMA image shows a broader spatial distribution of the decrement, because the BIMA primary beam is 1.5 times as large. Performing the model fitting in the u-v plane naturally takes these effects into account.

The parameters we fit are centroid position, β, θ_c, axis ratio (defined to be < 1), position angle (defined counterclockwise from north), and $\Delta T(0)$. The position and flux density of the radio-bright point source are also allowed to vary.

We performed a χ^2 analysis of the model by fitting the model to the combined BIMA and OVRO datasets. The model corresponding to each set of the seven fit parameters is multiplied by the primary beam response and Fourier transformed to compare directly with the interferometer data. The Fourier transform of the point source model is added to the cluster model without being multiplied by the primary beam. The fitting routine allows different point source fluxes for each dataset. This is sufficient, since the primary beam response affects only the point source flux, not its

position. Hence, the reported point source flux will be the point source flux modified by the primary beam response.

The inner u-v radius cutoff is determined by the shadowing limit; for BIMA data this limit is 0.58 $k\lambda$ and for OVRO data it is 1 $k\lambda$. We use the holographically determined primary beam models when modeling the data, and the entire datasets are used to do the analysis. The best fit parameter values for A370 are: θ_c= 78″, β= 1.37, $\Delta T(0)$ = -650 μK, and axis ratio = 0.67 with major axis exactly north-south. The best fit central position is 20″ to the south of the pointing center, at $\alpha_{J2000} = 02^h\ 39^m\ 53.2^s$, δ_{J2000} =-01° 34′ 40.4″, about halfway between the two giant elliptical galaxies.

Holding the centroid position, axis ratio, position angle, and point source position and flux fixed to the best fit values, a χ^2 statistic is derived for a large range of β and θ_c. Presented in Figure 6.3A. is a contour plot of these fits, where $\Delta T(0)$ is allowed to assume its best fit value at every pair of β and θ_c. The full line contours are marked for $\Delta\chi^2$ = 2.3, 4.61, and 6.17 which indicate 68.3%, 90.0%, and 95.4% confidence, respectively, for the two-parameter fit. The dashed lines indicate $\Delta\chi^2$ =1.0, 2.71, and 6.63. The projection onto the β or θ_c axis of the interval contained by these contours indicates the 68.3%, 90% and 99% confidence interval on the single parameter. Figure 6.3A. shows the contours derived when approximating the SZ distribution to be spherical, *i.e.*, the axis ratio is fixed to be 1.0. This illustrates that β and θ_c are correlated strongly and are not individually well constrained by these data. This poor constraint is at least partly due to the low declination of A370, which makes sampling non-redundant spatial frequencies difficult with the OVRO and BIMA instruments. Again, Abell 370 represents an extreme case; the β - θ_c constraints from the CL0016+16 data are stronger (see Figure 4.3.)

We also fit the data with a β-model which includes a truncation of the gas distribution at a given radius. With truncation radii from 270″ to 1000″, (β, θ_c, $\Delta T(0)$)

Figure 6.3 The OVRO and BIMA datasets are fit jointly with a β-model, with the centroid, axis ratio, major axis position angle and point source flux and position fixed at their best fit values, and $\Delta T(0)$ allowed to assume its best fit value at each (β, θ_c) point. A. The OVRO and BIMA datasets are fit jointly with an circular β-model, *i.e.*, the axis ratio is fixed to equal 1.0. B. The OVRO and BIMA datasets are fit jointly with a elliptical β-model. The centroid and point source flux and position are fixed at the best fit values, and $\Delta T(0)$ is allowed to assume its best fit value at each (β, θ_c) point. In both plots, the best fit (β, θ_c) point is indicated with an x. The full line contours are marked for $\Delta\chi^2 = 2.3$, 4.61, and 6.17 which indicate 68.3%, 90.0%, and 95.4% confidence, respectively, for the two-parameter fit. The dashed lines indicate $\Delta\chi^2 = 1.0$, 2.71, and 6.63; the projection onto the β or θ_c axis of the interval contained by these contours indicate the 68.3%, 90% and 99% confidence interval on the single parameter.

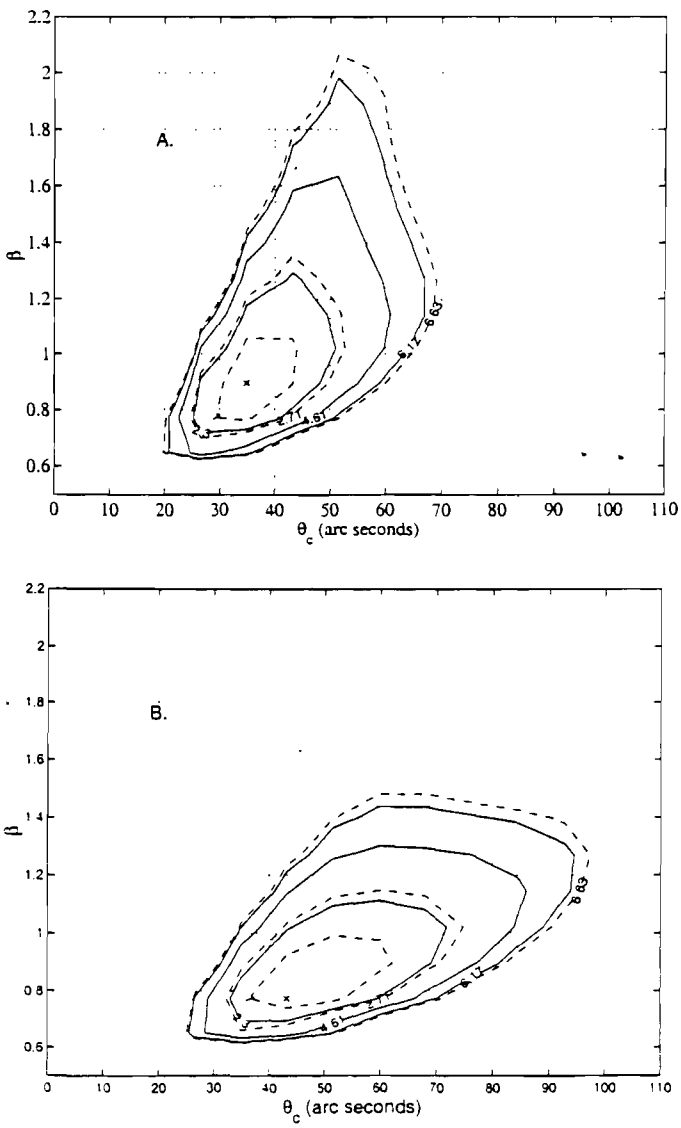

change from (1.37, 77″, -650μK) to (1.26, 73″, -667μK). The χ^2 statistic changes only minimally for different cutoff radii, with $\Delta\chi^2$ less than 0.1. This indicates that the possible systematic uncertainty in the fitted parameters due to modeling the data without a cutoff is not significant, and we proceed modeling without a cutoff radius.

Since the optical and x-ray data suggest that Abell 370 may have a bimodal gravitational potential, we also fit the data with a pair of β-models, each allowed independent shape parameters and position. The best fit two-component model has one component with nearly twice the decrement, $\Delta T(0) = -782\mu K$, as the other, with $\Delta T(0) = -430\mu K$. The stronger component is centered at $\sim 40''$ south of the pointing center, at the position of the large southern elliptical galaxy. The best fit position of the second component is $\sim 25''$ north of the pointing center, *i.e.*, 25″ north of the large northern elliptical, though this position is only weakly constrained. Both have a core radius of about 30″ and β of 1.0, and are nearly circular. This pair of model reduces the χ^2 statistic by 5 when 7 new parameters are introduced, and therefore is not a significantly better fit to the data.

We calculate the surface gas mass via the method outlined in Section 5.1.1 and compare it to the total mass implied by the lensing models for this cluster. The lensed arc in Abell 370 has a radius of curvature of about 30″ centered nearly halfway between the dominant galaxies, at about the same position of the gas density centroid in the one component β model. Since the SZ-derived isodensity contours are elliptical, we calculate the gas mass in a cylinder with an elliptical cross section with axis ratio of 0.67 and major radius 40″ since the lens model should be most accurate near the lensed arc radius. We explore the parameter space $0.4 < \beta < 4.0, 10'' < r_c < 240'', -2000\mu K < \Delta T(0) < -200\mu K$. For each set of β, θ_c, and $\Delta T(0)$, we determine a cylindrical gas mass. Each set of parameters also has an associated χ^2 value.

Although θ_c and β have a large range of values within 68% confidence, as was evident in Figure 6.3, the gas mass, which depends on all three parameters, is relatively

well constrained. In Figure 6.3, we show the derived cylindrical mass at radius 65″ as it varies with β and θ_c. The temperature decrement is allowed to assume its best fit value at each point. The isomass surfaces, shown in greyscale, follow the shape of the confidence interval contours, indicating that sets of parameters which fit the data well will predict the same gas mass. This is to be expected, since under the isothermal assumption, the SZ flux is directly proportional to the gas mass, and the fit parameters must reproduce the same observed flux at the angular scales where the flux is best measured. We build up a gas mass distribution as a function of confidence. The SZ-derived cylindrical gas mass, at 68% confidence, is $5.4^{+1.17}_{-1.24} \times 10^{12} h^{-2} M_{\odot}$. Included in the error estimates are the uncertainty due to the fit parameters, the 4% SZ absolute calibration uncertainty, and the gas temperature measurement uncertainty.

We also derive the gas mass in the model with two components. The best fitting two-component β-model parameters are integrated in this same volume. This yields a gas mass of $3.48 \times 10^{12} h^{-2}\ M_{\odot}$, 35% lower than the single model, though at larger radii the difference in gas mass between the two models decreases. Since the bimodal model doubles the parameter space over which fits must be made, making a comprehensive parameter fit unfeasable, we approximate the statistical uncertainty from the fit to be the same as in the single model fit, about 20%.

These gas masses are compared to the total mass implied by strong lensing measurements. We calculate the gravitational mass using the lensing model in Kneib *et al.* (1993) in the same volume in which the surface gas mass was calculated, a cylinder with an elliptical profile with axis ratio 0.67 and 40″ major axis, centered at the SZ model fit center. The quoted uncertainties on the model parameters are less than ten percent, but we make a conservative estimate of 20% for the uncertainty, to allow for variations of this model. Comparing this mass, $1.59^{+0.30}_{-0.30} \times 10^{14} h^{-1}\ M_{\odot}$, to the single-component gas mass yields a gas fraction, f_g, of $(0.034^{+0.010}_{-0.010}) h^{-1}$. The two-component model yields a gas fraction of $(0.022 \pm 0.006) h^{-1}$. To calculate the

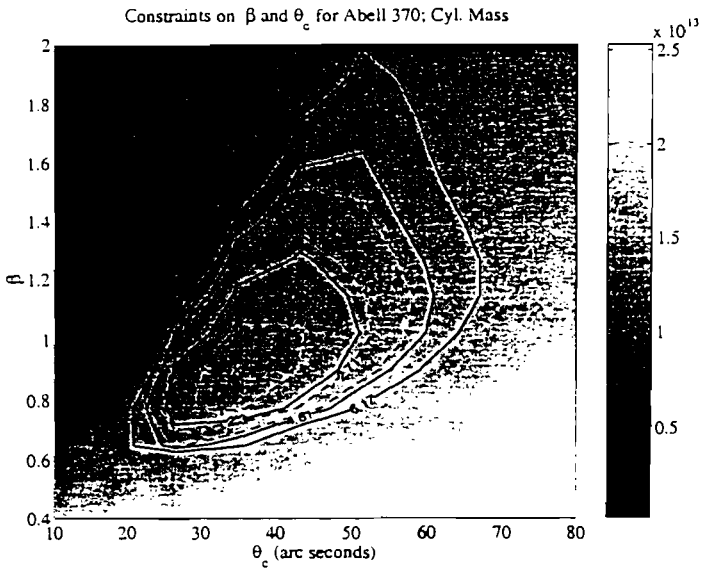

Figure 6.4 Gas Mass for Abell 370. The gas mass in a cylindrical volume with cross section of 65″ and axis ratio 0.672, in units of $M_{\odot}$is shown in greyscale. The two-parameter confidence intervals for β and θ_c are overlaid. At each point, $\Delta T(0)$ is allowed to take its best fit value. The best fit point is marked with an x.

cluster's angular diameter distance, we assume $\Omega_M = 0.3$ and $\Omega_\Lambda = 0$. If $\Omega_M = 1.0$, $\Omega_\Lambda = 0$, the angular diameter distance to A370 will be 6.5% smaller, as will the gas fraction.

We also derive the spheroidal gas mass and gas mass fraction as described in Sections 5.1.2 and 5.2.2. The gas fraction is calculated for three cluster geometries, an oblate ellipsoid with its symmetry axis in the plane of the sky, a prolate ellipsoid with its symmetry axis in the plane of the sky, and a sphere.

For the same range of β, θ_c, and $\Delta T(0)$ used in the cylindrical geometry analysis, we calculate the cluster's ellipsoidal gas mass, virial mass, gas mass fraction, and χ^2 for each geometry. We calculate the 68% confidence intervals for the gas mass and the gas mass fraction at different major axis radii for the ellipsoid. These measurements are made at a major axis radius of 65″ ($\sim 200h^{-1}kpc$). We also calculate the gas fraction for the two components of the bimodal model separately, using a gas temperature of

6.6 keV for each and find that the gas fraction for both components is $\sim 3.5\%$. The calculated values are found in Table 6.3.

The gas in nearby clusters has been observed to be distributed more uniformly than the dark matter (*e.g.*, David *et al.* 1995), which is to be expected if energy transfer from galaxies and the dark matter to the gas is important. If this is generally true, the value of the gas mass fraction measured will then depend on the radius within which the measurement is made. To compare the gas fractions measured within a fixed angular radius for clusters with differing size and redshift, we attempt to extrapolate our measured gas fractions to a fiducial radius. As suggested in Evrard (1997) and Metzler, Evrard, & Navarro (1998), we choose this radius to be that at which the average density of the cluster interior to this radius is 500 times the critical density, $\rho_c = \frac{3H_o^2}{8\pi G}$. Their numerical simulations suggest that within this radius, r_{500}, the cluster's baryon fraction should closely reflect the universal baryon fraction, if the current physical models of hierarchical structure formation are correct. We use an analytical expression describing the expected variation of the gas fraction with overdensity which was derived from hydrodynamic simulations of clusters (Evrard 1997), an expression which is found to be consistent with the radial gas fraction variation reported in the David *et al.* (1995) sample.

$$f_{gas}(r_{500}(T_e)) = f_{gas}(r_X)\left(\frac{r_{500}(T_e)}{r_X}\right)^{\eta}, \tag{6.1}$$

where $\eta = 0.17$, $f_{gas}(r_{500}(T_e))$ is the gas fraction at r_{500}, and r_X is the radius at which the gas fraction is measured. We modify Evrard's expression for r_{500}, derived for low redshift clusters, to include the change in the value of ρ_c with redshift; $\rho_c(z) = \rho_c(z = 0)(1+z)^3$ in a matter dominated universe.

$$r_{500}(T_e) = (1.24 \pm 0.09)\left(\frac{T_e}{10\ \mathrm{keV}(1+z)^3}\right)^{1/2} h^{-1}\ \mathrm{Mpc}. \tag{6.2}$$

In contrast to the spheroidal geometry gas fractions, the surface gas fraction is not measured at a clearly defined overdensity. In order to estimate the correction

Table 6.3: Gas Mass Fractions for Abell 370

geometry	$f_g h$	$\frac{f_g(\delta_{500})}{f_g(65'')}$	$f_g(\delta_{500})h$
cylinder (radius=40″)	$(0.034^{+0.010}_{-0.010})h^{-1}$	1.31	$(0.045^{+0.013}_{-0.013})h^{-1}$
cylinder (radius=40″), bimodal	$(0.022^{+0.006}_{-0.006})h^{-1}$	1.31	$(0.029^{+0.008}_{-0.008})h^{-1}$
oblate ellipsoid (radius=65″)	$(0.064^{+0.024}_{-0.024})h^{-1}$	1.31	$(0.084^{+0.032}_{-0.031})h^{-1}$
prolate ellipsoid (radius=65″)	$(0.096^{+0.036}_{-0.034})h^{-1}$	1.31	$(0.126^{+0.047}_{-0.045})h^{-1}$
sphere (radius=65″)	$(0.085^{+0.043}_{-0.032})h^{-1}$	1.31	$(0.112^{+0.064}_{-0.056})h^{-1}$

needed to estimate the gas fraction at r_{500}, we note that the bulk of the SZ signal comes from the core region of the cluster, and estimate the correction to be of the same magnitude as we use for the spheroidal models.

The gas fraction values at r_{500}, extrapolated from those measured at 65″ are summarized in Table 6.3, where the uncertainties include the statistical fit uncertainties and the gas temperature uncertainties. The gas masses, gas mass fractions and gas fractions extrapolated to r_{500} are given. The gas fraction in the cylindrical geometry has its long axis along the line of sight, axis ratio of 0.672, major radius measured from the center of the fitted SZ model, and its total mass estimated from the gravitational lensing model. The oblate, prolate, and spherical ellipsoids have the major axis indicated in the first column, and their symmetry axis in the plane of the sky. The total masses are estimated from the isothermal HSE approximation.

This experiment best measures the gas fraction at a given angular scale, which corresponds, in Abell 370, to an overdensity of 6000-8000 ρ_c. This is not the optimal radius at which to compare observations with numerical simulations, since the simulation resolution is limited in the cores of the clusters, and the gas in the core may also be sensitive to additional physics, magnetic fields for example, not yet included in the models. For these reasons, the extrapolations should be taken with some caution.

6.4 Hubble Constant

Constraints on the Hubble parameter $H_\circ$ can be derived from the SZ and x-ray measurements of A370. This is useful not only as a distance ladder-independent measurement of $H_\circ$, but, when compared with other $H_\circ$ measurements, can be used to explore possible systematic errors made in the gas fraction calculation. We follow the method outlined by Hughes and Birkinshaw (1998), again assuming that the gas is isothermal and that the gas density can be described by an ellipsoidal β-model. We first describe the analysis methods and results, and then discuss the limitations of the present analysis and the possibility for improving the measurement.

It is possible to constrain $H_\circ$ from spatially resolved measurements of a cluster's SZ effect and x-ray emission, along with a measurement of the gas temperature (see Birkinshaw 1998 and references therein). We measure the x-ray surface brightness in the *ROSAT* HRI image (Figure 6.1). We filter the data to include only PHA channels 1-7 in order to reduce the background level (David *et al.* 1997) and block it into $8'' \times 8''$ pixels. A circular region with a radius of $36''$ centered on the pointlike x-ray source to the north of the cluster was excluded from our modeling; the position of this source is $\alpha_{J2000} = 2^h\ 39^m\ 54.6^s$, $\delta_{J2000} = -1^\circ\ 32'\ 28''$. Model fitting of these data were made using the software described by Hughes and Birkinshaw (1998). The spectral emissivity, Λ_{eo}, was calculated according to their equation (1). The x-ray data was fit to all of the gridded (β, θ_c) pairs within the SZ data 90% confidence interval (Figure 6.3). At each grid point within this interval, we performed a joint fit of the HRI data to obtain the central x-ray surface brightness. The quality of the x-ray data, however, was not adequate to provide a sufficient constraint on the shape parameters. We derived an $H_\circ$ estimate from the fitted SZ and x-ray parameters for an isothermal cluster, and find that $H_\circ$ is not strongly constrained. When the considerable uncertainties from the emission-weighted temperature are also considered, as

well as the uncertainties due to cluster geometry and inclination angle, it is clear that the $H_\circ$ calculation will not aid the gas fraction measurements. A Hubble constant determination from A370 will be difficult until higher quality x-ray data, *i.e.*, from the planned AXAF A370 observation, are available.

6.5 Magnitude of Systematic Effects

The assumptions made in the hydrostatic isothermal analysis can be tested by comparing the HSE predicted virial mass to the lensing mass. We make this comparison and also attempt to estimate the magnitude of some of the systematic effects discussed in Section 5.3.

To compare the HSE mass with the lensing mass, we integrate the mass density in Equation 5.8 in the same cylindrical volume for which the lensing mass is calculated. This cylindrical total mass is calculated for each set of shape parameters and the 68% confidence limits are derived. This comparison is potentially a means to discriminate between oblate and prolate models for the cluster, but, as discussed in Section 5.2.2, the concentrically ellipsoidal geometry approximation breaks down at large radii, so this quantity is not calculated for the ellipsoidal geometries.

Using an electron temperature of $6.6^{+1.1}_{-0.9}$ keV, the spherical cluster total mass integrated in the cylindrical volume is $1.17^{+0.37}_{-0.22} \times 10^{14} M_\odot$, consistent with the lensing mass in the same geometry of $1.59^{+0.30}_{-0.30} \times 10^{14} h^{-1} M_\odot$. The two-component β-model predicts about $1.14 \times 10^{14} M_\odot$, and so it also remains a viable model for the cluster's mass distribution.

This test is most useful in failure, though. Agreement between the HSE mass of the cluster and the lensing mass does not guarantee that the assumptions in the HSE analysis are valid. For this reason, we examine other possible systematic effects and their effects on the mass measurements.

Emission-weighted Temperature If the x-ray point source to the north of the cluster is indeed a nearby AGN, the emission-weighted temperature could be in error. For instance, in the Hughes & Birkinshaw (1998) analysis of CL0016+16, a nearby AGN is present in the field, too close for the ASCA GIS to resolve it and determine a separate temperature measurement. Jointly fitting *ROSAT* PSPC and *ASCA* GIS data, Hughes & Birkinshaw determine the ICM temperature of the cluster to be $7.55^{+0.72}_{-0.58}$keV, and measure a power law index for the AGN x-ray emission of 2.54±0.18. Should they not have included a separate model for the AGN emission, the derived ICM temperature would have been ∼2 keV lower (Hughes, private comm.). Since AGN generally have power law spectra, though, AGN contamination will generally, though not always, tend to artificially bias the temperature low. This problem has not been addressed extensively in the literature, however.

Should the measured ICM temperature be biased low by 2 keV, or ∼ 30%, the gas fraction would be biased high by ∼ 100%. It is unlikely that the temperature is this much in error, since the HSE total mass using the emission-weighted temperature is in good agreement with the strong lensing mass.

Non-Isothermal ICM We estimate the effect of a negative temperature gradient on the gas fraction calculations for typical cluster parameters. There is no evidence for a cooling flow in Abell 370, so we do not consider its effects here. Recent observations of $z << 0.1$ clusters suggest that clusters have a slow decline in temperature with radius, dropping to about half the central value at 6-10 core radii (Markevitch *et al.* 1996). This is adequately described by a gas with a polytropic index of $\gamma = 1.2$. (For discussion of polytropic indices, see Sarazin 1988 and the references within.) For the best fit Abell 370 shape parameters, β= 1.37, θ_c= 78″, and $\gamma = 1.2$, the isothermal gas mass is an overestimate by ∼ 5% at 20″ radius, is equal to the polytropic mass at 60″ and is an underestimate of ∼10% at 90″ radius. The isothermal virial mass is an underestimate by ∼ 40% at 20″ radius, is a 20% underestimate at 65″ and is

about equal to the polytropic mass at 100″ radius. The gas mass fraction is then overestimated by $\sim$ 35% at 20″, is about 15% overestimated at 65″, and equal at about 85″. Changing the shape parameter values change these estimates 5-10%, but should the value of γ be larger, the error in using an isothermal analysis can be quite significant.

The planned Advanced X-ray Astrophysics Facility (AXAF) mission will make possible the measurement of temperature structure in clusters, should it exist. A Guaranteed Time Observation of 90 kiloseconds is scheduled toward Abell 370, which will should be sufficient to indicate the presence of a temperature gradient in this cluster.

Inclination Angle As discussed in Section 5.3.3, the implied SZ gas mass for a cluster will remain constant even if the the cluster is elliptical with its symmetry axis inclined away from the plane of the sky, but its implied HSE mass will change. Here, the gas fraction of Abell 370 is calculated as a function of inclination angle, i, using the best-fit shape parameters $\beta = 1.37$, θ_c =78″, and presented in Figure 6.5. The change in gas fraction is not severe over a large part of the parameter space for this cluster. Inclination angle is not likely a strong source of systematic error.

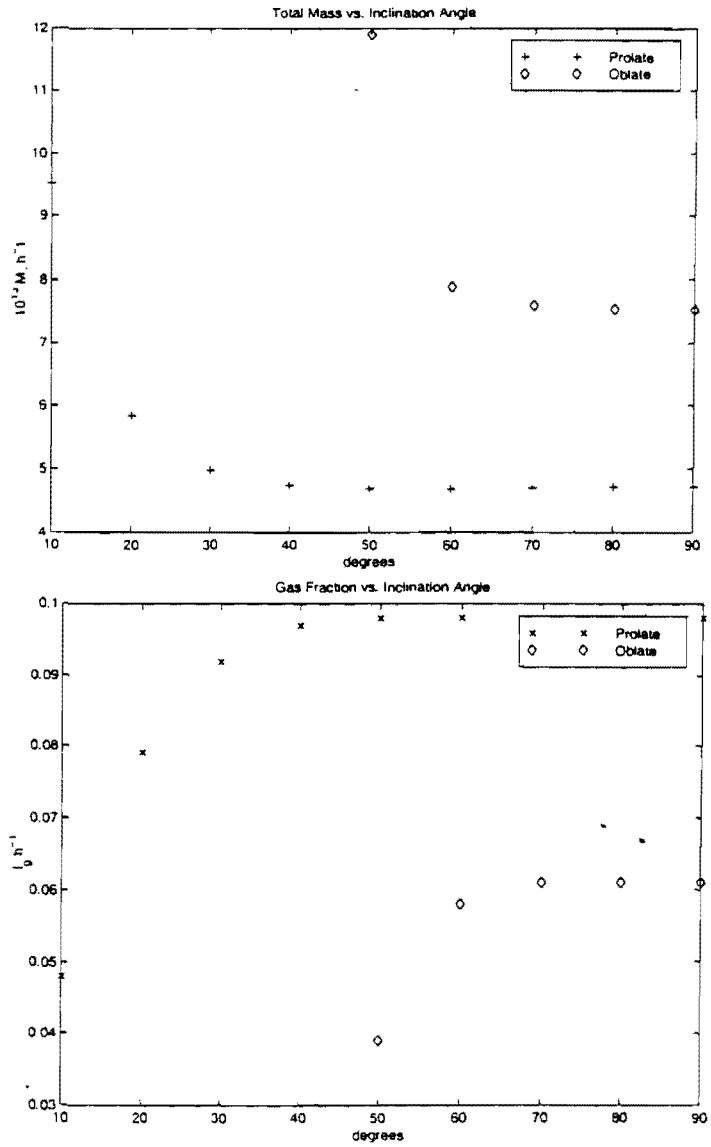

Figure 6.5 Change with inclination angle of derived HSE mass and gas fraction for Abell 370. Top panel: The total mass, calculated with the HSE method, as a function of inclination angle. The mass is calculated using the best fit SZ parameters. Bottom panel: The gas mass fraction as a function of inclination angle, where the total mass is calculated with the HSE method. The angle i is measured between the symmetry axis and the line of sight.

Chapter 7

Cluster Sample

A large sample of clusters, numbering over 40, was observed with the centimeter-wave SZ system during the 1994-1998 observing seasons. Not all of the clusters were pursued beyond the initial measurements. Some of the observations were intended as a survey for point sources and to help define a larger sample for future work. Some clusters were observed at length but were not detected. To date, 25 clusters have been detected significantly; analysis of a sample of 18, which includes a homogeneous subsample, are presented here.

The purpose of this chapter is fourfold: to describe the sample selection method, to discuss possible selection effects, to enumerate the known properties from optical and x-ray observations of the selected clusters, and to describe the homogeneous subsample and its properties.

7.1 Cluster Selection and Rejection

7.1.1 Criteria

Clusters of galaxies were first identified as enhancements of the surface density of galaxies. Since the background is also galaxy-rich and is variable, false cluster identifications from superpositions can occur (Frenk *et al.* 1990), and clusters may be

missed due to a local smaller-than-average background. Identifying clusters based on x-ray emission ameliorates the superposition problem because, as x-ray luminosity is proportional to $\int n_e^2 dV$, the chance superposition of two poor clusters will not mimic the presence of a rich cluster. X-ray surface brightness from clusters is generally two orders of magnitude larger than the x-ray background, and the temperature of the x-ray gas is not sensitive to projection effects. For these reasons, x-ray surveys are expected to be a very good method for identifying clusters. From these, massive clusters may be identified by a velocity dispersion criterion, rather than x-ray luminosity. Our purpose, however, is to identify massive clusters which manifest the Sunyaev-Zel'dovich effect, and the SZ effect requires the presence of an ICM, which is not necessarily indicated by the presence of a galaxy association.

The observed quantity from x-ray telescopes is surface brightness. The x-ray surface brightness, $b_X(E)$, where E is the photon energy, due to thermal bremsstrahlung, is sensitively dependent on the density of the ICM and to a lesser degree to its temperature. Specifically, $b_X(E,r,\phi) = \frac{1}{4\pi(1+z)^3}\int n_e(r,\phi,l)^2 \Lambda(E,T_e(r,\phi,l))dl$, where (r,ϕ,l) are cylindrical coordinates, with l along the line of sight, z is the redshift of the cluster, $n_e(r)$ is the spatially varying electron density, and Λ is the spectral emissivity of the gas at the x-ray energy E and electron temperature, T_e.

A sample of clusters selected on the basis of surface brightness will, however, be biased towards clusters which are extended along the line of sight, have central cooling flows with characteristic temperatures in the telescope's bandpass, or are dynamically active. A better selection criterion is x-ray luminosity, which will not be enhanced by such projections. Generally cooling flows only contribute 10-30% of a cluster's luminosity, although they have been observed to contribute as much as 70% (Peres *et al.* 1998).

We have selected clusters preferentially with high luminosities. The clusters were culled from public data from the *Einstein* mission and from the *ROSAT* mission. The

primary sources for *ROSAT* cluster targets were Ebeling *et al.* (1996) and Ebeling *et al.* (1998). The latter selected clusters from the *ROSAT* All-Sky Survey on the basis of cluster brightness, up to a limiting redshift of z=0.3. The *Einstein* Medium Sensitivity Survey (EMSS), which will be discussed in Section 7.2, also was a source of cluster targets (Gioia *et al.* 1990). Nichol *et al.* (1997) also studied the EMSS sample, and their resultant cluster sample contains refined redshifts and cluster identifications.

The observing scheme for this experiment requires that clusters be at declination greater than about -10°, that they be at redshifts greater than about 0.15, and that any radio bright point sources be ~5 mJy or less. The clusters initially observed and found to have radio bright point sources were not pursued further.

7.1.2 Selection Effects

We aim to select clusters which are massive. David *et al.* (1995) and Mohr *et al.* (1998) have found in x-ray studies of the gas fraction over a large range in mass that the gas fraction near the virial radius increases with cluster mass; poor groups have a lower gas fraction than massive clusters, presumably because the gas in poor clusters is more loosely bound to the potential and therefore more susceptible to energy input from galaxy winds and dark matter. The gas fraction in massive clusters should approach the universal value. The clusters in this sample all qualify as massive clusters, *i.e.*, have $T_e > 5$ keV, and so the gas fraction is not expected to be depressed relative to the asymptotic value for clusters.

In order to select for massive clusters (and also clusters which will be SZ-bright), the cluster sample is selected for high x-ray luminosity. A homogeneous, luminosity selected sample is preferable to selecting by high surface brightness, since surface brightness will preferentially select for clusters extended along the line of sight. A luminosity-selected sample may exhibit other selection effects, however. As mentioned in the previous section, x-ray luminous clusters may have large cooling flows or be

dynamically active, rather than simply massive. The presence of a cooling flow is unlikely to significantly affect the SZ gas measurement if the cooling flow is pressure supported, although it may affect an x-ray gas measurement. In fact, since cooling times are long, the presence of a cooling flow may indicate that the cluster has not experienced a recent disruptive merger, and so may be relaxed. Peres *et al.* (1998) find cooling flows of some magnitude in 70-90% of nearby clusters observed.

It is conceivable that clusters selected by luminosity may preferentially have a baryon enhancement at the cluster center. White *et al.* (1993) use numerical simulations to estimate the maximum baryon enhancement which can be produced by dissipative effects during cluster formation. Even for extreme models, they find it unlikely that the baryons could be enhanced by as much as 40%.

It is also possible that selecting against clusters with strong point sources may introduce a bias. This bias would also be redshift dependent because, while the SZ effect magnitude is not diminished by distance, the flux of a point source is, and so distant clusters will be less likely to be dropped because of point source confusion. Possible correlations between radio emission in clusters and cluster properties have been studied in the literature. Peres *et al.* (1998) study a sample of 55 nearby x-ray clusters, 40% with a cooling flow mass deposit rate of over 100 $M_{\odot}$/yr. They cross correlate this sample with radio surveys at several frequencies. However, they find no correlation between the radio power of the brightest cluster galaxy and the strength of the cooling flow. Roettiger, Loken, and Burns (1997) created simulations to study the hydrodynamics of the cluster gas during cluster mergers, and found that a major cluster merger could sustain the lifetime of radio halos beyond the canonical lifetime of the synchotron source. Currently, evidence for a bias introduced by radio emission criteria is limited.

7.1.3 Selected Clusters

Some of the clusters in the SZ sample have been well studied, both in x-ray and optical bands. Others have not been studied extensively. A short description of the observations of each cluster is included, should published literature be available. The prospects for future x-ray observations are also included for many clusters. Following these descriptions is Table 7.1.3, which denotes the redshifts, temperatures and luminosities for the cluster sample.

Images of twelve of the observed clusters are presented in Figure 7.1.3. These CLEANed images are from both BIMA and OVRO data and are restored with the beam appearing the bottom left-hand corner. The images are contoured at with multiples of 1.5 σ, where σ is the $r.m.s.$ noise of the observation.

Abell 2218 is a regular, circular cluster with several associated point sources. Spectacular strong gravitational lensing is associated with the cluster. Initial comparisons of the lensing mass with that derived by x-ray HSE method suggested a discrepancy, *i.e.*, the lensing mass was 2-3 times larger than the hydrostatic mass (Loeb & Mao 1994.) Further investigations of the cluster with weak lensing (Squires *et al.* 1996), show that the total masses derived by weak lensing and by the x-ray HSE method are consistent. With the weak lensing technique, a lower bound for the total mass in A2218 within $0.4h^{-1}$ Mpc is $(3.9 \pm 0.7) \times 10^{14}\ M_{\odot}$. The gas to mass ratio at $400h^{-1}$ kpc is found to be $(0.04 \pm 0.02)h^{-3/2}$(Squires *et al.* 1996). An AXAF A01 observation is scheduled for A2218.

Abell 1914 An AXAF A01 observation is scheduled for A1914.

Abell 665 *ROSAT* PSPC and HRI observations and *ASCA* observations have been made, and are publicly available. An AXAF A01 observation is scheduled for A665.

Abell 1689 is a well-studied cluster in both the optical and x-ray regimes. This cluster exhibits strongly lensed arcs and is highly substructured in its weak lensing

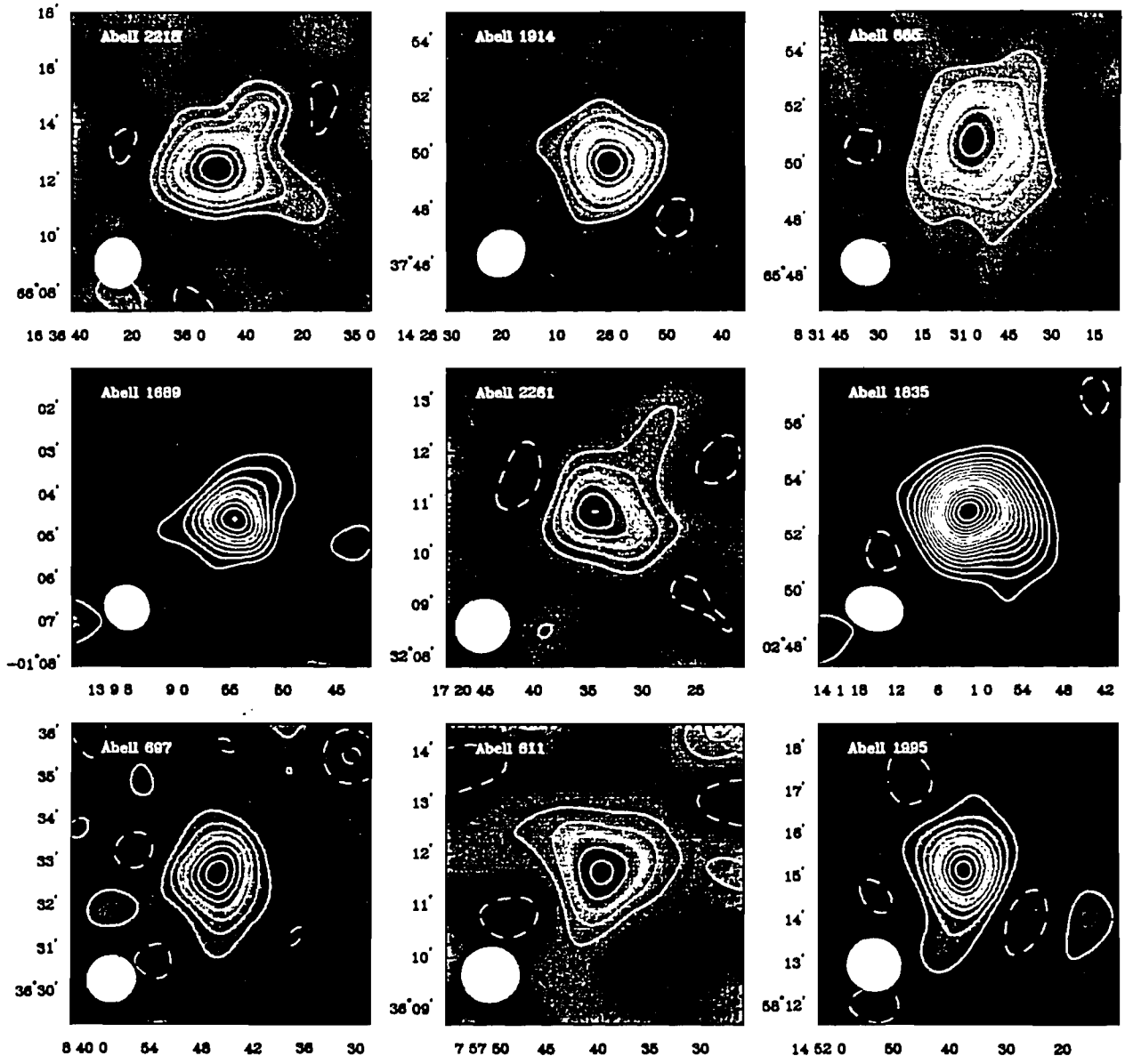

Figure 7.1 Images of the observed clusters. The CLEANed images are resored with the beams shown in the bottom left corners.

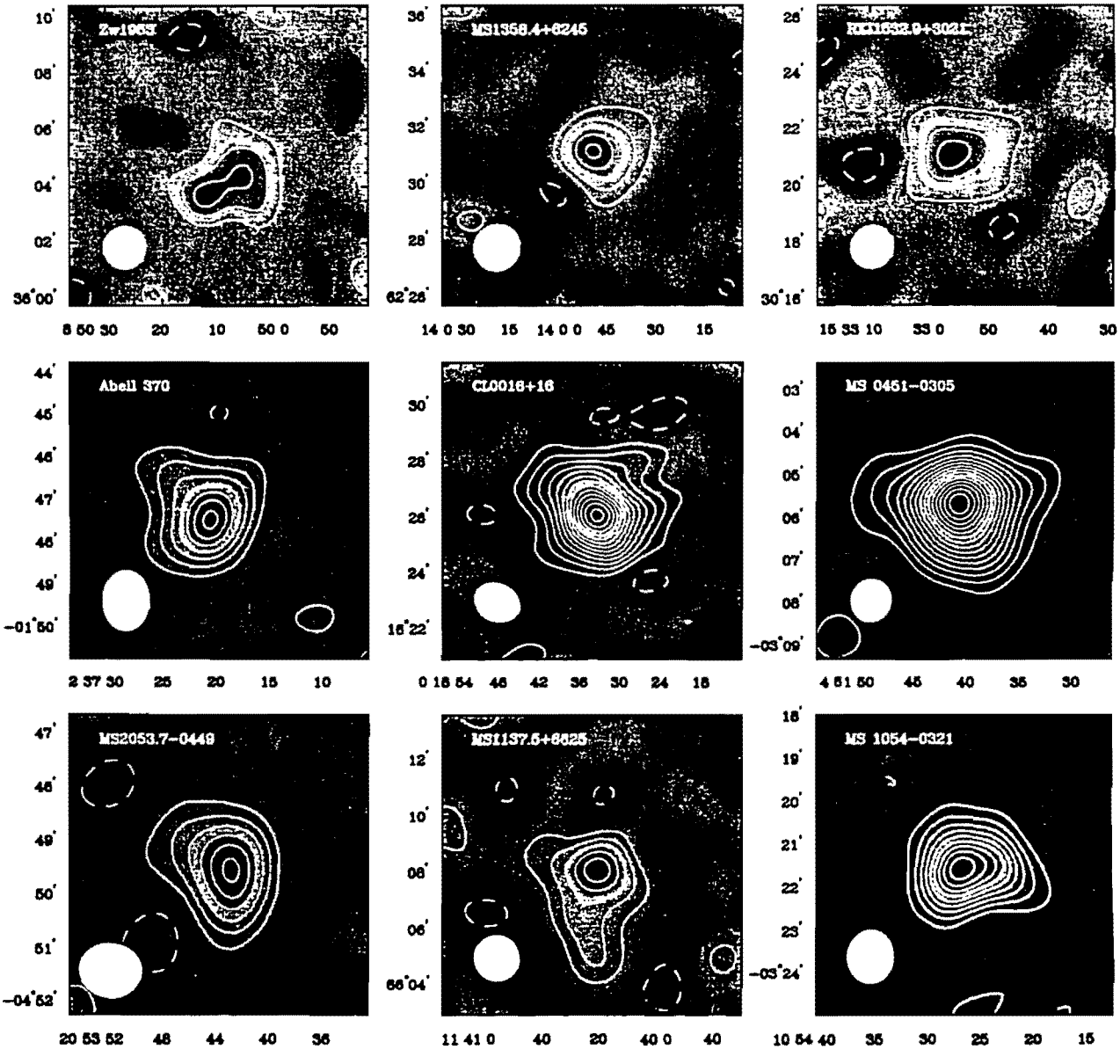
Zw1953
MS1358.4+6245
Abell 370
CL0016+16
MS 0451−0305
MS2053.7−0449
MS1137.5+6625
MS 1054−0321

map (Tyson & Fischer 1995.) This, and the bimodal distribution of A1689's constituent galaxies, suggests that this cluster may be quite elongated along the line of sight. It has a small cooling flow (White *et al.* 1997.) *ROSAT* PSPC and HRI observations and *ASCA* observations have been made, and are publicly available. An AXAF A01 observation is scheduled for A1689.

Abell 2261 was observed with the *ROSAT* mission and with the *ASCA* mission. The analysis of the *ASCA* data is in preparation. An AXAF A01 observation is scheduled for A1835.

Abell 1835 An AXAF A01 observation is scheduled for A2261.

Abell 697 was observed with the *ROSAT* mission and with the *ASCA* mission. The analysis of the *ASCA* data is in preparation. An AXAF A01 observation is scheduled for A697.

Abell 611 was observed with the *ROSAT* mission and with the *ASCA* mission. The analysis of the *ASCA* data is in preparation.

Abell 1995 was observed by the *ROSAT* mission and by the *ASCA* mission. An AXAF A01 observation is scheduled for A1995.

Zw1953 was observed in the EMSS. It has not been observed with the *ROSAT* mission nor with the *ASCA* mission.

MS1358.4+6245 was observed by the *Einstein* mission and by the *ASCA* mission. An AXAF A01 observation is scheduled for MS1358.4+6245.

R1532.9+3031 has been observed with the *ROSAT* HRI instrument, and the data are publicly available. *ASCA* observations for this cluster are scheduled for 1998.

Abell 370 is discussed at length in Chapter 6.

CL0016+16 is one of the best-studied clusters at high redshift. It has been observed with the *ROSAT* HRI and PSPC instruments as well as the *ASCA* mission. It is x-ray bright and is likely to be part of a large scale overdensity (Koo 1981).

Evidence has been found for at least two nearby poorer clusters (see Hughes *et al.* 1995, Connolly *et al.* 1996). It has the highest gas fraction of any cluster in this sample. Neumann & Bohringer (1997) investigate the gas fraction using *ROSAT* HRI and PSPC imaging and the HSE method for determining the total cluster mass. They find a gas fraction of $(14-23)\%h^{-3/2}(h=0.5, q_o=0.5)$ at 3 Mpc. To compare with our values, we scale by $(0.5)^{-3/2} \times 1.09 = 0.385$. The correct result, then, with which to compare the SZ gas fraction is $(5.39-12.32)h^{-3/2}$.

MS0451.5+0250 is a well-studied, x-ray luminous cluster. It was observed with *ROSAT* HRI and PSPC. This cluster is part of the CNOC cluster survey (Carlberg *et al.* 1995, Yee *et al.* 1996), and so its redshift is well-established and its galaxy dynamics have been investigated at length.

MS2053.7-0449 has not been studied very extensively in the x-ray regime. It has a rather short *ROSAT* exposure, and has not been observed with the *ASCA* instrument. In Gioia & Luppino's brightest EMSS cluster lens survey, this cluster was found to have a strongly lensed arc associated. Note that we have estimated this cluster's temperature from the luminosity-temperature relation of Arnaud & Evrard (1997). An AXAF A01 observation is scheduled for MS2053.7-0449. The SZ detection of this cluster is without sufficiently high signal-to-noise ratio to constrain its axis ratio well. Therefore, only the spherically fit gas fraction is included.

MS1137.5+6625 is one of the most x-ray luminous clusters known. It has recently been observed by the *ASCA* mission. Although there is not a published temperature for this cluster, we use an unpublished estimate (Donahue, private communication) of $5.7^{+2.1}_{-1.1}$ keV.

MS1054.4-0321 is one of the most distant clusters known, certainly the most distant cluster discovered by its x-ray emission. It exhibits a rather scrambled-egg appearance in the x-ray image, which may be due to poor signal-to-noise ratio, but its SZ data and image are regular and rounded.

Table 7.1.3: X-ray and Optical Properties of the Cluster Sample

Cluster	z	reference	T_e	reference	$L_x(10^{45} erg/s)$	band (keV)	reference
A2218	0.171	LB	$7.04^{+0.97}_{-0.97}$	MS	0.94	2-10	AE
A1914	0.1712	BA	$10.7^{+1.5}_{-1.5}$	EB	1.8	0.3-3.5	EB
A665	0.1818	SR	$8.26^{+0.9}_{-0.9}$	AE	1.50	2-10	AE
A1689	0.1832	SR	$9.02^{+0.40}_{-0.30}$	MS	3.22	2-10	AF
A2261	0.224	C95	$6.90^{+0.50}_{-0.50}$	HG	2.33	2-10	AF
A1835	0.2528	A92	$8.15^{+0.46}_{-0.45}$	MS	4.49	2-10	AF
A697	0.282	C95	$9.80^{+0.70}_{-0.70}$	HP	1.574	0.1-2.4	E98
A611	0.288	C95	$6.60^{+0.60}_{-0.60}$	HP	1.04	0.1-2.4	E98
A1995	0.318	HU	$10.70^{+2.50}_{-1.80}$	MS	0.87	0.3-3.5	MS
Z1953	0.32	BA	$13.2^{+2.0}_{-2.0}$	E98	2.86	0.3-3.5	E98
MS1358	0.328	GI	$7.48^{+0.50}_{-0.70}$	AF	1.05	0.3-3.5	AF
R1532	0.345	EB	$12.20^{+2.00}_{-2.00}$	E98	2.374	0.3-3.5	E98
A370	0.374	M88	$6.60^{+1.10}_{-0.90}$	OT	1.3	2-10	AE
CL0016	0.5479	GI	$8.00^{+1.00}_{-1.00}$	MS	1.46	0.3-3.5	GI
MS0451	0.55	GI	$10.17^{+1.55}_{-1.26}$	MS	0.7	0.3-3.5	GI
MS2054	0.583	GI	$6.60^{+2.00}_{-2.00}$	AEest	0.58	0.3-3.5	GI
MS1137	0.78	GI	$5.70^{+2.10}_{-1.10}$	D98b	1.9	0.3-3.5	GI
MS1054	0.826	LG	$12.30^{+3.10}_{-2.20}$	D97	9.3	0.3-3.5	LG

A92 Allen (1992); AF Allen & Fabian (1997)
AE Arnaud & Evrard (1998); AEest estimated from L_x-T relation of AE
BA Bade, N. *et al.* (1998); C95 Crawford *et al.* (1995)
D97 Donahue *et al.* (1996); D98 Donahue *et al.* (1998); D98b Donahue *et al.* (1998b)
EB Ebeling *et al.* (1996), E98 Ebeling (1998)
GI Gioia *et al.* (1990); HU Huchra *et al.* (1990)
HP Hughes *et al.* (1998); LB LeBorgne *et al.* (1992)
LG Luppino & Gioia (1995); M88 Mellier *et al.* (1988)
MS Mushotzky & Scharf (1997); N97 Nichol *et al.* (1997)
OT Ota *et al.* (1997); SR Struble & Rood (1991)

7.2 EMSS Subsample

A homogeneous sample of clusters has been identified from the *Einstein* Extended Medium Sensitivity Survey (EMSS) (Gioia *et al.* 1990). The EMSS consists of 835 serendipitous sources detected in a total area of 778 square degrees away from the Galactic plane. The limiting fluxes in the 0.3-3.5 keV energy band in the 1435 fields range from $\sim 5 \times 10^{-14}$ to $\sim 3 \times 10^{-12}$ ergs cm^{-2}s^{-1}. After optical followup on these sources, it was determined that $\sim$ 12% are clusters of galaxies (Stocke *et al.* 1991, Gioia & Luppino 1994). Nichol *et al.* (1997) reanalyzed the EMSS and refined this cluster sample.

The selection by x-ray luminosity is made after corrections for absorption by neutral hydrogen in the Milky Way, the difference in covered sky area at different flux limits, the correction for lost flux in the 2.4′ square detection cell, and the variation of these corrections with redshift. The restriction of the 2.4′ detection cell makes the EMSS in fact a surface-brightness limited survey, rather than a flux limited survey. This effect is less significant at the high redshifts of interest for the SZ work, and there are detailed prescriptions for correcting this effect (Gioia *et al.* 1990b, Henry *et al.* 1992).

Gioia & Luppino (1994) constructed a subsample of the EMSS which is suitable for a gravitational lens search. The criteria used selecting this sample make this sample suitable for SZ work. The Gioia and Luppino clusters are the most distant ($z > 0.15$), x-ray luminous ($L_x \geq 2 \times 10^4$4 erg/s) EMSS clusters observable from Hawaii ($\delta > 40°$). The 12 most luminous clusters in the Gioia & Luppino sample are presented in Table 7.2, along with their SZ observational status. SZ observations were made towards the most luminous of these clusters which are accessible from OVRO and BIMA. The additional requirements the SZ experiment imposes are that the clusters must be at a declination higher than about -10°, and must not have radio

bright point sources with flux > 5 mJy. The redshifts of two of the reported clusters were measured to greater precision after the publication of this sample; the updated redshifts and luminosities are used in this work.

Table 7.2: SZ-Observed X-ray Flux Limited Sample

Cluster	**a.k.a.**	**z**	L_x $\times 10^{44} h_{50}^{-2}$ erg/s	SZ status	SZ obs. $r.m.s.\mu$K
MS0451.6-0305[c]		0.550	20.0	detected	39.95
MS1137.5+6625[a,c]		0.782	19.0	detected	25.97
MS1455.0+2232		0.259	16.0	undetected	-
MS2137.3-2353		0.313	15.6	$\delta < -10$	-
MS0015.9+1609[c]	CL0016+16	0.546	14.6	detected	31.00
MS1358.4+6245[c]	Zw6429	0.327	10.6	detected	22.83
MS1054.4-0321[b,c]		0.826	9.3	detected	25.64
MS0451.5+0250	Abell 520	0.202	7.0	detected	28.19
MS2318.7-2328	Abell 2580	0.187	6.8	$\delta < -10$	-
MS0735.6+7421	Zw1370	0.216	6.1	undetected	172.99
MS0906.5+1110	Abell 750	0.180	5.8	undetected	47.31
MS2053.7-0449[c]		0.583	5.8	detected	19.19

[a]The redshift and L_x of this cluster are reported in Clowe et al. (1998).
[b]The redshift and L_x of this cluster are reported in Luppino & Gioia (1995).
[c]Included in the SZ EMSS sample

None of the clusters which are currently undetected have prohibitively bright radio point sources, although MS1455.0+2232 has four point sources at least, and proves a challenge. It is expected that these clusters will be detected in the future. In order to form a complete, homogeneous sample, the SZ EMSS sample is restricted to the

clusters in Table 7.2 which have $\delta > -10$ and $z > 0.26$. The clusters included in this sample are denoted with a superscript "c".

Chapter 8

SZ Gas Mass and Gas Mass Fraction Results

8.1 SZ Gas Fractions

Gas fractions are presented for all clusters in the sample. The fractions are calculated for three simple spheroidal geometries; spheres and oblate and prolate spheroidal clusters with the symmetry axes in the plane of the sky. The clusters A665, Zw1953, and MS2053.7-0449 are not included in the ellipsoidal fitting because axis ratio was not sufficiently constrained by the data.

The gas fractions calculated depend on the assumed cosmology through the angular diameter distance, D_A. We assume the values $\Omega_M = 0.3, \Lambda_0 = 0$, and $h = 1.0$ for the cosmological parameters. The gas fractions are calculated via the method described in Chapter 5, and within an angular radius of $65''$, the radius best constrained by the observing technique and model limitations. Measuring the gas fraction at a fixed angular radius necessitates that the measurements are made at different physical radii for clusters at different redshifts and temperatures. If clusters are self-similar, the more pertinent scale length is the radius at which the cluster has a particular overdensity, rather than its radius in length. At r_{500}, the mean mass density interior

to that radius, is 500 times the critical density parameter, $\rho_c = \frac{3H_0^2}{8\pi G}$. A cluster's virial radius is expected to be at $\sim r_{200}$.

Since the gas in clusters is found to be more extended than the dark matter, the cluster gas fraction will vary with radius, and approach the universal baryon fraction at the virial radius in massive clusters. In order to best estimate the true cluster gas fraction, we extrapolate the measured values, using relations derived from numerical simulations, to the value expected at r_{500}, based on the ratio expected between the value at r_X, the physical radius at which the measurement is made (the radius corresponding to 65″), and r_{500}. The physical radius at which the overdensity is 500 depends on the cluster temperature, an indicator of its mass, and also the redshift, since the critical density will change with redshift. The extrapolation is discussed and applied in Section 6.3, but we reproduce the relevant equations here. The radius r_{500} is calculated with the expression,

$$r_{500}(T_e, z) = (1.24 \pm 0.09) \left(\frac{T_e}{(1+z)^3\ 10\ \mathrm{keV}} \right)^{1/2} h^{-1}\mathrm{Mpc}.$$

And the correction to r_{500} is given here,

$$f_{gas}(r_{500}(T_e, z)) = f_{gas}(r_X) \left(\frac{r_{500}(T_e)}{r_X} \right)^{\eta},$$

where $\eta = 0.17$, $f_{gas}(r_{500}(T_e))$ is the gas fraction at r_{500}, and r_X is the radius at which the gas fraction is measured.

We tested our modeling and gas fraction analysis methods on a cluster taken from hydrodynamic simulations from Gus Evrard & Joe Mohr (private comm.). A simulated cluster was selected which has a gas temperature typical of the observed SZ clusters. An SZ decrement map was made, assuming the cluster is at z=0.3. The decrement map was "observed" by multiplying it by the primary beam of BIMA, sampling the Fourier transform of this with the u-v sampling of a typical observation, and adding noise also typical of an observation. The resulting dataset was fitted with a

circularly symmetric model and to an elliptical model and the spheroidal masses were calculated within an angular radius of 65″ using the same protocol as the actually observed clusters. The apparent axis ratio of the simulated cluster's projected SZ effect was 0.55. These gas fractions were scaled to r_{500} using the above relations, and compared to the simulated cluster's true gas fraction at r_{500}. The gas mass gas fractions were recovered accurately to within 3% when the cluster was assumed to be an oblate ellipsoid. The gas fraction was 50% too large when the cluster was modeled as a prolate ellipsoid, and was 8% too high when modeled as a sphere. Although this test is most useful when performed on a large set of simulations, we are encouraged by this test that the method is sound. We note that the ellipsoidal fitting takes advantage of the two-dimensional information available, but until more is known about the true distribution of cluster geometries, this extra information may not be especially useful. We calculate the gas fractions considering all three simple spheroidal geometries, but generally refer to the spherical model when estimating the gas fraction of a sample of clusters.

The gas fractions in the two ellipsoidal geometries, both within angular radius 65″ and r_{500}, are presented in Table 8.1. The gas fractions in spherical geometry, within angular radius 65″ and r_{500}, are presented in Table 8.2. Figures 8.1a. and b. show the ellipsoidal gas fractions as a function of redshift and x-ray temperature. Figures 8.2a. and b. show the spherical gas fractions as a function of redshift and x-ray temperature.

8.2 Comparison of SZ and X-ray Results

We calculate the weighted average gas fractions for the cluster sample; in the averaging, the measurements are weighted by their statistical uncertainties. The gas fractions are calculated within r_{500} for oblate, prolate and spherical cluster geometries

Table 8.1: SZ-derived Gas Fractions for Elliptical clusters

Cluster	z	a/b	T_e (keV)	$f_g h$ (65″) oblate	$f_g h$ (65″) prolate	r_{500} corr.	$f_g h$ (r_{500}) oblate	$f_g h$ (r_{500})) prolate
A2218	0.171	0.880	$7.04^{+0.97}_{-0.97}$	$11.33^{+4.80}_{-4.80}$	$13.39^{+5.57}_{-5.57}$	1.438	$16.30^{+6.91}_{-6.91}$	$19.26^{+8.01}_{-8.01}$
A1914	0.171	1.000	$10.70^{+1.50}_{-1.50}$	$3.61^{+1.86}_{-1.86}$	$3.61^{+1.86}_{-1.86}$	1.490	$5.37^{+2.76}_{-2.76}$	$5.37^{+2.76}_{-2.76}$
A1689	0.183	0.910	$9.02^{+0.40}_{-0.30}$	$5.16^{+1.61}_{-1.64}$	$6.19^{+1.63}_{-1.67}$	1.456	$7.52^{+2.34}_{-2.38}$	$9.02^{+2.38}_{-2.43}$
A2261	0.224	0.860	$6.90^{+0.50}_{-0.50}$	$7.80^{+13.05}_{-3.83}$	$9.88^{+15.15}_{-4.43}$	1.389	$10.83^{+18.12}_{-5.32}$	$13.72^{+21.04}_{-6.15}$
A1835	0.253	0.640	$8.15^{+0.46}_{-0.45}$	$8.88^{+1.90}_{-1.91}$	$13.58^{+2.66}_{-2.68}$	1.389	$12.33^{+2.64}_{-2.66}$	$18.87^{+3.70}_{-3.72}$
A697	0.282	0.820	$9.80^{+0.70}_{-0.70}$	$3.67^{+2.68}_{-2.17}$	$4.20^{+3.21}_{-2.19}$	1.394	$5.12^{+3.74}_{-3.03}$	$5.85^{+4.48}_{-3.06}$
A611	0.288	0.930	$6.60^{+0.60}_{-0.60}$	$5.25^{+10.56}_{-2.81}$	$5.78^{+10.57}_{-2.84}$	1.345	$7.07^{+14.20}_{-3.78}$	$7.77^{+14.21}_{-3.83}$
A1995	0.318	1.000	$10.70^{+2.50}_{-1.80}$	$4.75^{+2.66}_{-3.07}$	$4.75^{+2.66}_{-3.07}$	1.386	$6.59^{+3.69}_{-4.26}$	$6.59^{+3.69}_{-4.26}$
MS1358	0.328	0.990	$7.48^{+0.50}_{-0.70}$	$8.99^{+5.07}_{-4.93}$	$8.99^{+5.07}_{-4.93}$	1.340	$12.05^{+6.80}_{-6.61}$	$12.05^{+6.80}_{-6.61}$
R1532	0.345	1.000	$12.20^{+2.00}_{-2.00}$	$3.71^{+2.45}_{-2.01}$	$3.71^{+2.45}_{-2.01}$	1.390	$5.16^{+3.41}_{-2.80}$	$5.16^{+3.41}_{-2.80}$
A370	0.374	0.670	$6.60^{+1.10}_{-0.90}$	$6.40^{+2.39}_{-2.68}$	$10.66^{+4.36}_{-4.81}$	1.308	$8.37^{+3.12}_{-3.51}$	$13.95^{+5.70}_{-6.29}$
CL0016	0.548	0.764	$8.00^{+1.00}_{-1.00}$	$10.96^{+6.65}_{-3.55}$	$10.96^{+6.65}_{-3.55}$	1.281	$14.04^{+8.51}_{-4.55}$	$14.04^{+8.51}_{-4.55}$
MS0451	0.550	0.950	$10.17^{+1.55}_{-1.26}$	$14.26^{+4.22}_{-7.92}$	$14.26^{+4.22}_{-7.92}$	1.307	$18.63^{+5.51}_{-10.35}$	$18.63^{+5.51}_{-10.35}$
MS1054	0.826	1.000	$12.30^{+3.10}_{-2.20}$	$4.57^{+2.01}_{-2.58}$	$4.57^{+2.01}_{-2.58}$	1.270	$5.81^{+2.55}_{-3.28}$	$5.81^{+2.55}_{-3.28}$

for both the entire cluster sample and for the clusters with $z < 0.224$. The average gas fraction for the spherical geometry is also calculated for the homogeneous EMSS subsample. These gas fractions have been calculated assuming the cosmology (Ω_M= 0.3, Ω_Λ= 0). For the subset of clusters $z \leq 0.224$ (Abell 2218, Abell 1914, Abell 665, Abell 1689, Abell 2261), the measured gas fractions should be nearly independent of the assumed cosmology, as the angular diameter distance changes only a few percent for different assumed cosmologies.

It is instructive to compare the SZ-derived gas fractions from this experiment to other SZ- and x-ray-derived gas fractions. A recent gas fraction measurement was made using SZ observations (Myers *et al.* 1997). In this work, the integrated SZ effect in three clusters are measured using a single radio dish operating at centimeter wavelengths. Using shape parameters from published x-ray analyses, the central electron densities are calculated from the integrated SZ effect and the resulting gas masses are compared to the x-ray -derived binding masses. For three clusters, A2142, A2256 and the Coma cluster, they find a gas mass fraction of $0.061 \pm 0.011 h^{-1}$ at radii of 1-1.5 h^{-1} Mpc.

There have been several large x-ray cluster samples with which the gas fraction is measured, and we present these along with the SZ f_g measurements in Table 8.3. In Evrard (1997), the gas fractions reported in White & Fabian (1995) and David *et al.* (1995) for nearby clusters are examined and combined in a consistent way, and the gas fractions extrapolated to r_{500} in the same manner as described in Section 6.3. Also, gas fractions for a large, homogeneous, nearby sample are presented in Mohr *et al.* (1998). Included also are x-ray gas fractions derived for a number of individual, higher redshift clusters which are in the SZ sample. These are taken from the literature and converted to a fiducial cosmology of (Ω_M= 0.3, Ω_Λ= 0). This is certainly not an exhaustive examination of published x-ray gas fractions, but is illustrative of the range of values derived for cluster gas fractions. Since the analysis methods and outer radii varied widely for these measurements, it is difficult, and probably unwise, to compare the results quantitatively. The gas fractions have different cosmology dependences when derived with the SZ or x-ray techniques, and this should be noted when comparing the results. Qualitatively, though, the comparison does not suggest any large systematic offsets. This is a significant result, because a large clumping factor, $c = < n_e^2 >^{1/2} / < n_e >$, has been suggested as an explanation for the high gas fractions in clusters (White *et al.* 1993, Evrard 1997). A cluster with clumping factor

c would only require $1/c$ as much gas mass to produce the observed emission, and so the SZ and x-ray gas fraction measurements would differ by $\sim c$.

8.3 Cosmological Constraints

8.3.1 Comparison of Baryon Fraction with Ω_B

For the reasons discussed in Chapter 1, we make the assumption that clusters are fair samples of the universe, and that the relative mass of the baryonic component to the total mass component is representative of the composition of the universe as a whole. We consider our best estimate of the gas mass fraction to be a lower limit to the universal baryon fraction. It is certain that clusters contain baryons in luminous galaxies; generally the galaxy mass is an order of magnitude less than the gas mass (White *et al.* 1993; Forman & Jones 1982). It is also possible that some of the dark matter is also baryonic, though in total it should not exceed the the baryon mass fraction constrained by BBN, $\Omega_B h^2 < 0.015$ (Walker *et al.* 1991). We consider here that a cluster's gas mass is a good approximation to its total baryonic mass, which in turn is a good approximation to the universal baryon mass fraction.

Under this assumption, then, the relationship between the measured quantity of gas mass, f_g, and the cosmological parameters of interest is:

$$f_g \leq f_B = \frac{\Omega_B}{\Omega_M}, \tag{8.1}$$

where Ω_B is the ratio of baryon mass density in the universe to the critical mass density. The cluster gas fraction measurements can be used within the Big Bang Nucleosynthesis (BBN) paradigm to constrain Ω_M,

$$\Omega_M \leq \Omega_B / f_g. \tag{8.2}$$

The value of Ω_B is strongly constrained from BBN calculations and the measurements of the abundances of the light elements. The relative abundance of deuterium and hydrogen provide a particularly strong constraint on the baryonic matter density. A firm upper limit to Ω_B is set by the presence of deuterium in the local interstellar medium. This constrains the value of Ω_B to be less than $0.031h^{-2}$ (Linsky *et al.* 1995). Measurements of the D/H ratio in metal-poor Lyman-α absorption line systems in high-redshift quasars put an even more stringent constraint on the baryonic mass density. Figure 8.3.1 shows the light elemental abundances predicted from BBN models and current observational limits on ^{3}He, ^{4}He, ^{7}Li, and D/H. The shaded area contains the 95% confidence interval for the two D/H measurements of Burles & Tytler (1998) and Fan & Tytler (1994). For simplicity, we adopt the published value at 95% confidence from Burles & Tytler.

To infer an upper limit for Ω_M, the average gas fraction for the clusters with redshift < 0.25 is used (see Section 8.2). The cosmological parameter values used to calculate the angular diameter distance for this measurement are ($\Omega_M = 0.3$, $\Omega_\Lambda = 0$). In this redshift regime the effect of cosmological parameters on the gas fraction is only of order a few percent; assuming instead that ($\Omega_M = 1.0$, $\Omega_\Lambda = 0$) will lower the value by $\sim 4\%$.

The mean gas fraction for the spherical fit to the clusters is $(0.075^{+0.007}_{-0.011})h^{-1}$, 68% confidence. The implied upper limit of Ω_M is then:

$$\Omega_M \leq (0.019 \pm 0.002)h^{-2}/(0.075^{+0.007}_{-0.011})h^{-1}$$

$$\Omega_M h \leq 0.25^{+0.04}_{-0.03}, \text{at 68\% confidence.}$$

Using the more conservative value for Ω_B from Linsky *et al.* (1995), the constraint on Ω_M is relaxed,

$$\Omega_M \leq (0.031)h^{-2}/(0.075^{+0.007}_{-0.011})h^{-1}$$

$$\Omega_M h \leq 0.41^{+0.06}_{-0.04}, \text{at 68\% confidence.}$$

These values are conservative upper limits. For a more realistic estimate, we should include the baryon contribution from galaxies, and attempt to account for the overall dimunition of the baryon fraction in clusters with respect to the universal value, since some baryons are expected to not become bound to the cluster, *i.e.*, if preheating is important. Following White *et al.* (1993) we estimate the galaxy mass to be a fixed fraction of the cluster gas, $M_B = M_g(1 + 0.20h^{3/2})$. For a realistic equation of state, the gas in the cluster will be more extended than the dark matter; when this is assumed, the baryon fraction at r_{500} is an underestimate of the true baryon fraction (Evrard (1997)), $f_g(r_{500}) = 0.85 \times f_b(\text{universal})$. So we find the best limit on Ω_M is

$$\Omega_M = (0.019 \pm 0.002)h^{-2}/((0.075^{+0.007}_{-0.011})h^{-1}(1 + 0.2h^{3/2}))/0.85 \qquad (8.3)$$

$$\Omega_M = 0.29^{+0.05}_{-0.04}h^{-1}/(1 + 0.2h^{3/2}) = 0.37^{+0.07}_{-0.05} \text{ for } = 0.7.$$

Table 8.2: SZ-derived Gas Fractions for Spherical Clusters

Cluster	**z**	$\mathbf{T_e}$ (keV)	$\mathbf{f_g}h$ **(at 65″)**	$\mathbf{r_{500}}$ **corr.**	$\mathbf{f_g}h$ **(at** $\mathbf{r_{500}}$**)**
A2218	0.171	$7.04^{+0.97}_{-0.97}$	$11.33^{+5.20}_{-5.20}$	1.438	$16.30^{+7.48}_{-7.48}$
A1914	0.171	$10.70^{+1.50}_{-1.50}$	$3.61^{+1.86}_{-1.86}$	1.490	$5.37^{+2.76}_{-2.76}$
A665	0.182	$8.26^{+0.90}_{-0.90}$	$4.13^{+2.26}_{-2.26}$	1.447	$5.97^{+3.27}_{-3.27}$
A1689	0.183	$9.02^{+0.40}_{-0.30}$	$6.19^{+2.13}_{-2.16}$	1.456	$9.02^{+3.10}_{-3.14}$
A2261	0.224	$6.90^{+0.50}_{-0.50}$	$5.20^{+14.58}_{-3.22}$	1.389	$7.22^{+20.24}_{-4.47}$
A1835	0.253	$8.15^{+0.46}_{-0.45}$	$12.01^{+2.99}_{-3.00}$	1.389	$16.69^{+4.15}_{-4.17}$
A697	0.282	$9.80^{+0.70}_{-0.70}$	$2.10^{+4.21}_{-0.61}$	1.394	$2.93^{+5.87}_{-0.86}$
A611	0.288	$6.60^{+0.60}_{-0.60}$	$4.73^{+13.69}_{-3.28}$	1.345	$6.36^{+18.41}_{-4.41}$
A1995	0.318	$10.70^{+2.50}_{-1.80}$	$4.75^{+2.26}_{-2.74}$	1.386	$6.59^{+3.14}_{-3.80}$
Z1953	0.320	$13.20^{+2.00}_{-2.00}$	$5.28^{+10.69}_{-3.56}$	1.410	$7.45^{+15.08}_{-5.02}$
MS1358	0.328	$7.48^{+0.50}_{-0.70}$	$8.99^{+5.07}_{-4.93}$	1.340	$12.05^{+6.80}_{-6.61}$
R1532	0.345	$12.20^{+2.00}_{-2.00}$	$3.71^{+2.45}_{-2.01}$	1.390	$5.16^{+3.41}_{-2.80}$
A370	0.374	$6.60^{+1.10}_{-0.90}$	$9.06^{+4.50}_{-4.82}$	1.308	$11.86^{+5.89}_{-6.31}$
CL0016	0.548	$8.00^{+1.00}_{-1.00}$	$10.96^{+6.65}_{-3.55}$	1.281	$14.04^{+8.51}_{-4.55}$
MS0451	0.550	$10.17^{+1.55}_{-1.26}$	$12.06^{+5.34}_{-5.76}$	1.307	$15.76^{+6.98}_{-7.52}$
MS2054	0.583	$6.60^{+2.00}_{-2.00}$	$4.41^{+10.28}_{-3.84}$	1.252	$5.52^{+12.87}_{-4.81}$
MS1137	0.780	$5.70^{+2.10}_{-1.10}$	$6.24^{+3.74}_{-5.14}$	1.198	$7.48^{+4.48}_{-6.16}$
MS1054	0.826	$12.30^{+3.10}_{-2.20}$	$4.57^{+2.01}_{-2.58}$	1.270	$5.81^{+2.55}_{-3.28}$

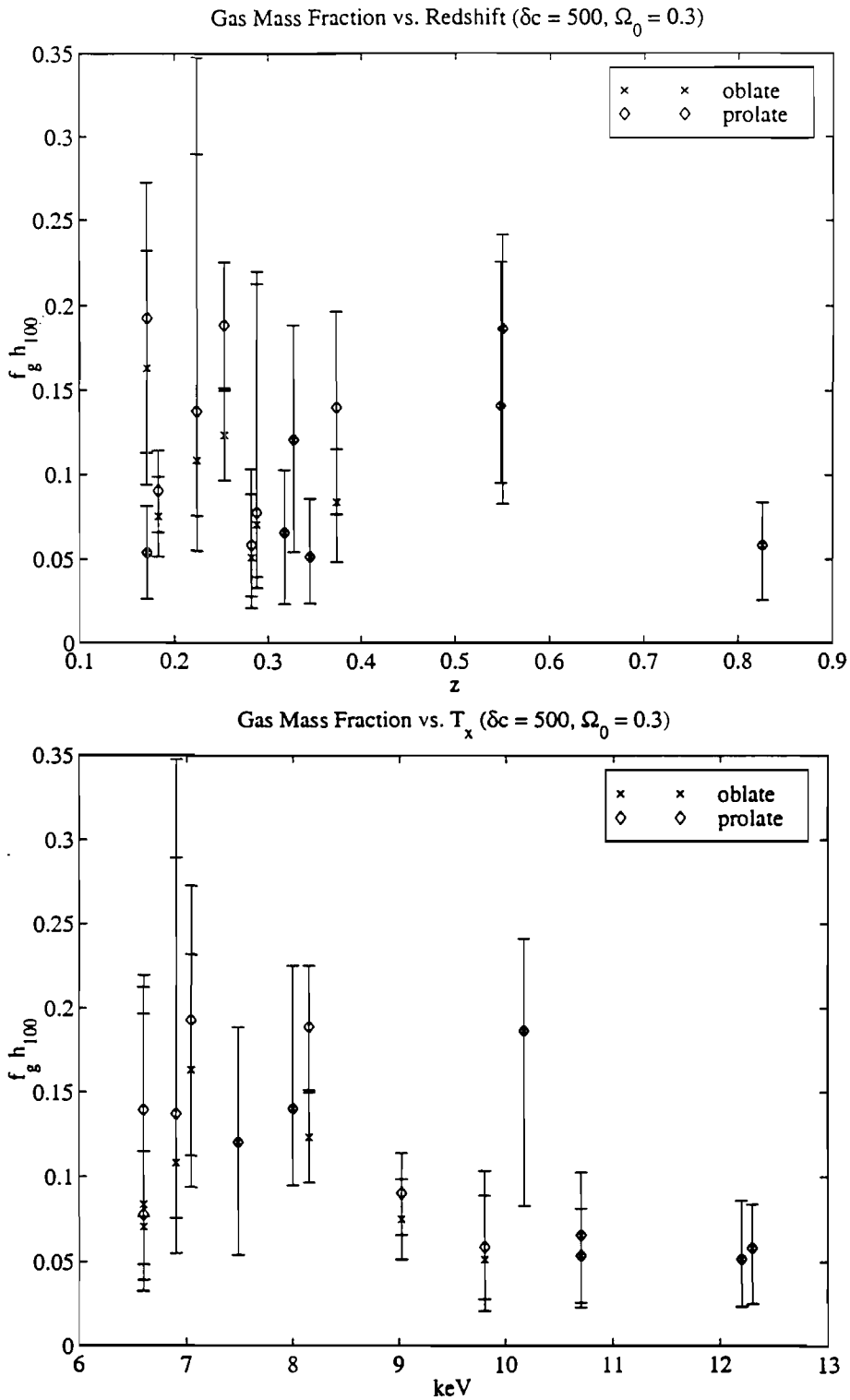

Figure 8.1 a. Gas fraction vs. z for oblate and prolate spheroidal clusters. b. Gas fraction vs. z for oblate and prolate spheroidal clusters.

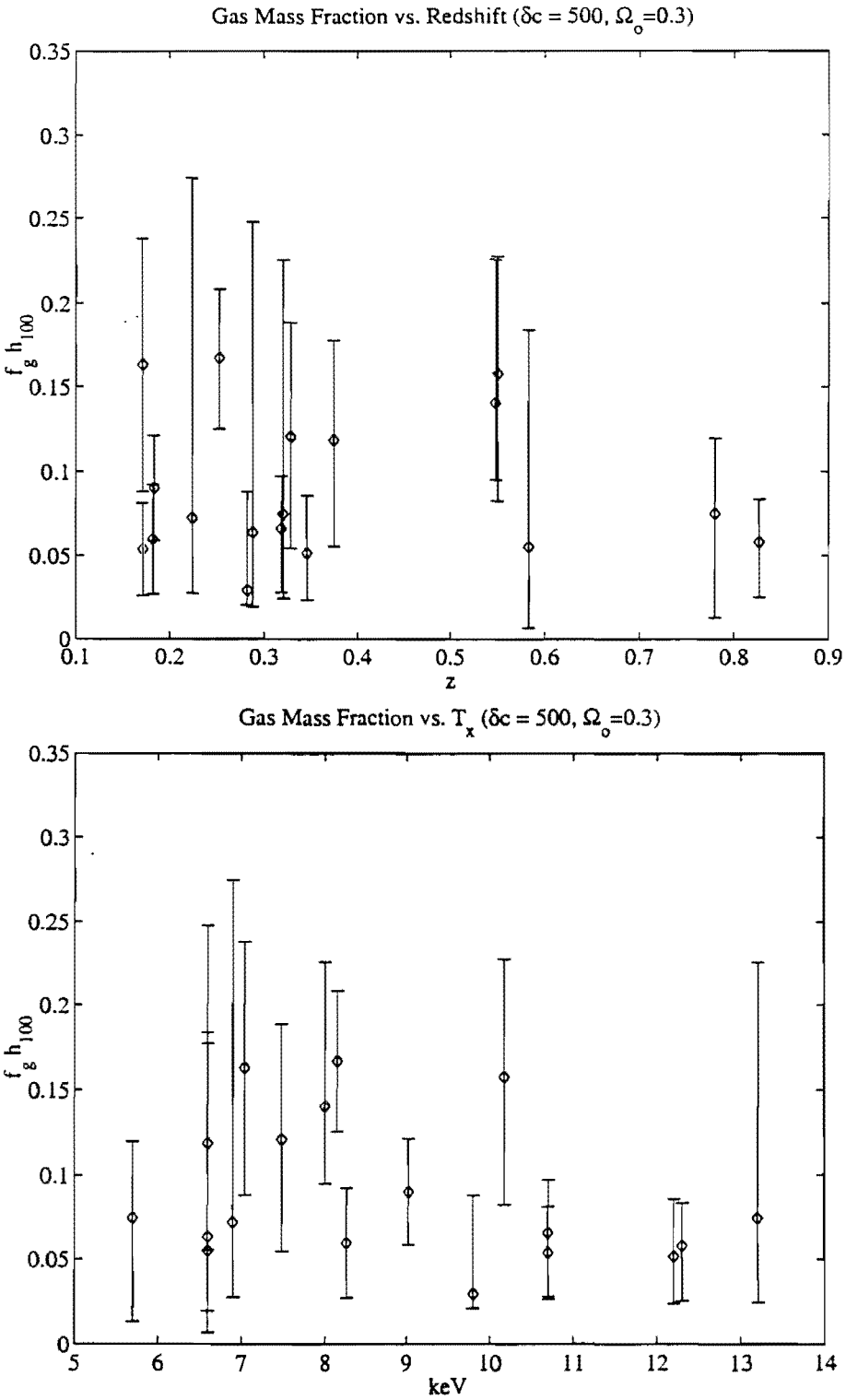

Figure 8.2 a. Gas fraction vs. z for spherical clusters. b. Gas fraction vs. z for spherical clusters.

Table 8.3: Mean Values of SZ and X-ray Derived Gas Fractions

Sample	Geom.	Radius	f_g	Notes
SZ full sample	spherical	r_{500}	$(7.49^{+0.65}_{-1.04})h^{-1}$	
SZ (z < 0.253)	spherical	r_{500}	$(8.53^{+1.49}_{-1.57})h^{-1}$	
SZ EMSS subsample	spherical	r_{500}	$(8.31^{+1.99}_{-1.94})h^{-1}$	(homogeneous)
SZ full sample	obl. ellip.	r_{500}	$(7.91^{+0.94}_{-0.98})h^{-1}$	
SZ full sample	pro. ellip.	r_{500}	$(8.70^{+1.01}_{-1.07})h^{-1}$	
SZ (z < 0.253)	obl. ellip.	r_{500}	$(8.79^{+1.41}_{-1.44})h^{-1}$	
SZ (z < 0.2534)	pro. ellip.	r_{500}	$(10.09^{+1.55}_{-1.58})h^{-1}$	
Myers sample[a]	spherical	1-1.5h^{-1} Mpc	$(6.1\pm1.1)h^{-1}$	SZ/x-ray obs.
Evrard sample[b]	spherical	r_{500}	$(6.0\pm0.3)h^{-3/2}$	
Mohr sample[c]	spherical	r_{500}	$(6.61\pm0.21)h^{-3/2}$	z<0.1, T_e>5keV
Buote & Canizares[d]	elliptical	$1.2h^{-1}$ Mpc	$(3\text{-}8)h^{-3/2}$	z < 0.1
CL0016+16[e]	spherical	$1.5h^{-1}$ Mpc r_{250}	$(5\text{-}11)h^{-3/2}$	
Abell 2163[f]	spherical	2 Mpc	$\sim 7h^{-3/2}$	

[a]Myers *et al.* (1997)
[b]Evrard (1997)
[c]Mohr *et al.* (1998)
[d]Buote & Canizares (1995)
[e]Neumann & Böhringer (1996)
[f]Squires *et al.* (1997)

Figure 8.3 Theoretical light element abundances versus $\Omega_B h^2$ in the BBN paradigm, with current observational constraints. The shaded area is the 95% confidence interval for the D/H abundance measurements of Burles *et al.* (1998) and Tytler, Fan, & Burles (1996), which are marked as boxes on the deuterium curve. These provide constraints on η, the baryon/photon ratio and hence on $\Omega_B h^2$.

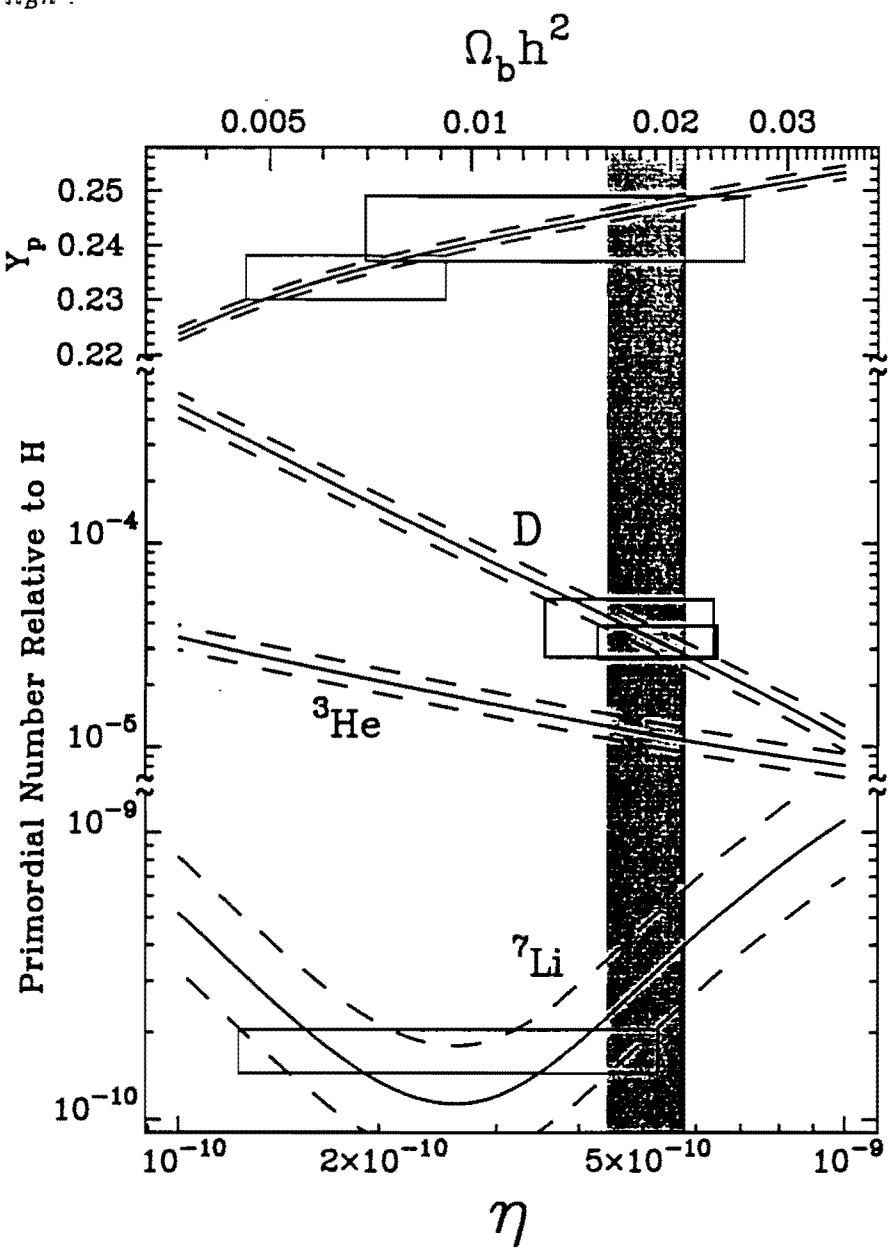

Chapter 9

Conclusions and Future Work

9.1 Constraints on Ω_M and Λ_o

Recently published work measuring the deceleration parameter of the universe, using Type Ia supernovae as standard candle distance indicators, has suggested evidence that the universe may be expanding at an accelerating rate (*c.f.*, Perlmutter *et al.* 1997; Schmidt *et al.* 1998). Riess *et al.* 1998 require a non-zero value of Ω_Λ at the 3-4 σ level to explain their observations, and are inconsistent with a matter-closed universe ($\Omega_M = 1$) at the 7-9 σ level. This work is relatively new, and the systematic effects are still being investigated. An independent test of such a provocative and interesting result is desirable.

As was noted in Sasaki (1996), and applied to x-ray observations of clusters in Pen (1996) and Cooray (1998), the gas fraction of clusters can be used as such an independent distance indicator if indeed the cluster gas fraction is a constant. To illustrate this, we return to the derivation of the gas fraction in Chapter 5.

The gas mass from the SZ effect is proportional to the angular diameter distance, D_A, whether the gas mass is measured in a cylindrical geometry or an elliptical geometry. The angular diameter distance relates the size, D, of an object and its apparent angular size, θ: $D_A = D/\theta$. In Section 5.1.1, the gas mass in a cylindrical

volume is calculated by integrating the SZ decrement model in a projected ellipse with angular radii (θ_{max}, $a/b \cdot \theta_{max}$). The SZ decrement is proportional to the electron density, n_e, integrated along the line of sight, $\Delta T \propto n_e m_p l$, *i.e.*, units of m/l^2. The integrated decrement is then proportional to m $\times$ (radians/l)^2. The conversion of integrated decrement to gas mass in the cylindrical volume requires the angular diameter distance, $\mathrm{M}_g(\mathrm{cyl.}) \propto {D_A}^2 \int\int \Delta T(\theta_r, \theta_z) d\theta_z d\theta_r$.

The ellipsoidal mass is also proportional to ${D_A}^2$. M_g(ellip.) is calculated by integrating the inferred gas density profile through the volume of the cluster. The shape of the density profile is taken from the fitted shape parameters, and the central density, n_{eo}, is inferred from Equation 4.7. The relationship between n_{eo} and D_A is more clearly seen when this relationship is expressed in the following way:

$$n_{eo} \propto \Delta T(0) \Big/ \left(T_e \int \left(1 + \left(\frac{\theta \cdot D_A}{\theta_c \cdot D_A} \right)^2 \right)^{-\frac{3}{2}\beta} d\theta \cdot D_A \right). \tag{9.1}$$

This density is integrated over an ellipsoidal volume with volume element $dV = {D_A}^3 \cdot \theta_r \delta\theta_r \delta\theta_z \delta\theta_\phi$. Therefore, M_g(ellip.) also depends on ${D_A}^2$.

The total mass of a cluster, calculated either by gravitational lensing measurements or by the virial relation, depends directly on D_A. The dark matter density is derived under the isothermal HSE assumption in Section 5.2.2. According to Equation 5.8,

$$\rho_{grav} = -\frac{kT_e}{4\pi G \mu m_p} \nabla^2 \ln \rho_{gas}. \tag{9.2}$$

In the cylindrical coordinates used for the analysis in this work,

$$\nabla^2 = \left(\frac{1}{\theta_r} \frac{\partial}{\partial \theta_r} \left(\theta_r \frac{\partial \Phi}{\partial \theta_r} \right) + \frac{1}{\theta_r^2} \frac{\partial^2 \Phi}{\partial \phi^2} + \frac{\partial^2 \Phi}{\partial \theta_z^2} \right) \frac{1}{{D_A}^2} \tag{9.3}$$

and again the volume element is $dV = {D_A}^3 \, \theta_r d\theta_r d\theta_z d\phi$. The total cluster mass from the HSE method is therefore proportional to D_A.

For a strongly lensed arc in a cluster, the critical mass density is (see, for example,

Narayan & Bartelmann 1997)

$$\Sigma_{cr} = 0.35 \text{ g cm}^{-3} \left(\frac{D}{\text{Gpc}}\right)^{-1}, \tag{9.4}$$

where

$$D = \frac{D_{ds}}{D_d D_s}, \tag{9.5}$$

and D_d, D_s, D_{ds} the angular diameter distances between the observer and lens, lens and source, and observer and source, respectively. To approximate the total mass within the Einstein radius, θ_{cr}, the critical mass density can be integrated within the area enclosed.

$$\text{M}_{total} = \int_0^{\theta_{cr}} \Sigma_{cr} D_{ds}^2 \cdot \theta d\theta \int_0^{2\pi} d\phi \tag{9.6}$$

And so the total mass measured by lensing is also proportional to the angular diameter distance to the cluster. Since the distance to the lensed source is also involved, the lensing mass is sensitive to cosmology in a more complicated way than is the virial mass.

The SZ-determined gas fraction then is proportional to ${D_A}^2/D_A = D_A$. Apparent evolution of the gas fraction with redshift can be used as a cosmological probe. Since the cluster gas fraction is expected to remain constant, a systematic change in gas fraction with redshift may be due to the dependence of $D_A$on q_o. In contrast, the x-ray-determined gas fractions will be proportional to ${D_A}^{3/2}$.

The angular diameter distance to an object depends on the geometry of the universe and its energy composition. We define $\Omega_{tot} \equiv \Omega_M + \Omega_\Lambda = 1 - \Omega_k$, where $\Omega_M = \frac{8\pi G}{3H_o^2}\rho_{M0}$ is the matter density in units of the critical density parameter, $\Omega_\Lambda \equiv \frac{\Lambda}{3H_o^2}$ is the cosmological constant term, and $\Omega_k \equiv -\frac{k}{R_o^2 H_o^2}$ is the curvature term, with k=−1, 0, 1 for an open, flat, and closed universe, respectively. The angular diameter distance is given in Caroll & Press (1992) as:

$$D_A = \frac{1}{H_o(1+z)} \frac{1}{|\Omega_k|^{1/2}} \text{sinn} \left[|\Omega_k|^{1/2} \int_0^{z_{source}} [(1+z)^2(1+\Omega_M z) - z(2+z)\Omega_\Lambda]^{-1/2} dz \right], \quad (9.7)$$

where sinn $\equiv$ sinh if $\Omega_k = 0$, and sinn $\equiv$ sin if $\Omega_k < 0$. In a flat ($\Omega_k = 0, \Omega_{tot} = 1$) Universe, the sinn and Ω_ks disappear from the expression. The angular diameter distance for a given source redshift, z_{source}, can be evaluated numerically without difficulty. There are analytic expressions for the flat universe case and for the case when $\Omega_\Lambda = 0$ (*e.g.*, Kolb & Turner 1990).

Figure 9.1 illustrates the expected change in behavior of D_A with redshift for a range of cosmologies. Figure 9.2 illustrates the expected change in apparent gas fraction with these cosmologies. The gas fractions plotted are calculated with an (Ω_M = 0.3, Ω_Λ = 0) cosmology. The lines plotted show the expected observed gas fraction value with respect to redshift if the true gas fraction is the same as that measured at z=0 by Mohr *et al.* (1998), and the true cosmology is different from this assumed cosmology. At our maximum observed redshift of 0.83, the gas fraction expected for a flat, (Ω_M =0.3, Ω_Λ =0.7) universe differs from that expected in a flat, (Ω_M =1.0, Ω_Λ =0) universe by 28%. From Figure 9.2, it appears that the statistical errors in the gas fraction measurements may still be prohibitively large to constrain cosmology in this way. However, we can also make a more quantitative assessment.

In order to evaluate whether the cosmology can be constrained by the SZ gas fractions, the gas fractions are fit to several different cosmological models, with Ω_M ranging from 0 to 1.0, and Ω_Λ ranging from −1 to 1. The gas fraction value is assumed to be constant for all clusters, but this value is allowed to take its best fit value for each (Ω_M, Ω_Λ) pair. Included with the SZ-derived gas fractions is the gas fraction derived for z << 0.1 in Mohr *et al.* (1998), in order to expand the redshift range. The test is repeated without including the Mohr *et al.* result and the results are significantly changed. In the former calculation, the SZ data are consistent with a

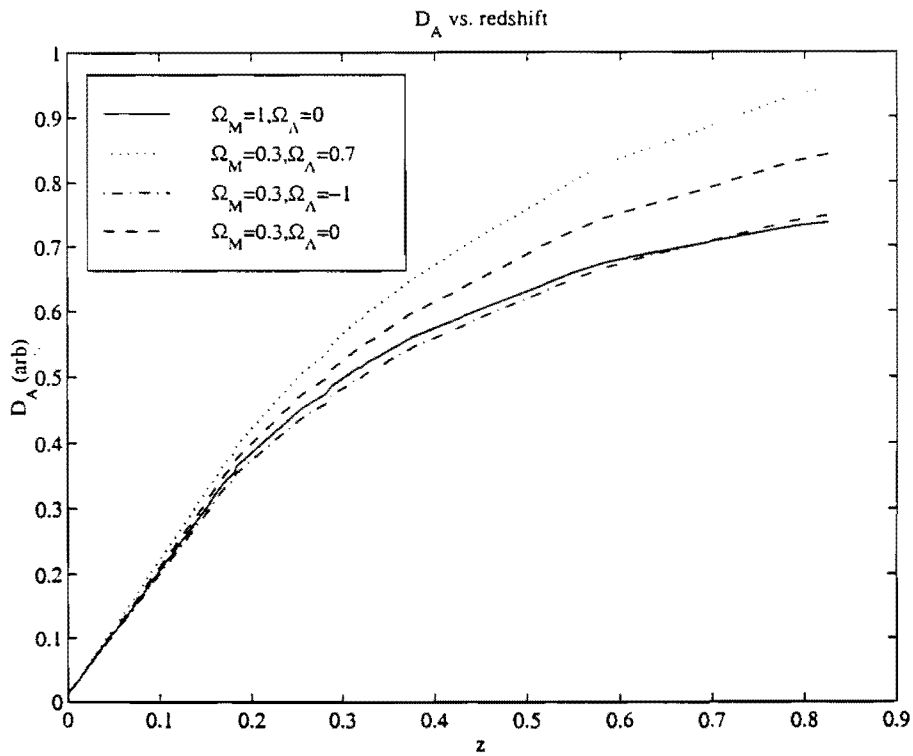

Figure 9.1 The expected change in behavior of D_A with z for different cosmologies, in arbitrary units.

universe closed by matter (Ω_M =1). For low values of Ω_M, no cosmological constant is necessary, but is not ruled out. For a value of Ω_M = 0.3, this fit requires that $-1.0 \leq \Omega_\Lambda \leq 0.6$. Without the "zero point," the data disfavor Ω_M =1, and require a cosmological constant. Accurate knowledge of this zero point is clearly critical. This test, however, cannot currently present strong cosmological constraints. The analysis of more SZ clusters should ameliorate the problem. Such a set of SZ-derived gas fractions constitute a uniformly analyzed sample of objects which span a large range of redshift, and are governed by well-understood physics. And it is unnecessary to appeal to BBN theory to constrain the curvature of the universe with this method. There are still means to significantly improve the statistical uncertainties in this method, so the constraints should improve significantly in the future.

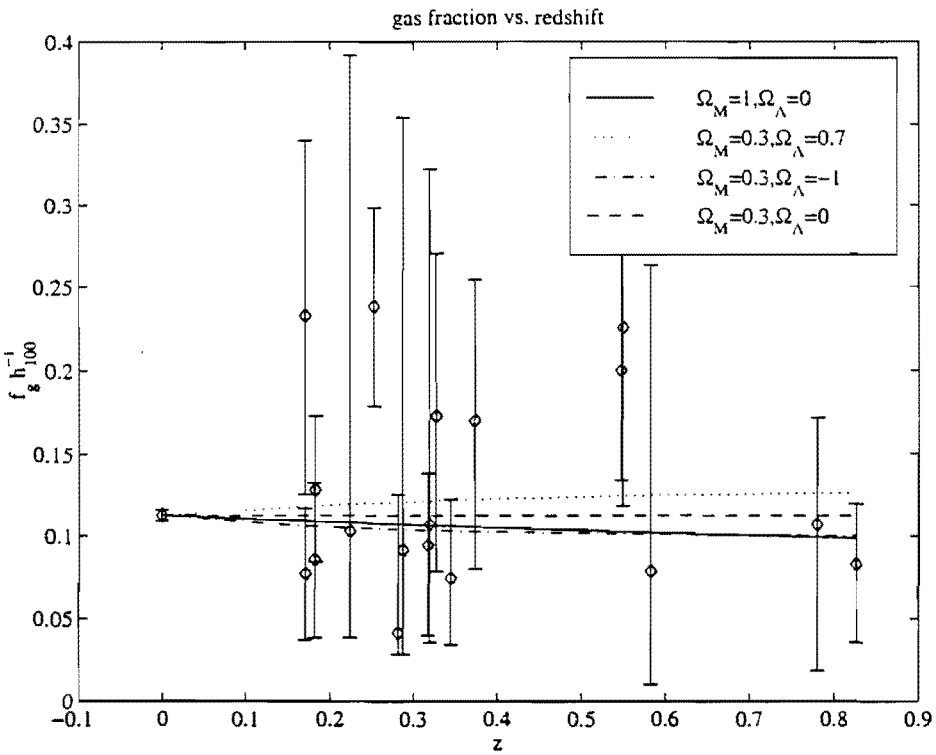

Figure 9.2 Presented are gas fractions measured assuming (Ω_M =0.3,Ω_Λ =0.0), and expected behavior of gas fraction if other sets of cosmological parameters are the true parameters.

To be noted is the fact that the SZ gas fraction values are all corrected to a fiducial radius of r_{500}, where the gas fraction should be the same for all clusters. These corrections are substantial, on the order of 20-30%, and the uncertainty in this correction may have a strong influence on these results, as the size of the correction is comparable to that of the expected signal. Examining further, possible systematic effects from the correction, the uncertainty in the power law exponent in the extrapolation relation Equation 6.1 is not large. The value $\eta = 0.17$ we use is derived from the numerical simulations of Evrard, Metzler & Navarro (1996). The values of η derived in Evrard (1997) for the White & Fabian (1995) sample have a mean η of 0.15, with a range of 0.05-0.28. The application of this relation does necessitate, though, that no significant evolution in the relationship of cluster gas to dark matter occurs between

z=0.8 and the current epoch.

Since the interferometry experiment measures the gas fraction at different overdensities for clusters at different redshifts and gas temperatures, the effectiveness of the use of the Evrard relation is likely to change with redshift. It is not necessary to make the measurements at r_{500} for this test; it is only necessary to measure at a radius at which the gas fraction is constant. The cluster sample has a factor of four range in redshift, and only a factor in two range in angular radius over which the gas fractions can be measured accurately. This possible systematic error can be improved by extrapolating to a fiducial radius which is closer to the scales at which the measurements are taken. Such an extrapolation relation could be derived from numerical simulations which currently exist.

9.2 Prospects for Improvement and Future Work

The centimeter-wave SZ interferometry experiment has matured in the last five years from an inspired idea to an instrument capable of detecting this elusive effect and is now engaged in a large survey of massive galaxy clusters. The cluster detections provide a tool with unique properties for studying the physics of clusters, a tool especially powerful when combined with observations at other wavelengths. The SZ cluster survey observations are suited for addressing cosmological questions because high redshift observations are not difficult and the physics governing the ICM is reasonably well-understood. The work presented here show these observations can provide an independent means to measure cosmological parameters. With a number of phenomena useful to investigation of the distant universe, *i.e.*, Type I supernovae, gravitational lensing, CMB and galaxy clusters, the systematic effects in cosmological measurements can begin to be understood.

The instrument and the analysis techniques are continually being improved. The

potential also exists for improving the centimeter-wave SZ interferometer dramatically by taking advantage of the 10 GHz output of the SZ receivers; currently a maximum of 2 GHz are correlated at OVRO and 0.8 GHz are correlated at BIMA.

The commission of the AXAF mission, with its unprecedented combination of sensitivity and angular and spectral resolution in the x-ray regime, should greatly improve our understanding of galaxy clusters and the intracluster medium. The uncertainty in the emission-weighted temperature is a dominant or significant contribution to the statistical uncertainties of the gas fraction measurements presented here and unresolved temperature structure may be a significant source of systematic uncertainty. Many of the clusters presented in this sample are scheduled to be observed in the first year of AXAF's mission, and the prospects for improving the gas fraction measurements through these AXAF measurements is promising.

Numerical simulations will also help identify other sources of systematic error, especially those incurred through the observational and analysis program. We plan to use hydrodynamic simulations of a sample of clusters to quantify any biases we may introduce to the gas fraction measurements with the interferometric method, through the simplified β-model fitting, and to determine the best geometric model (oblate ellipsoids, prolate ellipsoids, spheres) to assume for the gas mass and gas mass fraction measurements.

REFERENCES

AbdelSalam, H., Saha, P., & Williams, L. 1997, astro-ph 9707207

Alcock, C. *et al.* 1998. EROS and MACHO Combined Limits on Planetary-mass Dark Matter in the Galactic Halo. *Astrophys. J. Lett.* 499:L9–L12.

Allen, S. W. 1992, *M.N.R.A.S.*, 259, 67

Allen, S. W. 1998, *M.N.R.A.S.*, 296, 392

Allen, S. W., & Fabian, A. C. 1998, *M.N.R.A.S.*, 297, L63

Anders, E., & Grevesse, N. 1989, Geochimica et Cosmochimica Acta 53, 197

Arnaud, M., & Evrard, A. E. 1998, *M.N.R.A.S.* (submitted)

Astronomical Almanac 1994-1998

Bade, N. *et al.* 1998, *A. & A.*, 127, 145

Bahcall, N. A. 1975, *Ap. J.*, 198, 249

Bartelmann, M., & Steinmetz, M. 1996, *M.N.R.A.S.*, 283, 431

Bautz, M., Mushotzky, R., Fabian, A., Yamashita, K., Gendreau, K., Arnaud, K., Crew, G., & Tawara, Y. 1994, PASJ, 46, L131

Bezecourt, J., Kneib, J.-P., Soucail, G., & Ebbels, T., 1998, in preparation

Birkinshaw, M. 1998, Phys. Rep., in press

Birkinshaw, M., Hughes, J.P., & Arnaud, K.A. 1991, ApJ, 370, 466

Buote, D. A., & Canizares, C. R. 1996, *Ap. J.*, 457, 565

Burles, S., & Tytler, D. 1998, *Ap. J.*, 499, 699

Carlstrom, J.E., Joy, M.K., & Grego, L. 1996, ApJ, 456, L75

Carlstrom, J.E., Joy, M.K., Grego, L., & Holzapfel, W. 1997 Proceedings of the 21st Annual Texas Symposium on Relativistic Astrophysics, ed. Olinto, Frieman, Schramm

Carroll, S. M., & Press, W. H. 1992, *Ann. Rev. Astr. Ap.*, 30, 499

Cavaliere, A., & Fusco-Femiano, R. 1976, *A. & A.*, 49, 137

Cavaliere, A., & Fusco-Femiano, R. 1978, *A. & A.*, 70, 677

Challinor, A., & Lasenby, A. 1998, ApJ, 499, 1

Clowe, D., Luppino, G. A., Kaiser, N., Henry, J. P., & Gioia, I. M. 1998, *Ap. J. Letters*, 497, 61

Cooray, A. R. 1998, *A. & A.*, 333, 71

Cooray, A. R., Grego, L., Holzapfel, W. L., Joy, M., & Carlstrom, J. E. 1998, *A. J.*, 115, 1388

Copi, C. J., Schramm, D. N., & Turner, M. S. 1995, *Science*, 267, 192

Crawford, C. S., Edge, A. C., Fabian, A. C., Allen, S. W., Böhringer, H., Ebeling, H., McMahon, R. G., & Voges, W. 1995, *M.N.R.A.S.*, 274, 75

David, L. P., Harnden, F. R., Kearns, K. E., Zombeck, M. V., Harris, D. E., Prestwich, A., Primini, F. A., Silverman, J. D., & Snowden, S. L. 1997, The ROSAT High Resolution Imager (HRI) Calibration Report, U.S. ROSAT Science Data Center/SAO, 25

David, L. P., Jones, C., & Forman, W. 1995, ApJ, 445, 578

De Zeew, T. & Pfenniger, D. 1988, *M.N.R.A.S.*, 235, 949

Donahue, M., Voit, G. M., Gioia, I., Luppino, G., Hughes, J. P., & Stocke, J. T. 1998, *Ap. J.*, 502, 550

Donahue, M., Voit, M., Scharf, C. A., Mullis, Hughes, J. P., & Stocke, J. T. 1998 (in preparation)

Ebeling, H., Voges, W., Böhringer, H., Edge, A. C., Huchra, J. P., & Briel, U. G. 1996, *M.N.R.A.S.*, 281, 799

Ebeling, H., Voges, W., Böhringer, H., Edge, A. C., Huchra, J. P., & Briel, U. G. 1996, *M.N.R.A.S.*, 283, 1103

Ebeling, H., Voges, W., Böhringer, H., Edge, A. C., Huchra, J. P., & Briel, U. G. 1998, *M.N.R.A.S.*(submitted)

Evans, N. W. 1994, *M.N.R.A.S.*, 267, 333

Evrard, A.E. 1997, MNRAS, 292, 289

Evrard, A. E., Metzler, C. A., & Navarro, J. F. 1996, *Ap. J.*, 469, 494

Fabian, A. C. 1994, *Ann. Rev. Astr. Ap.*, 32, 277

Fabian, A. C., Crawford, C. S., Edge, A. C., & Mushotzky, R. F. 1994, *M.N.R.A.S.*, 267, 779

Fabricant, D., Rybicki, G., & Gorenstein, Pl 1984, ApJ, 286, 186

Fan, X., & Tytler, D. 1994, *Ap. J. Suppl.*, 94, 17

Forman, W., & Jones, C., 1982, ARA&A, 20, 547

Frenk, C., White, S., Efstathiou, G., & Davis, M. 1990, *Ap. J.*, 354, 10

Gioia, I. M., *et al.* 1990, *Ap. J.*, 72, 567

Gioia, I. M., Henry, J. P., Maccacaro, T., Morris, S. L., Stocke, J. T., & Wolter, A. 1990b, *Ap. J.*, 356, L35

Gioia, I. M., & Luppino, G. A. 1994, *Ap. J. Suppl.*, 94, 583

Grainge, K., Jones, M., Pooley, G., Saunders, R., & Edge, A. 1993, MNRAS, 265, L57

Henry, J. P., Gioia, I. M., Maccacaro, T., Morris, S. L., Stocke, J. T., & Wolter, A. 1992, *Ap. J.*, 386, 408

Holzapfel, W.L., Ade, P. A. R., Church, S. E., Mauskopf, P. D., Rephaeli, Y., Wilbanks, T. M., & Lange, A. E. 1996, *Ap. J.*, 481, 35

Holzapfel, W.L., Ade, P.A.R., Church, S.E., Mauskopf, P.D., Rephaeli, Y., Wilbanks, T.M., & Lange, A.E. 1997, ApJ, 481, 35

Huchra, J. P., Geller, M. J., Henry, J. P., & Postman, M. 1990, *Ap. J.*, 365, 66

Hughes, J. P. & Birkinshaw, M. 1998, *Ap. J.*, 501, 1

Hughes, J. P., Gomez, P., Joy, M. K., Carlstrom, J. E., Grego, L., Reese, E., *Ap. J.*, (in preparation)

Jones, C. & Forman, W. 1984, *Ap. J.*, 276, 38

Jones, M. E. 1990, in ASP Conf. Proc. 19, Radio Interferometry; Theory, Techniques and Applications, ed., T. J. Cornwell & R. A. Perley (San Francisco: ASP, 395)

Jones, M., *et al.* 1993, Nature, 365, 320

Kim, K. T., Kronberg, P. P., Dewdney, P. E., & Landecker, T. L. 1990, *Ap. J.*, 355, 29

Kneib, J., Mellier, Y., Fort, B., & Mathez, G. 1993, A & A, 273, 370

Kolb, E. W., & Turner, M. S. 1990, *The Early Universe*. Redwood City, CA: Addison-Wesley

LeBorgne *et al.* 1992, *A. & A.*, 95, 87

[Le Fevre, O., Hammer, F., Angonin, M. C., Gioia, I. M., & Luppino, G. A. 1994, *Ap. J. Letters*, 422, L5

Linsky, J. L., Diplas, A., Wood, B. E., Brown, A., Ayres, T. R., & Savage, B. D. 1995, *Ap. J.*, 451, 335

Loeb, A., & Mao, S. 1994, ApJ, 435, L109

Loeb, A., & Refregier, A. 1997, *Ap. J.*, 476, L59

Luppino, G. A., & Gioia, I. M. 1995, *Ap. J. Letters*, 445, 77

Markevitch, M., 1996, ApJ, 465, L1

Mather, J. C. *et al.* 1994, *Ap. J.*, 420, 439

McMillan, S., Kowalski, M., & Ulmer, M., 1989 ApJS, 70, 723

Mellier, Y. 1987, High Redshift and primeval Galaxies: Proc. of the Third IAP Workshop, 207

Mellier, Y., Soucail, G., Fort, B., & Mathez, G., 1988, A & A, 199, 13

Metzler, C.A., & Evrard, A.E. (submitted) ApJ, astro-ph/9710324

Miralda-Escudé, J., & Babul, A. 1995, ApJ, 449, 18

Mohr, J. J., Evrard, A. E., Fabricant, D. G., & Geller, M. J. 1995, ApJ, 447, 8

Mohr, J. J., Mathiesen, B., & Evrard, A. E. 1998, *Ap. J.*(submitted)

Mushotzky, R. F., & Scharf, C. A. 1997, ApJ, 482, L13

Myers, S. T., Baker, J.E., Readhead, A.C.S., & Leitch, E.M. 1997, ApJ, 485, 1

Narayan, R., & Bartelmann, M. 1997, *Formation of Structure in the Universe*, Dekel, A. & Ostriker, J.P., ed. Cambridge University Press

Navarro, J. F., Frenk, C. S., & White, S. D. M., 1997, *Ap. J.*, 490, 493

Neumann, D. M., & Böhringer, H. 1997, *M.N.R.A.S.*, 289, 123

Nichol, R. C., Holden, B. P., Romer, A. K., Ulmer, M. P., Burke, D. J., & Collins, C. A. 1997, *Ap. J.*, 481, 644

Ohashi, T. *et al.* 1996, *PASJ*, 48, 157

Ota, N., Mitsuda, K., & Fukazawa, Y. 1997, Proceedings of the ASCA/ROSAT Workshop on Clusters of Galaxies, Japan Society for the Promotion of Science

Padin, S. 1994, *IEEE Transactions on Instrumentation and Measurement*, 43, 782

Pen, U. 1997, NEWA, 2, 309

Peres, C. B., Fabian, A. C., Edge, A. C., Allen, S. W., Johnstone, R. M, & White, D. A. 1998, *M.N.R.A.S.*, 298, 416

Perley, R. A., Schwab, F. R., & Bridle, A. H. 1994, in *Synthesis Imaging in Radio Astronomy*, ASP Conference Series

Perlmutter, S., *et al.* 1997, *Ap. J.*, 483, 565

Pospieszalski, M. W., Lakatosh, W. J., Nguyen, L. D., Lui, M., Liu, T., Le, M., Thompson, M. A., Delaney, M. J. 1995, Microwave Symposium Digest, IEEE MTT-S International, 3, 1121

Rephaeli, Y. 1995, Annual Reviews A & A, 33, 541

Riess, A. G., *et al.* 1998, *Ap. J.*, 116, 1009

Roettiger, K., Loken, C., & Burns, J. O. 1997, *Ap. J. Suppl.*, 109, 307

Rudy, D. J., 1987, Ph.D. Thesis, California Institute of Technology

Sarazin, C. 1988, in *X-ray Emissions from Clusters of Galaxies*, Cambridge Astrophysics Series

Sasaki, S. 1996, PASJ, 48, L119

Sault, R. J., Teuben, P. J., & Wright, M. C. H. 1995, ADASS 4, 77, 433

Schmidt, B. P., *et al.* 1998, *Ap. J.*, 507, 46

Scoville, N. Z., *et al.* 1993, PASP, 105, 1482

Shepherd, M. C., Pearson, T. J., & Taylor, G. B. 1994, *Bull. Amer. Astron. Soc.*, 26, 987

Smail, I., Dressler, A., Kneib, J.-P., Ellis, R.S., Couch, W.J., Sharples, R.M., & Oemler, A., Jr. 1996, ApJ, 469, 508

Soucail, G., Mellier, Y., Fort, B., Mathez, G., & Cailloux, M. 1988, A & A, 191 no. 2, L19

Squires, G., Kaiser, N., Babul, A., Fahlman, G., Woods, D., Neumann, D. M., & Böhringer, H. 1996, *Ap. J.*, 461, 572

Squires, G., *et al.* 1997, *Ap. J.*, 482, 648

Stark, A. A. 1977, ApJ, 213, 368

Stocke, J. T., *et al.* 1991, *Ap. J. Suppl.*, 76, 813

Struble & Rood 1991, *Ap. J. Suppl.*, 77, 363

Sunyaev, R. A., & Zel'dovich, Y. B. 1970, *Comm. Astrophys. Space Phys. 2, 173*

Sunyaev, R. A., & Zel'dovich, Y. B. 1972, *Comm. Astrophys. Space Phys. 4, 173*

Suto, S., Sasaki, S., & Makino, N. 1998, *Ap. J.*(accepted), astro-ph/9807112

Taylor, G. B., & Perley, R. A. 1993, *Ap. J.*, 416, 554

Tyson, A. J., & Fischer, P. 1995, *Ap. J. Letters*, 446, L55

Tyson, A. J., Kochanski, G. P., & Dell'Antonio, I. P. 1998, *Ap. J.*, 498, L107

Tytler, D., Fan, X.-M., & Burles, S. 1996, Nature, 381, 207

Walker, T. P., *et al.* 1991, *Ap. J.*, 376, 51

Walsh, D., Carswell, R. F., Weymann, R. J. 1979, *Nature*, 279, 381

Wagoner, R. V., Fowler, W. A., & Hoyle, F. 1967, *Ap. J.*, 148, 3

Webb, J.K., Carswell, R.F., Lanzetta, K.M., Ferlet, R., Lemoine, M., Vidal-Madjar, A., Bowen, D.V. 1997, Nature, 388, 250

White, D. A., & Fabian, A. C. 1995, *M.N.R.A.S.*, 273, 72

White, D. A., Jones, C., & Forman, W. 1997, *M.N.R.A.S.*, 292